

Suvi Huhtanen

3D BIOPRINTING OF HUMAN CORNEA MIMICKING STRUCTURES WITH STROMA AND EPITHELIUM

Master's Thesis
Faculty of Medicine and Health
Technology
Professor Minna Kellomäki
PhD Anni Mörö
December 2023

ABSTRACT

Suvi Huhtanen: 3D Bioprinting of Human Cornea Mimicking Structures with Stroma and Epithelium

Master's Thesis

Tampere University

Master's Programme in Biotechnology and Biomedical Engineering

December 2023

There is an immense need for corneal transplants to restore vision after injury or disease. Due to the shortage of donor corneas, three dimensional (3D) bioprinting has emerged as a possible solution to create cornea mimicking structures. The cornea consists of five layers, with the stroma and epithelium forming the two outermost cellular layers. To be able to 3D bioprint these layers, bioinks, and appropriate cell types are needed. For the epithelial layer, human pluripotent stem cell -derived corneal limbal epithelial stem cells (hPSC-LSCs) have great potential. For the stromal layer, human adipose stem cells -derived corneal stromal keratocytes (hASC-CSKs) have been explored together with a hyaluronic acid -based dopamine-containing (HA-DA) stromal bioink. To be able to create cornea mimicking structures with stroma and epithelium, the structures must be co-cultured after 3D bioprinting. However, the HA-DA stromal bioink is not stable in limbal epithelial stem cell (LSC) medium required by the hPSC-LSCs. To address this issue, this thesis aimed to enhance the stiffness and stability of the HA-DA stromal bioink in the LSC medium co-culture condition to enable the co-culture of 3D bioprinted cornea mimicking structures with stroma and epithelium.

To enhance the stiffness and stability of the HA-DA stromal bioink, the bioink composition was modified by incorporating a methacrylated hyaluronic acid (HAMA) component into the bioink to create a photocrosslinkable HA-DA HAMA stromal bioink. First, the composition of this HA-DA HAMA stromal bioink was optimized by evaluating the printability and shape fidelity of the bioink as well as handling of bioprinted structures after incubation in LSC medium. Then, the optimized HA-DA HAMA stromal bioink was compared to the original HA-DA stromal bioink by analyzing printability, shape fidelity, viscosity, swelling behavior, handling, mechanical properties, and transparency of the bioinks. After this, the cytocompatibility of the bioinks with hASC-CSKs was assessed. In the final part of this thesis, human cornea mimicking structures with stroma and epithelium were bioprinted, and two different co-culture conditions were tested.

HA-DA HAMA stromal bioink with good printability and shape fidelity was developed, and bioprinted stromal structures demonstrated good stability after incubation in LSC medium. Based on the comparison of the HA-DA and HA-DA HAMA stromal bioinks, the bioinks had similar printability, shear-thinning behavior, and transparency. Moreover, after incubation in LSC medium, the HA-DA HAMA stromal bioink had improved characteristics regarding handling, swelling, and shape fidelity. However, the HA-DA HAMA stromal bioink lacked the necessary cytocompatibility required for bioinks and demonstrated inferior cytocompatibility compared to the HA-DA stromal bioink. This underlined the importance of conducting cytocompatibility tests as part of bioink characterization. Furthermore, it was confirmed that the LSC medium co-culture condition significantly influenced the properties of the HA-DA stromal bioink. Therefore, bioink characterization should always consider the final application of the 3D bioprinted construct. Finally, cornea mimicking structures with stroma and epithelium were successfully bioprinted for the first time using extrusion-based bioprinting. A suitable co-culture condition was also found which combined the cell culture medium of both cell types used in the structure. This fulfilled better the needs of both cell types and prolonged the stability of the HA-DA stromal bioink during cell culture. In the future, further research is required to optimize cell density in the epithelial layer and analyze the effect of the co-culture medium on both cell types. Based on these findings, cornea mimicking structures with improved stability and cellular functionality can be 3D bioprinted in the future.

Keywords: 3D bioprinting, cornea, stroma, epithelium, HAMA

The originality of this thesis has been checked using the Turnitin OriginalityCheck service.

TIIVISTELMÄ

Suvi Huhtanen: Strooma- ja epiteelikerroksen sisältävien ihmisen sarveiskalvorakenteiden 3D-biotulostus
Diplomityö
Tampereen yliopisto
Bioteknologian ja biolääketieteen tekniikan maisteriohjelma
Joulukuu 2023

Tarve sarveiskalvosiirteille näön palauttamiseksi vamman tai sairauden jälkeen on valtava. Luovutettujen sarveiskalvosiirteiden pulan vuoksi kolmiulotteinen (3D) -biotulostus on noussut esiin lupaavana ratkaisuna keinotekoisien sarveiskalvorakenteiden luomiseen. Sarveiskalvossa on viisi kerrosta, joista strooma ja epiteeli muodostavat kaksi ulointa solukerrosta. Näiden kerrosten 3D-biotulostaminen edellyttää sopivia biomusteita ja solutyyppejä. Epiteelikerrosta varten ihmisen pluripotenteista kantasoluista erilaistettujen limbaaliset kantasolut ovat lupaava vaihtoehto. Puolestaan stroomakerroksen osalta lupaavia ovat ihmisen rasvakudoksen kantasoluista erilaistettujen sarveiskalvon strooman keratotsyytit yhdessä hyaluronihappopohjaisen dopamiinia sisältävän (HA-DA) biomusteen kanssa. Strooma- ja epiteelikerroksen sisältävän sarveiskalvorakenteen valmistamiseksi 3D-biotulostettua rakennetta täytyy voida viljellä biotulostuksen jälkeen. HA-DA -biomuste ei kuitenkaan ole stabiili limbaalisten kantasolujen vaatimassa limbaalisten kantasolujen (eng. limbal epithelial stem cell, LSC) -mediumissa. Ongelman ratkaisemiseksi tämän opinnäytetyön tavoitteena oli parantaa HA-DA biomusteen jäykkyyttä ja stabiilisuutta LSC-mediumissa, jotta 3D-biotulostettujen sarveiskalvorakenteiden viljely olisi mahdollista.

HA-DA -biomusteen jäykkyyden ja stabiilisuuden parantamiseksi biomusteen koostumusta muokattiin sisällyttämällä biomusteeseen metakryloitua hyaluronihappoa (HAMA) valoristisilloitettavan HA-DA HAMA -biomusteen kehittämiseksi. Ensimmäiseksi tämän HA-DA HAMA -biomusteen koostumus optimoitiin arvioimalla biomusteen tulostettavuutta ja filamenttien muodon pysyvyyttä sekä 3D-biotulostettujen rakenteiden käsiteltävyyttä LSC-mediumissa inkuboinnin jälkeen. Tämän jälkeen HA-DA HAMA -biomustetta verrattiin alkuperäiseen HA-DA -biomusteeseen analysoimalla biomusteiden tulostettavuutta, filamenttien muodon pysyvyyttä, viskositeettia, turpoamista, käsiteltävyyttä, mekaanisia ominaisuuksia sekä läpinäkyvyyttä. Seuraavaksi biomusteiden soluyhteensopivuutta arvioitiin ihmisen rasvakudoksen kantasoluista erilaistettujen sarveiskalvon strooman keratotsyyttien kanssa. Lopuksi 3D-biotulostettiin sarveiskalvorakenteita, jotka sisälsivät strooma- ja epiteelikerroksen, sekä tutkittiin kahta erilaista viljelyolosuhdetta.

Kehitetyillä HA-DA HAMA -biomusteella oli hyvä tulostettavuus sekä filamenttien muodon pysyvyys tulostamisen jälkeen, ja 3D-biotulostetuilla rakenteilla oli hyvä stabiilisuus LSC-mediumissa inkuboinnin jälkeen. HA-DA ja HA-DA HAMA -biomusteen vertailun perusteella biomusteilla oli samanlainen tulostettavuus, leikkausohenevyys sekä läpinäkyvyys. Lisäksi LSC-mediumissa inkuboinnin jälkeen HA-DA HAMA -biomusteella oli hieman parantuneet ominaisuudet käsiteltävyyden, turpoamisen ja filamenttien muodon pysyvyyden suhteen. Kuitenkin HA-DA HAMA -biomusteelta puuttui biomusteilta vaadittava soluyhteensopivuus, ja sen soluyhteensopivuus oli huomattavasti heikompi kuin HA-DA -biomusteen soluyhteensopivuus. Tämä korosti soluyhteensopivuustestien tärkeyttä osana biomusteen karakterisointia. Lisäksi vahvistettiin, että LSC-medium vaikuttaa merkittävästi HA-DA -biomusteen ominaisuuksiin. Tämän takia biomusteen karakterisoinnissa tulisi aina ottaa huomioon 3D-biotulostetun rakenteen lopullinen käyttöolosuhde. Lopuksi sarveiskalvorakenteita, jotka sisälsivät strooma- ja epiteelikerroksen, 3D-biotulostettiin onnistuneesti ensimmäistä kertaa käyttäen ekstruusiopohjaista biotulostusta. Rakenteita varten löydettiin sopiva viljelyolosuhde, joka yhdisti molempien käytettyjen solutyypin viljelymediumit täyttämällä paremmin molempien solutyypin tarpeet ja pidentämällä HA-DA biomusteen stabiilisuutta viljelyn aikana. Tulevaisuudessa epiteelikerroksen solutiheys tulisi optimoida ja viljelyolosuhteen vaikutusta molempiin solutyyppeihin tulisi analysoida. Näiden löydösten perusteella tulevaisuudessa voidaan 3D-biotulostaa sarveiskalvorakenteita, joilla on parempi stabiilisuus sekä solutoiminnallisuus.

Avainsanat: 3D-biotulostus, sarveiskalvo, strooma, epiteeli, HAMA

Tämän julkaisun alkuperäisyys on tarkastettu Turnitin OriginalityCheck –ohjelmalla.

PREFACE

This Master's thesis was done in the Eye group at the Faculty of Medicine and Health Technology at Tampere University. First, I want to thank my supervisors PhD Anni Mörö and MSc Paula Puistola for their dedication, support, and advice they gave me during the thesis process. In addition, I want to thank MSc Maija Kauppila for helping me with the experimental part of this thesis, and the leader of the Eye Group Professor Heli Skottman for giving me the opportunity to do my thesis in her research group. Lastly, I want to thank my family and friends who have supported me during this thesis process and throughout my studies.

Tampere, 13 December 2023

Suvi Huhtanen

CONTENTS

1.INTRODUCTION.....	1
2.HUMAN CORNEA.....	3
2.1 Structure of the cornea.....	3
2.2 Corneal cell types.....	6
2.2.1 Human corneal stromal keratocytes.....	6
2.2.2 Limbal epithelial stem cells.....	7
3.CORNEAL BLINDNESS.....	9
3.1 Corneal diseases and injury.....	9
3.2 Current Treatments.....	10
4.CORNEAL TISSUE ENGINEERING.....	13
4.1 Scaffold-free approaches.....	14
4.2 Scaffold-based approaches.....	15
4.3 Stem cells as cell source for corneal tissue engineering.....	17
5.3D BIOPRINTING.....	19
5.1 Extrusion-based bioprinting.....	19
5.2 Other 3D bioprinting approaches.....	22
6.BIOINKS.....	25
6.1 Hydrogels.....	26
6.2 Crosslinking.....	28
6.2.1 Photocrosslinking.....	29
6.2.2 Click chemistry.....	32
6.3 Characterization of Bioinks.....	33
7.3D BIOPRINTING OF CORNEA.....	38
8.AIM OF THE THESIS.....	43
9.MATERIALS AND METHODS.....	44
9.1 Crosslinking components for bioinks.....	45
9.2 Preparation of bioinks.....	45
9.3 3D bioprinting setup and printing procedure.....	46
9.4 Optimization of HA-DA HAMA stromal bioink.....	47
9.5 Characterization of stromal bioinks.....	49
9.5.1 Printability and shape fidelity.....	49
9.5.2 Viscosity of bioinks.....	50
9.5.3 Swelling behavior of bioprinted structures.....	50
9.5.4 Handling of bioprinted structures.....	50
9.5.5 Rheology of bioprinted structures.....	51
9.5.6 Transparency.....	51

9.6	Cells.....	52
	9.6.1 hASC ethical statement.....	52
	9.6.2 hASC-CSKs.....	52
	9.6.3 hPSC-LSCs	53
9.7	Cytocompatibility of stromal bioinks	54
	9.7.1 Cell culture of 3D bioprinted stromal structures.....	54
	9.7.2 Live/Dead.....	55
	9.7.3 Immunofluorescence staining.....	56
9.8	Human cornea mimicking structures with stroma and epithelium	57
	9.8.1 3D bioprinting procedure.....	57
	9.8.2 Co-culture of cornea mimicking structures	58
	9.8.3 Analysis of cornea mimicking structures	58
9.9	Statistical Analysis	58
10.	RESULTS.....	59
	10.1 Optimization of HA-DA HAMA stromal bioink	59
	10.2 Characterization of stromal bioinks	61
	10.2.1 Printability.....	62
	10.2.2 Shape fidelity during incubation	64
	10.2.3 Swelling behavior of bioprinted structures.....	66
	10.2.4 Handling of bioprinted structures	67
	10.2.5 Rheology of bioprinted structures	68
	10.2.6 Transparency.....	70
	10.3 Cytocompatibility of stromal bioinks	72
	10.3.1 Live/Dead	72
	10.3.2 Immunofluorescence staining	74
	10.3.3 Stability of cell-laden stromal structures in LSC medium.....	80
	10.4 Human cornea mimicking structures with stroma and epithelium	82
11.	DISCUSSION	84
	11.1 Characterization of stromal bioinks	85
	11.2 Cytocompatibility of stromal bioinks	91
	11.3 Human cornea mimicking structures with stroma and epithelium	94
	11.4 Future perspectives.....	96
12.	CONCLUSIONS	98
	REFERENCES.....	99

LIST OF SYMBOLS AND ABBREVIATIONS

3D	Three dimensional
ABCG2	ATP binding cassette subfamily G member 2
ALDH 1A1	Aldehyde dehydrogenase 1A1
ALDH 3A1	Aldehyde dehydrogenase 3A1
ALK	Anterior lamellar keratoplasty
AM	Amniotic membrane
ASCs	Adipose tissue -derived stem cells
ATP	Adenosine triphosphate
B-KPro Type I	Boston type I keratoprosthesis
B-KPro Type II	Boston type II keratoprosthesis
BSA	Bovine serum albumin
Ca-AM	Calcein-acetoxymethyl ester
CAD	Computer-aided design
CK15	Cytokeratin 15
Col I	Type I collagen
Col III	Type III collagen
Col IV	Type IV collagen
Col V	Type V collagen
Col VI	Type VI collagen
Col XI	Type XI collagen
Col XII	Type XII collagen
CSK	Corneal stromal keratocyte
CSSCs	Corneal stromal stem cells
CT	Computed tomography
Cx43	Connexin 43
DLP	Dynamic light processing
DMD	Digital mirror device
DoD	Drop-on-demand
DTI	Defined Trypsin Inhibitor
ECM	Extracellular matrix
EGF	Epidermal growth factor
ESCs	Embryonic stem cells
EthD-1	Ethidium homodimer-1
FRESH	Freeform Reversible Embedding of Suspended Hydrogels
GAGs	Glycosaminoglycans
GelMA	Gelatin methacrylate
HA	Hyaluronic acid
HA-ALD	Hyaluronic acid-aldehyde
HA-DA	Hyaluronic acid -based dopamine-containing
HA-DA-CDH	Hyaluronic acid with dopamine and carbodihydrazide modification
HAGM	Hyaluronic acid glycidyl methacrylate
HAMA	Methacrylated hyaluronic acid
hASC-CSKs	Human adipose stem cells -derived corneal stromal keratocytes
hASCs	Human adipose tissue -derived stem cells
hBM-MSCs	Human bone marrow -derived mesenchymal stem cells
hCSCs	Human corneal stromal cells
hCSKs	Human corneal stromal keratocytes
hCS-MSCs	Human corneal stroma -derived mesenchymal stem cells
hESC-LSCs	Human embryonic stem cell -derived limbal epithelial stem cells
hFGF	Human fibroblast growth factor
hPSC-LSCs	Human pluripotent stem cell -derived corneal limbal epithelial stem cells

hTMSCs	Human turbinate derived mesenchymal stem cells
IF	Immunofluorescence
iPSCs	Induced pluripotent stem cells
KDM	Keratocyte differentiation medium
LaBP	Laser-assisted bioprinting
LAP	Lithium phenyl-2,4,6-trimethylbenzoylphosphinate
LCD	Liquid crystal display
LK	Lamellar keratoplasty
LN521	Laminin 521
LSC	Limbal epithelial stem cell
LSCD	Limbal stem cell deficiency
LVER	Linear viscoelastic region
MIPs	Maximum intensity projections
MOOKP	Modified osteo-odonto-keratoprosthesis
MRI	Magnetic resonance imaging
MSCs	Mesenchymal stem cells
OOKP	Osteo-odonto-keratoprosthesis
PAX6	Paired box protein 6
PBS	Phosphate buffered saline
PCL	Polycaprolactone
PEGDA	Poly(ethylene glycol) diacrylate
PFA	Paraformaldehyde
PKP	Penetrating keratoplasty
PLDLA	Poly(L,D lactic acid)
PLK	Posterior lamellar keratoplasty
PMCs	Post-mitotic cells
PMMA	Poly(methyl methacrylate)
PSCs	Pluripotent stem cells
qPCR	Quantitative real-time polymerase chain reaction
RT	Room temperature
SLA	Stereolithography
SLRPs	Small leucine-rich proteoglycans
TACs	Transient amplifying cells
TDCs	Terminally differentiated epithelial cells
TE	Tissue engineering
UV	Ultra-violet
α SMA	α -smooth muscle actin
Δ Np63 α	α isoform of p63

1. INTRODUCTION

The cornea is the transparent outer part of the eye and is composed of five layers of which the two outermost cellular layers are the stroma and epithelium. Together the five layers function to ensure eyesight. (Jia et al., 2023; Sridhar, 2018) However, if these layers are damaged severely, corneal transplantation may be needed (Barrientez et al., 2019). At the moment, corneal transplantation is the primary method for restoring vision but there is a significant shortage of available donor corneas (Gain et al., 2016; Tan et al., 2012). There is an estimated 12.7 million people in line for corneal transplantation while there is only one cornea available for every 70 needed (Gain et al., 2016). Three dimensional (3D) bioprinting is an additive manufacturing technique where tissue-like structures are printed layer-by-layer, and it has been proposed as a promising solution for creating cornea mimicking structures (Balters and Reichl, 2023). In corneal 3D bioprinting, the ultimate goal would be to bioprint the necessary layers needed for transplantation.

3D bioprinting requires cells to create the tissue-like structures but it is not appealing to derive corneal cells from their native origin since the availability of donor corneal tissue is limited (Balters and Reichl, 2023; Gain et al., 2016). Also, primary cell types can be difficult to isolate and culture *in vitro* (Jia et al., 2023). Therefore, stem cells with the potential to become almost any cell type have been explored as a potential cell source for corneal cells (Chakrabarty et al., 2018; Jia et al., 2023; Wang et al., 2023). For the outermost layer of the cornea, the epithelium, human pluripotent stem cell -derived corneal limbal epithelial stem cells (hPSC-LSCs) have been explored as a possible cell source (Hongisto et al., 2017; Mikhailova et al., 2014).

In 3D bioprinting, the tissue-like structure is created using a cell-containing formulation called bioink (Groll et al., 2018). For the thickest layer of the cornea below the epithelium, the stroma (Sridhar, 2018), a suitable hyaluronic acid -based dopamine-containing (HA-DA) stromal bioink has been developed (Mörö et al., 2022). Importantly, for 3D bioprinted structures to become tissue-like, the bioprinted structures are cultured after bioprinting to enable cell growth and maturation (Saini et al., 2021). Moreover, when corneal structures with multiple layers of the cornea are bioprinted, different cell types must be co-cultured after bioprinting. However, the developed HA-DA stromal bioink is not stable in the limbal epithelial stem cell (LSC) medium required to culture hPSC-LSCs and needed

in co-culture after bioprinting, thus restricting the 3D bioprinting of cornea mimicking structures with stroma and epithelium.

To solve this problem, this thesis aimed to enhance the stiffness and stability of the HA-DA stromal bioink in the LSC medium co-culture condition to enable the co-culture of 3D bioprinted cornea mimicking structures with stroma and epithelium. This was explored by modifying the composition of the HA-DA stromal bioink by introducing a methacrylated hyaluronic acid (HAMA) component into the bioink to create a photocrosslinkable HA-DA HAMA stromal bioink. After optimization of the HA-DA HAMA stromal bioink, this bioink was compared to the original HA-DA stromal bioink by characterizing the printability, shape fidelity, viscosity, mechanical properties, transparency, and cytocompatibility of the two bioinks. Based on this comparison, cornea mimicking structures with stroma and epithelium were bioprinted using a different HA-DA stromal bioink for the stroma and a HA-DA bioink specific for the epithelium.

This thesis is composed of a literature review and an experimental part. The literature review starts with introducing the structure and cell types of the human cornea after which corneal diseases, injury, and current treatments are discussed. Then, corneal tissue engineering (TE) approaches along with stem cells are introduced as potential alternatives for current treatments. Subsequently, 3D bioprinting and its multiple approaches are discussed before introducing bioinks used in 3D bioprinting, their crosslinking, and characterization. The literature review is concluded with a review of previous studies conducted in corneal 3D bioprinting. The experimental part of this thesis starts by specifying the aims of this thesis and is followed by a description of the materials and methods used. Finally, the obtained results are presented and discussed, and the main findings of this thesis are concluded.

2. HUMAN CORNEA

The cornea is the transparent outer part of the eye. Together with the sclera, the cornea forms the exterior coat of the eyeball. (Sridhar, 2018) The cornea has three major functions. Firstly, the cornea functions as a structural barrier by protecting the inner structures of the eye (Jia et al., 2023; Sridhar, 2018). Secondly, the cornea functions as a “window” by transmitting light into the eye (Jia et al., 2023). Lastly, the cornea functions as a “focusing lens” by focusing light rays with minimum scatter and optical degradation to the retina and by contributing to two-thirds of the refractive power of the eye (Jia et al., 2023; Sridhar, 2018).

The cornea is an avascular (Sridhar, 2018) and immune-privileged (Taylor, 2009) tissue with a curved shape (Sridhar, 2018). The thickness of normal cornea ranges between 551 – 565 μm in the central cornea and increases towards the periphery being 612 – 640 μm in the peripheral cornea (Feizi et al., 2014; Sridhar, 2018). The diameter of a normal adult cornea is between 11.04 – 12.50 mm for males and 10.70 – 12.58 mm for females (Rüfer et al., 2005). Furthermore, the cornea has high transparency with light transmittance values varying between 80 – 94% at wavelengths 450 – 600 nm and between 95 – 98% at wavelengths 600 – 1000 nm (Beems and Van Best, 1990).

Next, the structure of the corneal tissue is introduced following which corneal cell types are discussed, focusing on the cell types used in this thesis. Finally, corneal defects and current treatments are briefly considered.

2.1 Structure of the cornea

The corneal tissue contains five layers: epithelium, Bowmans’s layer, stroma, Descemet’s membrane and endothelium (Sridhar, 2018) (Figure 1). The epithelium, stroma and endothelium are cellular layers whereas the Bowmans’s layer and Descemet’s membrane are acellular interfaces (Jia et al., 2023).

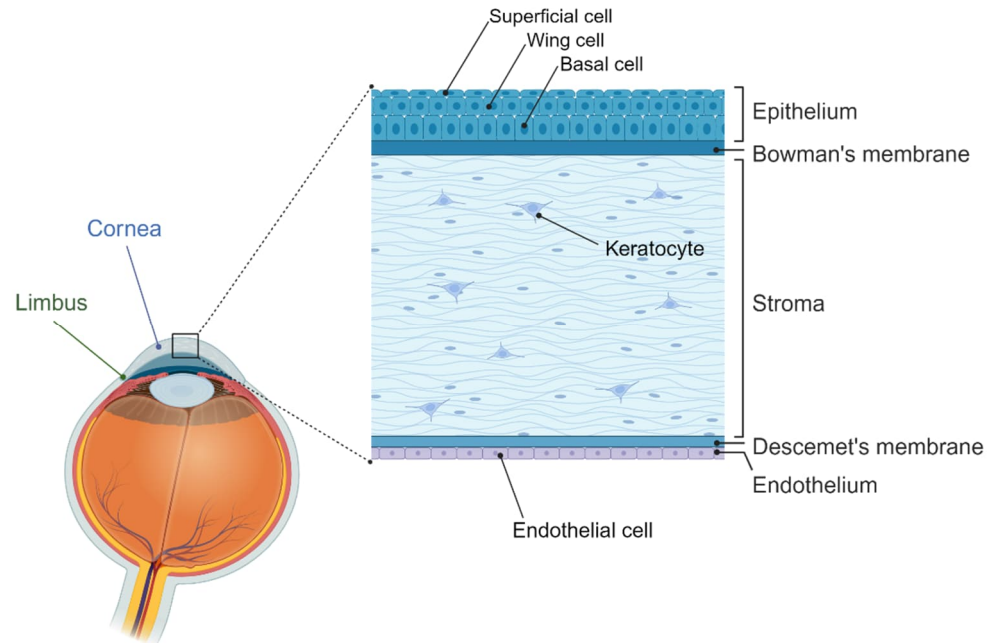


Figure 1. Illustration of the human eye and a cross-section of the cornea depicting its five layers and different cell types. Modified from Osei-Bempong et al. (2013) and Sridhar (2018). Created with BioRender.com.

The epithelium is the anterior layer of the cornea and is covered with a tear film (DelMonte and Kim, 2011). The epithelium transports nutrients and oxygen from the corneal surface, helps to maintain a smooth optical surface required for optimal vision, and functions as a barrier to protect the stroma from physical, chemical, and biological agents (Jia et al., 2023). The epithelium is approximately 50 μm thick and composed of 5 – 7 layers of nonkeratinized stratified squamous epithelial cells (Sridhar, 2018). Epithelial cells have a lifespan of 7 – 10 days which results in the complete turnover of the epithelium each week (DelMonte and Kim, 2011). The transparency of the epithelium is due to the epithelial cells containing cytoplasmic crystallin proteins, crystallins (Jester, 2008; Sridhar, 2018), and due to having similar refractive indexes between epithelial cell types (Meek and Knupp, 2015, p. 2).

The epithelium is composed of superficial cells, wing cells, and basal cells which are attached to each other through desmosomes (Sridhar, 2018). Superficial cells form 2 – 3 layers of flat polygonal cells and have tight junctions to prevent tears, toxins and microbes from entering the eye (DelMonte and Kim, 2011; Sridhar, 2018). Superficial cells also have apical microvilli to increase surface area and therefore adhesion to the tear film (DelMonte and Kim, 2011). Under the superficial cells, less flat wing-shaped wing cells create 2 – 3 layers of epithelium (DelMonte and Kim, 2011; Sridhar, 2018). Beneath the wing cells, basal cells form a single cell layer which is columnar in the central and cuboidal in the peripheral cornea (Sridhar, 2018). The basal cells are attached to an

underlying basement membrane by hemidesmosomes (DeMonte and Kim, 2011; Sridhar, 2018). This 40 – 60 nm thick basement membrane is composed of type IV collagen (Col IV) and laminin secreted by the basal cells and attaches the epithelium to the underlying layers of the cornea (Sridhar, 2018).

Bowmans's layer is below the epithelium, anterior to the stroma, and assists in maintaining the shape of the cornea. It is 12 µm thick and composed of type I and V collagen (Col I and Col V) and proteoglycans. (Sridhar, 2018) Since the Bowmann's layer is thin, light scattering is minimal and the layer is transparent (Meek and Knupp, 2015). However, the Bowmans's layer does not regenerate and therefore when injured may result in a scar (Sridhar, 2018). Yet, the absence of the Bowmans's layer does not appear to have an impact on corneal function (Espana and Birk, 2020, p. 2).

The stroma provides mechanical strength, refractive power, and transparency to the cornea. The stroma is the thickest layer of the cornea accounting for 80 – 85 % of its thickness. Increased thickness in the periphery of the cornea is due to increased amounts of collagen in the peripheral stroma whereas rigidity of the anterior stroma is important in the maintenance of the corneal curvature. The transparency of the stroma is due to a precise organization of collagen fibers and extracellular matrix (ECM). (Sridhar, 2018) The collagen fibers are assembled from parallel bundles of collagen fibrils which form lamellae (DeMonte and Kim, 2011; Espana and Birk, 2020). The lamellae form an orthogonal arrangement where adjacent lamellae are oriented at approximately 90° from each other (Espana and Birk, 2020). The stroma of the human eye contains 200 – 250 of these orthogonal lamellae (Sridhar, 2018). The fibrils are mainly formed from Col I, but the regulatory fibril-forming collagens Col V and type XI collagen (Col XI) are also present (Espana and Birk, 2020, p. 5).

The major cell type of the human stroma is human corneal stromal keratocytes (hCSKs) (Sridhar, 2018; Yam et al., 2020). The hCSKs are mainly located between the collagen lamellae keeping the lamellae in place (Downie et al., 2021). The hCSKs maintain the stroma ECM and synthesize collagen molecules as well as glycosaminoglycans (GAGs). The stroma ECM is composed of these collagens including Col I, type III collagen (Col III), Col V, type VI collagen (Col VI) and type XII collagen (Col XII) as well as GAGs including mainly keratan sulfate, but also chondroitin sulfate, and dermatan sulfate. (Sridhar, 2018) When attached to a core protein, these GAGs form small leucine-rich proteoglycans (SLRPs). SLRPs expressed in the corneal stroma are decorin, biglycan, lumican, keratocan, fibromodulin, and osteoglycin. These SLRPs regulate the assembly of collagen fibrils, maintain stromal hydration by binding water to the attached GAGs, as

well as modulate and tether growth factors. (España and Birk, 2020). SLRPs are also important for the transparency and integrity of the cornea (Yam et al., 2020, p. 3).

The Descemet's membrane is located between the stroma and endothelium. It is 7 μm thick and composed of Col IV and laminin. (Sridhar, 2018) The Descemet's membrane is transparent due to its thinness causing minimal light scattering (Meek and Knupp, 2015). Endothelial cells constantly secrete the Descemet's membrane and adhere to it (Sridhar, 2018).

The innermost layer of the cornea is the endothelium. It removes water from the stroma to maintain corneal clarity. Endothelial cells arrange in a 5 μm thick honeycomb-like mosaic monolayer, do not regenerate in adults and cell density decreases during adult life. (Sridhar, 2018)

In the periphery of the cornea, the cornea turns into the sclera via a transitional zone known as the limbus. The limbus is 1.5 – 2.0 mm wide and anatomically complex. (Downie et al., 2021) The limbus contains limbal epithelial stem cells (LSCs) which are responsible for corneal epithelial regeneration since the constant renewal of the epithelium requires a peripheral influx of cells from the limbus (Downie et al., 2021, p. 134; Gonzalez et al., 2018; Saghizadeh et al., 2017). The corneal epithelium is continuous with limbal epithelium which is subsequently continuous to the conjunctival epithelium covering the sclera. Therefore, the limbus also acts as a physical barrier ensuring that the conjunctival cells do not proliferate into the corneal epithelium. (Downie et al., 2021)

2.2 Corneal cell types

As discussed, each cellular layer of the human cornea contains characteristic cells: epithelial cells reside in the epithelium, the stroma contains hCSKs and the endothelium is composed of endothelial cells (Sridhar, 2018). In addition, the cornea contains stem cells of which LSCs reside in the limbus (Dziasko and Daniels, 2016) and corneal stromal stem cells (CSSCs) in the anterior peripheral stroma near the LSCs (Pinnamaneni and Funderburgh, 2012; Yam et al., 2020). Next, hCSKs and LSCs are discussed in more detail since they are the cell types relevant for the experimental part of this thesis.

2.2.1 Human corneal stromal keratocytes

As the major cell type of the stroma, the human cornea has approximately 2.4 million non-uniformly distributed hCSKs with a higher density of hCSKs at the anterior of the stroma (Downie et al., 2021; Møller-Pedersen et al., 1994). Besides synthesizing collagens and GAGs, hCSKs mediate intra-corneal communications, act as an energy source

by storing glycogen, have phagocytic functions and contribute to wound healing (Downie et al., 2021, p. 135; Sridhar, 2018; Yam et al., 2020, p. 1,3).

The hCSKs are anchored between the collagen lamellae of the stroma and are mitotically quiescent (España and Birk, 2020; Yam et al., 2020). hCSKs are thin and dendritic, having long and branching cellular processes (Yam et al., 2020). These processes are connected to cell bodies or cytoplasmic extensions of other hCSKs via gap junctions to enable cell-to-cell communication (Downie et al., 2021, p. 135; Yam et al., 2020). hCSKs have distinct nuclei and most of the cell volume is occupied by the cytoplasm (Yam et al., 2020). hCSKs appear transparent due to crystallins in the cytoplasm which limit light scattering and allow the hCSKs to match the refractive index of the surrounding stroma (Jester, 2008; Yam et al., 2020).

Distinctive molecular markers expressed by hCSKs include proteoglycans keratocan and lumican as well as crystallins such as aldehyde dehydrogenases 1A1 and 3A1 (ALDH 1A1, 3A1) (España and Birk, 2020, p. 4; Yam et al., 2020, p. 4). Furthermore, hCSKs express collagen-binding integrins $\alpha 2\beta 1$, $\alpha 3\beta 1$, $\alpha 5\beta 1$, and $\alpha 6\beta 1$ which contribute to stromal integrity by interacting with the ECM. However, hCSKs are negative for α -smooth muscle actin (α SMA) and fibroblast genes such as fibronectin, tenascin and CD90. (Yam et al., 2020, pp. 3–4)

2.2.2 Limbal epithelial stem cells

LSCs are a quiescent cell population with high proliferative capacity, and therefore are responsible for the continuous regeneration and repair of the corneal epithelium (Dziasko and Daniels, 2016; Gonzalez et al., 2018). Within the limbus, LSCs reside in a unique microenvironment called the limbal niche (Dziasko and Daniels, 2016). The limbal niche contains ridges called Palisades of Vogt which extend into limbal epithelial crypts where the LSCs reside in the basal epithelial layer (Dua et al., 2005; Dziasko and Daniels, 2016; Gonzalez et al., 2018). The proliferation and differentiation potential of LSCs is regulated by the distinct anatomical features, biomechanical properties, specific composition of the ECM, secreted soluble factors, and other cell types residing in the limbal niche (Dziasko and Daniels, 2016).

To regenerate the corneal epithelium, LSCs proliferate in the basal epithelial layer of the limbal niche and give rise to transient amplifying cells (TACs) (Saghizadeh et al., 2017; Yazdanpanah et al., 2019). As TACs migrate from the limbus to the center of the cornea, TACs divide into post-mitotic cells (PMCs) which differentiate into terminally differentiated epithelial cells (TDCs) (Gonzalez et al., 2018; Saghizadeh et al., 2017; Yazdanpanah et al., 2019). This theory behind the maintenance of the corneal epithelium

was proposed in 1993 by Thoft and Friend in the X-Y-Z hypothesis. In the hypothesis, X depicts the proliferation of basal cells, Y the migration of cells towards the center of the cornea and Z the loss of epithelial cells from the surface. (Thoft and Friend, 1983) This theory of corneal epithelial cell maintenance by LSCs is presented in Figure 2.

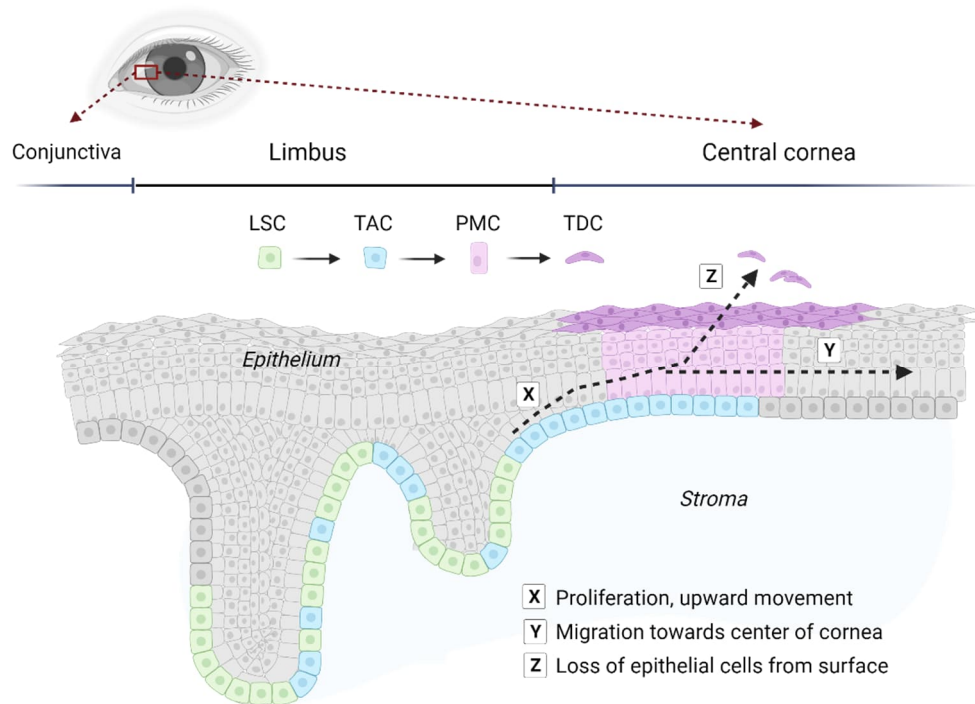


Figure 2. Corneal epithelial cell maintenance by LSCs. LSCs proliferate in the basal epithelial layer of the limbal niche and give rise to TACs (X). As they migrate first horizontally along the basement membrane then diagonally through the epithelial layers (Y) TACs divide into PMCs before reaching the surface as TDCs. Finally, TDCs are shed from the corneal surface (Z). Modified from Saghizadeh et al. (2017), Schlötzer-Schrehardt and Kruse (2005) and Yazdanpanah et al. (2019). Created with BioRender.com

Currently, there is no single specific biomarker to identify true LSCs (Kauppila et al., 2023; Vattulainen et al., 2019). A widely acknowledged biomarker for putative LSCs is adenosine triphosphate (ATP) binding cassette subfamily G member 2 (ABCG2) (Schlötzer-Schrehardt and Kruse, 2005; Vattulainen et al., 2019). Other markers expressed by LSCs include, but are not limited to, paired box protein 6 (PAX6), a master regulatory gene involved in eye development, the alpha isoform of p63 ($\Delta Np63\alpha$), a transcription factor, as well as cytokeratin 15 (CK15) (Di Iorio et al., 2005; Dziasko and Daniels, 2016; Kauppila et al., 2023; Li et al., 2015; Vattulainen et al., 2019).

3. CORNEAL BLINDNESS

Corneal diseases and injury are one of the main causes of blindness (Zhang et al., 2019b). Next, corneal diseases and injury as well as current treatment alternatives are discussed focusing on the epithelial and stromal layer.

3.1 Corneal diseases and injury

As the outermost layer of the eye, the cornea is at risk of traumatic injury (Guérin et al., 2021, p. 4). The cornea can be damaged by chemical burns, lodged foreign bodies and lacerations or perforations. Corneal lacerations are often caused by high-speed flying objects while corneal perforations can be caused by foreign objects, microbial keratitis, or immune disorders. In corneal lacerations the injury penetrates both the epithelium and the stroma whereas in corneal perforations also the endothelium is pierced along with the epithelium and stroma. (Barrientez et al., 2019) Besides injury to the different corneal layers, chemical burns as well as mechanical and thermal injuries can also damage the limbus. This can result in the loss of LSCs which leads to limbal stem cell deficiency (LSCD). (Barrientez et al., 2019; Saghizadeh et al., 2017)

After injury to the cornea, wound healing mechanisms are activated. When the corneal injury involves only the epithelium, the healing process is usually rapid. (Barrientez et al., 2019) If the epithelium is damaged, epithelial cells at the edge of the wound migrate and spread to cover the wounded area (DeMonte and Kim, 2011). Moreover, with large wounds, LSCs proliferate and produce TACs which divide and differentiate as they migrate from the limbus towards the center of the cornea to restore the epithelium. However, if LSCs are damaged or lost, the consequent LSCD results in the ingrowth of the conjunctiva along with neovascularization leading to corneal opacity and vision loss. (Saghizadeh et al., 2017)

When the corneal stroma is also injured, the wound healing is more complex (Barrientez et al., 2019). Upon injury to the stroma, the hCSKs in the injured site undergo apoptosis (DeMonte and Kim, 2011). Additionally, when the epithelial basement membrane and/or Descemet's membrane are damaged, pro-fibrotic cytokines are present in the stroma at high levels and can trigger the transformation of surviving hCSKs into corneal fibroblasts. If the regeneration of either membrane is delayed, these fibroblasts develop into mature

α SMA positive myofibroblasts which are able to secrete significant amounts of disordered ECM. (Wilson, 2020) The disordered ECM results in corneal fibrosis, also termed corneal scarring, which can impair clear vision (Barrientez et al., 2019; Wilson, 2020).

In addition to traumatic injury, various degenerative, dystrophic, infectious and inflammatory corneal disorders can result in corneal blindness (Tan et al., 2012). For example, keratoconus is a progressive disease of the cornea where the stroma suffers gradual thinning and deterioration of its structural integrity. This results in the bulging of the cornea which appears as a cone-shaped cornea leading to poor vision. (Barrientez et al., 2019, p. 4) Another disease of the cornea is Fuchs' endothelial corneal dystrophy which is a progressive hereditary disease where the corneal endothelium is dysfunctional. The dysfunctional endothelium is not able to correctly regulate fluid absorption of the cornea, and this causes fluid buildup into the stroma resulting in swelling and hazy vision. (Barrientez et al., 2019; Hemaya et al., 2023) In addition, LSCD may be caused by genetic or chronic diseases, and lead to vision loss as discussed earlier (Saghizadeh et al., 2017). Moreover, changes in one or more layers of the cornea due to corneal pathologies can result in increased light scattering which can lead to the loss of corneal transparency. For example, several different corneal dystrophies, such as lattice dystrophy, are associated with opacities which are caused by different types of stromal deposits. (Meek and Knupp, 2015)

3.2 Current Treatments

When the corneal injury or disease is very severe and when initial measures have failed, corneal transplantation, also termed keratoplasty, may be needed to restore vision (Barrientez et al., 2019). Corneal transplantation procedures can be divided into full-thickness penetrating keratoplasty (PKP) and selective lamellar keratoplasty (LK) (Singh et al., 2019; Tan et al., 2012). In contrast to PKP where all five layers of the cornea are replaced by a donor cornea, in LK, only diseased layers of the cornea are replaced while healthy layers are preserved (Singh et al., 2019; Tan et al., 2012). LK can be roughly divided into anterior lamellar keratoplasty (ALK) and posterior lamellar keratoplasty (PLK) depending on which layers of the cornea will be replaced (Singh et al., 2018, 2019). In ALK, the epithelium and all or part of the stroma are replaced with donor tissue while the patient's endothelium is spared (Singh et al., 2019; Tan et al., 2012). Instead, in PLK, only the Descemet's membrane and endothelium are removed and replaced with donor equivalents with or without an additional thin strip of stroma. When compared to LK, PKP is associated with an increased risk of many complications. (Tan et al., 2012) For example, a major cause of graft failure in PKP is endothelial allograft rejection which is eliminated

in ALK since the endothelium is preserved (Singh et al., 2018; Tan et al., 2012). Therefore, when a suitable treatment option, LK has replaced PKP in most specialist centers (Singh et al., 2018).

Corneal transplantation is the primary method for restoring vision after corneal clarity has been compromised but requires corneal donor tissue (Tan et al., 2012). This is a significant constraint due to the shortage of corneal donor tissue. There is only 1 cornea available for every 70 needed, and an estimated 12.7 million people waiting for corneal transplantation. (Gain et al., 2016) Moreover, in patients suffering from LSCD, the lack of LSCs for epithelial regeneration can result in transplant failure (Pellegrini et al., 2013). Therefore, alternative treatment options have been explored.

Keratoprotheses are artificial corneas where a transparent optical cylinder is surrounded by a skirt or collar button. The optical cylinder allows light to pass whereas the skirt or collar button integrates the keratoprosthesis with the host corneal tissue. (Jia et al., 2023; Zhang et al., 2019b) Keratoprotheses are often made of non-degradable and bioinert materials to maintain function and to improve stability *in vivo* (Zhang et al., 2019b). There are several different kinds of keratoprotheses available of which the most common are the Boston type I and II keratoprotheses (B-KPro Type I, B-KPro Type II) as well as the osteo-odonto-keratoprosthesis (OOKP) and the modified OOKP (MOOKP) (Iyer et al., 2018; Salvador-Culla and Kolovou, 2016). The B-KPro Type I has a collar button design and is implanted into a carrier corneal graft. The device is made from an anterior plate composed of poly(methyl methacrylate) (PMMA), containing the optical cylinder, and from a snap-on titanium back plate. The donor cornea is placed between the two plates and the complex is implanted into the patient's eye. The B-KPro Type II is similar to the B-KPro Type I, but the anterior plate penetrates through the upper eyelid or between both eyelids. (Salvador-Culla and Kolovou, 2016) Instead, the OOKP and MOOKP use an optical PMMA cylinder which is inserted into the patient's tooth that functions as a carrier. The procedure requires multiple complex surgeries and is performed in only a few centers worldwide. (Salvador-Culla and Kolovou, 2016; Tan et al., 2012) Yet keratoprotheses have several disadvantages: the visual field is limited, the implantation process is complex, the skirt or button is non-transparent making the appearance unaesthetic and the keratoprosthesis may be uncomfortable to wear due to the implant materials being often hard (Zhang et al., 2019b). Therefore, current keratoprosthesis options are not ideal alternatives for transplants (Jia et al., 2023) and are used as last-resort options in the treatment of end-stage corneal blindness when conventional corneal surgery is likely to fail (Iyer et al., 2018; Tan et al., 2012).

Due to the lack of donor tissue (Gain et al., 2016) and several drawbacks of keratopros-theses (Zhang et al., 2019b), TE and stem cell therapy have been researched as possible alternative solutions (Barrientez et al., 2019). These new treatment approaches are discussed further in the following chapter, Chapter 4.

4. CORNEAL TISSUE ENGINEERING

TE was defined in 1993 by Langer and Vacanti as “an interdisciplinary field that applies the principles of engineering and the life sciences toward the development of biological substitutes that restore, maintain, or improve tissue function” (Langer and Vacanti, 1993). As TE aims to develop substitutes for damaged tissue (Langer and Vacanti, 1993), corneal TE has the potential to overcome the shortage of donor corneas (Barrientez et al., 2019). The cornea is an attractive target for TE since the corneal tissue is avascular and immune-privileged (Fuest et al., 2020). As an immune-privileged tissue, rejection and inflammatory responses are less likely than in other tissues (Fuest et al., 2020, p. 3). Nevertheless, there are several requirements that TE corneal substitutes should meet. These include transparency, curvature, sufficient mechanical properties, and appropriate biological function of cells (Fuest et al., 2020, pp. 5–6).

To create biological corneal substitutes, TE utilizes scaffolds, cells, and biomolecules such as growth factors (Bakhshandeh et al., 2017; Tafti et al., 2022). Scaffolds are 3D structures designed to mimic the functions of natural ECM, at least partly (Chan and Leong, 2008; Nikolova and Chavali, 2019). Scaffolds are constructed from biomaterials, defined as materials designed to direct the course of a therapeutic or diagnostic procedure through interactions with living systems (Ghasemi-Mobarakeh et al., 2019; Ovsianikov et al., 2018). One of the most common biomaterials used for scaffolds in TE are hydrogels as they can retain their 3D structure, provide mechanical support for cells as well as mimic natural ECM (Mantha et al., 2019). Hydrogels are discussed in detail in Chapter 6 along with bioinks. As for cells, several different cell types have been used, but stem cells are one of the most promising due to their self-renewal ability (Bakhshandeh et al., 2017). Therefore, stem cells and their application as a possible cell source for corneal epithelial and stromal TE are discussed in Chapter 4.3.

Generally, TE can be divided into scaffold-free and scaffold-based approaches (Matthyssen et al., 2018). In scaffold-free, i.e., cell-based, approaches, cells have the primary role in the TE construct whereas scaffold-based approaches combine biomaterials, cells and biomolecules to create functional scaffolds that support cellular function (Hussain and Pei, 2021; Matthyssen et al., 2018). Next, in Chapters 4.1 and 4.2 scaffold-free and scaffold-based approaches are introduced, respectively.

4.1 Scaffold-free approaches

Scaffold-free approaches are often used for epithelial and endothelial TE since they are composed of only a few cell layers and closely combined with the basal layers of the cornea *in vivo* (Matthyssen et al., 2018). Scaffold-free approaches used for corneal TE include cellular spheroids, cell-suspensions, and cell-sheets (Hussain and Pei, 2021).

Spheroids are defined as “cell aggregates, self-assembling in an environment that prevents attachment to a flat surface” (Białkowska et al., 2020). Cell spheroids are used as building blocks in scaffold-free TE since they allow intense cell-to-cell interactions and mimic other physiological conditions of complex tissues (Ovsianikov et al., 2018). Multi-lineage-differentiating stress enduring spheroids have been used as a cell source for human corneal stromal cells (hCSCs) and were used for the treatment of corneal scarring in a mouse model with promising results (Guo et al., 2020).

In cell-suspension approaches, the cell suspension is injected into the transplantation site (Hussain and Pei, 2021). Cell-suspension approaches have been used in corneal stromal TE. Alió Del Barrio et al. (2017) injected autologous human adipose tissue-derived stem cells (hASCs) into the corneal stroma of patients with advanced keratoconus and found that the treatment showed moderate improvement of visual acuity in patients three years after the procedure (Alió Del Barrio et al., 2017; El Zarif et al., 2021). Injecting cells into the corneal stroma is a simple strategy for stromal reconstruction, but it can disrupt the precise organization of collagen fibers and is ineffective for the reconstruction of severely damaged stroma since the cell-suspension does not include a supportive matrix and cells are localized poorly (Hussain and Pei, 2021).

In cell-sheet approaches, intact cells sheets are harvested after culturing cells on a responsive surface that allows the produced cell sheet to detach along with their ECM (G. Chen et al., 2015; Hussain and Pei, 2021). Cell-sheet approaches have been utilized in stromal reconstruction. Human CSSCs were cultured on microgrooved substrates which enabled the production of cell sheets with ECM organization mimicking the native human stroma (Syed-Picard et al., 2018). Once implanted into mouse stromal pockets, the cell sheets were incorporated into the surrounding tissue and became transparent (Syed-Picard et al., 2018). Moreover, cell sheets have been utilized in stromal TE by stacking hCSK cell sheets to create thicker stromal structures (Gouveia et al., 2017). Additionally, cell-sheet approaches have been used to repair the corneal epithelium in patients with LSCD (Burillon et al., 2012; Pellegrini et al., 1997). Pellegrini et al. (1997) used autologous LSC cell sheets which were expanded *ex vivo* before transplantation. A product called Holoclar based on this *ex vivo* expansion of autologous LSCs was authorized for

use in the European Union in 2015 (Deng et al., 2020; EMA, 2018). However, in bilateral LSCD, where both eyes are damaged, sufficient amounts of LSCs may not be present for *ex vivo* expansion of autologous LSCs (Deng et al., 2020). To overcome this limitation, Burillon et al. (2012) treated patients with cultured autologous oral mucosal epithelial cell sheets with promising results. Nonetheless, a drawback of cell sheet approaches is the delicate structure of the ultrathin cell-sheets therefore causing difficulty in handling during transplantation (Hussain and Pei, 2021). Consequently, cell-sheet approaches may need carrier materials to ease transplantation such as the fibrin membrane used in Holoclar (EMA, 2018; Hussain and Pei, 2021).

Generally, in the scaffold-free approach, reaching sufficient mechanical properties is a concern. However, high initial cell density and the possibility of tissue self-assembly are major advantages which, in contrast, cannot be achieved with the scaffold-based approaches introduced in the next chapter, Chapter 4.2. (Ovsianikov et al., 2018)

4.2 Scaffold-based approaches

A major advantage of scaffold-based approaches is that adequate mechanical properties can be achieved (Ovsianikov et al., 2018). This is particularly important in stromal TE since the stroma accounts for most of the thickness of the cornea. Therefore, scaffold-based approaches are more commonly used in stromal regeneration. (Matthyssen et al., 2018) Scaffold-based approaches rely on biomaterials to create a temporary structure that supports cells during tissue formation. The scaffold provides a biomimetic environment for the cells as well as the possibility of delivery and controlled release of biomolecules. Therefore, the properties of the biomaterial largely influence the functionality of the scaffold. (Ovsianikov et al., 2018) These biomaterials can be divided into synthetic and natural biomaterials of which synthetic biomaterials have better mechanical properties but lack cell binding sites (Mahdavi et al., 2020b). Examples of synthetic biomaterials used in corneal TE include synthetic polymers such as polycaprolactone (PCL) and poly(L,D lactic acid) (PLDLA) (Chen et al., 2018). Instead, natural biomaterials are derived from natural sources and have gained interest in corneal TE due to their biocompatibility and cell binding sites. Nevertheless, natural biomaterials often have poor mechanical properties and a high degradation rate. (Mahdavi et al., 2020b) Examples, of natural biomaterials include amniotic membrane (AM), decellularized cornea and collagen (Mahdavi et al., 2020b), which are introduced next.

A well-known natural biomaterial used in ophthalmology is AM (Jirsova and Jones, 2017). AM is the innermost layer of the placenta composed of a monolayered epithelium, a basement membrane and a three-layer avascular stroma (Jirsova and Jones, 2017;

Nejad et al., 2021). AM is widely used in corneal regeneration applications due to being translucent and having anti-inflammatory as well as anti-microbial properties (Jirsova and Jones, 2017; Le and Deng, 2019). Also, as the collagen composition of the basement membrane of the AM is similar to the one in the cornea, AM is a suitable substrate for corneal epithelial cells to grow on (Jirsova and Jones, 2017). In addition to using AMs alone as grafts in ophthalmology (Jirsova and Jones, 2017; Le and Deng, 2019), AMs have been utilized for both corneal epithelial and stromal TE. In corneal epithelial TE, AMs have been used as substrates and carriers for *ex vivo* cultured LSCs in patients with bilateral LSCD (Le and Deng, 2019). Instead in corneal stromal TE, Che et al. (2019) created a corneal stromal structure by culturing hCSCs on ultrathin AMs and then stacking these AMs to form a multilayered structure. The hCSCs in the AM-hCSC-structures secreted ECM with a microstructure similar to the human cornea (Che et al., 2019). Despite the several advantages of AM, disadvantages include batch-to-batch variation, possible disease transmission, and suboptimal transparency (Hussain and Pei, 2021).

Another natural biomaterial that has received attention in corneal TE is decellularized cornea (Hussain and Pei, 2021). In decellularization, cells are removed with biological, physical or chemical processes from the donor tissue leaving behind the ECM which can be utilized as a scaffold (Matthyssen et al., 2018). The decellularized cornea can be recellularized before transplantation. For example, Alió del Barrio et al. (2018) transplanted decellularized human corneal stroma sheets recellularized with autologous hASCs into the corneal stroma of patients with advanced keratoconus and found that the treatment showed moderate visual and refractive improvement in patients three years after the procedure (Alió del Barrio et al., 2018; El Zarif et al., 2021). The major advantage of decellularized cornea is that the native ECM is preserved thereby giving the scaffold the biochemical composition and tissue structure of the native cornea (Mantha et al., 2019). However, as decellularized cornea is based on donor tissue, limitations include batch-to-batch variation and possible disease transmission. Moreover, the proliferation of hCSKs inside decellularized corneas is challenging. (Hussain and Pei, 2021)

In addition to AM and decellularized cornea, various other biomaterials have been used as scaffolds for corneal TE. Especially, collagen-based biodegradable scaffolds have been researched for corneal stromal regeneration (Hussain and Pei, 2021; Matthyssen et al., 2018). Often Col I and III have been used in the form of hydrogels since the corneal stroma is naturally a hydrogel mostly composed of collagen (Matthyssen et al., 2018). As an example, crosslinked recombinant human Col III cell-free hydrogel scaffolds, were implanted into patients by ALK and promoted regeneration of corneal tissues and nerves

at four years (Fagerholm et al., 2014). Also, collagen sponges and films have been utilized in corneal stromal TE (Crabb and Hubel, 2008; Matthyssen et al., 2018; Orwin et al., 2003). To improve the mechanical properties of collagen scaffolds, collagen has been used with other biomaterials (Matthyssen et al., 2018). For example, electrospun PLDLA nanofiber meshes were incorporated into Col I hydrogels in a corneal stromal model (Wilson et al., 2012). Other biomaterials utilized in corneal TE include, but are not limited to, gelatin (Shirzaei Sani et al., 2019), silk fibroin (Wang et al., 2017), and hyaluronic acid (HA) (Koivusalo et al., 2019).

Widely used conventional scaffold fabrication techniques include electrospinning, freeze-drying, liquid molding, and particulate leaching (Tafti et al., 2022). However, creating scaffolds with specific tissue characteristics mimicking the natural ECM both structurally and functionally is challenging, and conventional fabrication techniques are not able to provide the precise positioning of multiple cell types needed for the creation of functional tissues (Cui et al., 2020; Tafti et al., 2022). To overcome these challenges, 3D bioprinting has been extensively studied in recent years, and will be discussed in Chapter 5.

4.3 Stem cells as cell source for corneal tissue engineering

Stem cells are unspecialized cells of the human body that have self-renewal ability and can differentiate into several cell types (Rajabzadeh et al., 2019; Zakrzewski et al., 2019). Therefore, stem cells hold great potential for TE (Si et al., 2019). Stem cells can be classified based on their differentiation ability (Rajabzadeh et al., 2019). Totipotent stem cells have the highest differentiation potential and can differentiate into any cell type found in the organism (Rajabzadeh et al., 2019; Zakrzewski et al., 2019). Pluripotent stem cells (PSCs) can form cells of all three germ layers, endoderm, mesoderm, and ectoderm whereas multipotent stem cells can differentiate into cell types of only one germ layer. Instead, unipotent stem cells have the narrowest differentiation capabilities and can differentiate into only one cell type. (Zakrzewski et al., 2019)

In addition to corneal -derived stem cells, LSCs and CSSCs, non-corneal -derived stem cells can be utilized in corneal TE including PSCs and mesenchymal stem cells (MSCs) (Wang et al., 2023). PSCs include embryonic stem cells (ESCs) and induced PSCs (iPSCs) (Zakrzewski et al., 2019). From the two, ESCs are derived from the inner cell mass of preimplantation embryos and therefore a source of ethical conflict (Thomson et al., 1998; Zakrzewski et al., 2019). Instead, iPSCs can be reprogrammed from adult somatic cells and thus do not possess the same ethical concerns as ESCs (Chakrabarty et al., 2018; Takahashi et al., 2007). PSCs can provide an almost unlimited cell source due to their self-renewal ability and capability to differentiate into desired cell types (Zakrzewski

et al., 2019). Thus, PSCs have also been researched for corneal TE. For the epithelial layer of the cornea, in 2007, Ahmad et al. produced the first human PSC-derived corneal epithelial-like cells (Ahmad et al., 2007). Since then, hPSC-LSCs and epithelial cells have been produced with several different protocols (Hayashi et al., 2016; He et al., 2020; Hongisto et al., 2017; Mikhailova et al., 2014). Corneal epithelial cell sheets derived from iPSCs have been used for the treatment of LSCD in first-in-human clinical trials in Japan (Osaka University, 2019; WHO, 2023). For the stromal layer of the cornea, hCSK differentiation using human PSC has also been reported (Chan et al., 2013; Naylor et al., 2016).

MSCs are multipotent stem cells found in various adult tissues (Ullah et al., 2015). A subset of MSCs, are hASCs which can be easily obtained from adipose tissue. In addition, hASCs can be expanded *in vitro*, have immunomodulatory properties, and have the capacity to differentiate into multiple cell lineages. (Si et al., 2019) For example, hASCs have been successfully differentiated towards CSKs (hASC-CSKs) *in vitro* and *in vivo* (Du et al., 2010; Espandar et al., 2012). Due to these multiple advantages, hASCs have been utilized for corneal stromal TE. Alió Del Barrio et al. used hASCs in both scaffold-free and scaffold-based approaches for corneal stroma with promising results in patients with advanced keratoconus as discussed in Chapters 4.1 and 4.2 (Alió del Barrio et al., 2018; Alió Del Barrio et al., 2017; El Zarif et al., 2021). Also, hASCs as well as hASC-CSKs have been utilized for example in 3D bioprinting of corneal stromal structures (Mörö et al., 2022).

5. 3D BIOPRINTING

3D bioprinting is an additive manufacturing technique where tissue-like constructs are printed from cells and biomaterials layer-by-layer (Mandrycky et al., 2016; Schwab et al., 2020). 3D bioprinting holds huge potential for TE since the approach enables the automated fabrication of cell-containing structures with high resolution and hierarchical organization (Schwab et al., 2020). In 3D bioprinting, a bioink is deposited by the 3D bioprinter to create the desired structure (Schwab et al., 2020) and will be discussed further in Chapter 6.

A typical 3D bioprinting procedure is composed of the following steps. First, the 3D model to be printed is created using computer-aided design (CAD). The 3D model can be designed with graphic user interfaces or created from clinical images such as images acquired from magnetic resonance imaging (MRI) or computed tomography (CT). Next, the 3D model is converted to a stereolithography (STL) file which is then sliced to create layers that will be printed by the bioprinter. Within layers, bioprinter toolpaths are created to design the outline and inner features of each slice. After creating the 3D model and bioprinter tool paths, suitable cell types and biomaterials are selected for the bioink. Following these steps, 3D bioprinting can be performed by the bioprinter. After bioprinting, the bioprinted tissues are cultured *in vitro* for further analysis. (Mandrycky et al., 2016) The *in vitro* culture allows the growth and maturation of the bioprinted tissue before possible *in vivo* implantation (Saini et al., 2021).

Several different 3D bioprinting techniques exist since no single 3D bioprinting technique is able to produce all scale and complexities needed to produce synthetic tissue (Mandrycky et al., 2016). Commonly adopted 3D bioprinting techniques include extrusion-based, inkjet, laser-assisted and lithography-based bioprinting (Jia et al., 2023; Schwab et al., 2020). Extrusion-based bioprinting will be introduced in the following chapter since it is the bioprinting approach used in the experimental part of this thesis. After this, in Chapter 5.2, the other commonly adopted 3D bioprinting approaches will be briefly introduced.

5.1 Extrusion-based bioprinting

Most commercially available bioprinters are based on extrusion-based bioprinting (Mandrycky et al., 2016). In extrusion-based bioprinting, a continuous filament is extruded through a nozzle or needle and deposited onto a building platform layer-by-layer based

on the pre-designed 3D model. Once the bioink filament exits the nozzle it should retain its shape without deformation. Therefore, precrosslinking strategies can be used to improve stable filament extrusion, and/or crosslinking induced after printing can be performed to stabilize the extruded filament. (Schwab et al., 2020) Different crosslinking strategies used in 3D bioprinting are discussed further in Chapter 6.2.

Extrusion-based 3D bioprinters can have pneumatic, piston- or screw-driven dispensing systems (Figure 3) (Schwab et al., 2020). In pneumatic dispensing systems, the driving force required to extrude the filament is provided by air pressure. Instead, in piston-driven systems vertical mechanical force and in screw-driven dispensing systems rotational mechanical forces are used to extrude the filament. (Derakhshanfar et al., 2018) Screw-driven dispensing systems are used for highly viscous materials whereas pneumatic pressure and piston-based systems are typically used for materials with lower viscosities ($<10^7$ mPa·s) (Schwab et al., 2020).

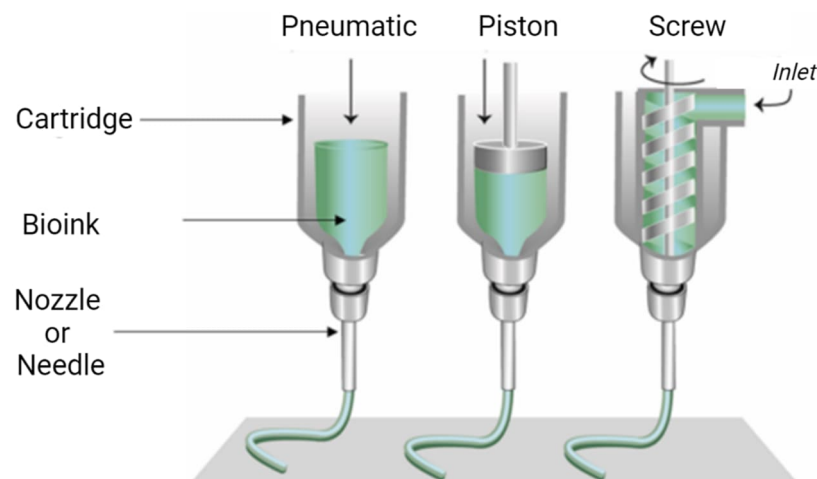


Figure 3. Different dispensing systems in extrusion-based bioprinting. Pneumatic, piston- or screw-driven dispensing systems can be used to extrude a filament through a nozzle or needle from the bioink which is stored in a cartridge. Modified from Schwab et al. (2020).

Indeed, an advantage of extrusion-based bioprinting is that it is suitable for printing bioinks with varying viscosities (Mandrycky et al., 2016). Other advantages of extrusion-based bioprinting include that bioprinters are often affordable, easy to use, fast prototyping can be performed, and a wide range of printable biomaterials are available (Derakhshanfar et al., 2018; Kong and Wang, 2023). Importantly, another advantage of extrusion-based bioprinting is that bioinks with high cell densities can be printed. However, shear stress and mechanical forces in the nozzle during extrusion of the bioink result in cell viability of 40 – 80% in the final structure. (Mandrycky et al., 2016) Moreover, extrusion-based bioprinting is slow, and since extrusion-based bioprinting uses filaments as

the building blocks of the structure, the creation of more complex shapes is hard (Li et al., 2023; Schwab et al., 2020). This is because the feasible printing resolution is mostly determined by the bioink and nozzle diameter even though extrusion-based bioprinters are available with accurate tool heads with 5 – 100 μm accuracy in the x-y-z planes. With cell containing bioinks, the printing resolution is also affected by the embedded cells since shear stress acting on cells in the nozzle during extrusion restricts the diameter of the nozzle that can be used as a smaller nozzle diameter creates higher shear stress. (Schwab et al., 2020) Therefore, the resolution of cell containing bioinks is typically limited to 100 μm (Li et al., 2023; Schwab et al., 2020). To prevent unnecessary shear stresses affecting cell viability and to ease extrusion, bioinks with shear-thinning properties are often selected since the viscosity of these materials decreases as shear rate increases during extrusion (Schwab et al., 2020).

A new area of research in extrusion-based 3D bioprinting is coaxial bioprinting (Kong and Wang, 2023). In coaxial bioprinting, a two-layered nozzle is used allowing the co-extrusion of two different solutions, a crosslinker and bioink, to create either bulk or hollow fibers (Costantini et al., 2018; Kong and Wang, 2023; Shyam Mohan et al., 2022). Thus, it is suitable for continuous fabrication of tubular structures and has been utilized especially in 3D bioprinting of vascularized tissues to obtain small-diameter blood vessels (Kong and Wang, 2023). Another adaptation, of extrusion-based bioprinting is printing into coagulation or support baths instead of directly onto a substrate. When bioprinting into coagulation baths, the liquid in the bath triggers the gelation of the extruded bioink (Costantini et al., 2018). Instead, when bioprinting into support baths, the bath gives structural support to the printed 3D structure, and this approach is often referred to as the Freeform Reversible Embedding of Suspended Hydrogels (FRESH) -method (Costantini et al., 2018; Hinton et al., 2015). The FRESH -method has been utilized in 3D bioprinting of the cornea to maintain the curved shape of the bioprinted structure (Isaacson et al., 2018).

In 3D bioprinting of the cornea, extrusion-based bioprinting is the most frequently used 3D bioprinting approach (Boix-Lemonche et al., 2023; Isaacson et al., 2018; Kilic Bektas and Hasirci, 2020; Kim et al., 2019a, 2019b, 2018; Kutlehria et al., 2020; Mörö et al., 2022; Peng et al., 2022; Song et al., 2022; Wu et al., 2016; Zhang et al., 2019a). Therefore, it is important to consider that structures created by extrusion-based bioprinting may have prominent strip-like patterns since the structures are composed of filaments. This is undesirable in applications that aim to create transparent constructs such as corneal tissue where these patterns could lead to opacities. (Jia et al., 2023) 3D bioprinting of the cornea is reviewed in detail in Chapter 7.

5.2 Other 3D bioprinting approaches

In addition to extrusion-based bioprinting, other major 3D bioprinting techniques include inkjet, laser-assisted and lithography-based bioprinting. Next, these techniques are briefly introduced.

Inkjet bioprinting was the first 3D bioprinting technique developed and is based on the inkjet printer ejecting controlled-size bioink droplets which are sequentially deposited onto a substrate to build up tissue-like constructs (Mandrycky et al., 2016). Inkjet bioprinting is classified into continuous inkjet and drop-on-demand (DoD) bioprinting. Continuous inkjet bioprinting ejects a continuous stream of bioink droplets whereas DoD bioprinting ejects droplets only on demand. Of the two, DoD bioprinting is preferred since droplets and their positioning can be more precisely controlled. (Vijayavenkataraman et al., 2018) In DoD bioprinting, the bioink droplets are generated by a thermal or piezoelectric actuator from the bioink that is stored in an ink cartridge (Figure 4A). Advantages of inkjet bioprinting include relatively high cell viability, high printing speed due to the possibility of multiple print heads working at the same time and low cost because of the similarity of the structure of the inkjet printer to commercial printers. Instead, disadvantages of inkjet bioprinting include, that it cannot be used for high viscosity materials (>15 mPa·s) and cell density of the bioink should be low ($<1 \times 10^6$ cells/ml) to keep the viscosity of the bioink low and to prevent clogging of the print head. (Mandrycky et al., 2016) Also, as inkjet printing uses bioink droplets to create the structure, the application possibilities of this bioprinting technique are limited (Derakhshanfar et al., 2018). Additionally, there is a risk of causing ultrasonic or thermal damage to the cells with the piezoelectric or thermal dispense mechanism (Kong and Wang, 2023). In corneal 3D bioprinting, DoD bioprinting has been utilized to create corneal stromal structures with a curved dome-like shape (Duarte Campos et al., 2019).

Laser-assisted bioprinting (LaBP) is based on a donor layer that responds to laser stimulation. The donor layer is composed of an energy-absorbing layer that responds to the laser stimulation and of bioink below the energy-absorbing layer. During LaBP a laser pulse is focused on the energy-absorbing layer which causes the layer to vaporize and form a high-pressure bubble that pushes the bioink to fall as a droplet onto the substrate (Figure 4B). (Mandrycky et al., 2016) Advantages of LaBP include high resolution, high cell viability in printed constructs since no shear stress is applied to the cells during printing, the ability to print highly viscous materials, and that the technique is a nozzle-free approach eliminating clogging in the print head (Kong and Wang, 2023; Mandrycky et al., 2016). In contrast, disadvantages of LaBP include high cost, the lack of understanding about the side effects of laser exposure on the cells, and the use of metals in the

energy-absorbing layer which may lead to metallic nanoparticle-induced cytotoxicity (Mandrycky et al., 2016; Vijayavenkataraman et al., 2018). LaBP has been utilized for bioprinting corneal structures including stromal and epithelial structures as well as structures with both stroma and epithelium (Sorkio et al., 2018).

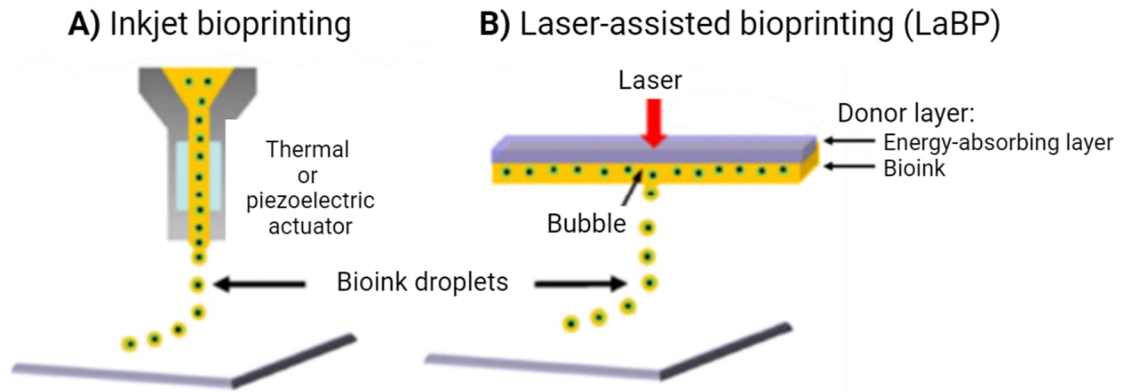
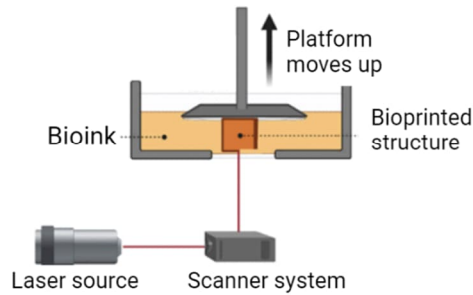


Figure 4. Illustrations of inkjet bioprinting (A) and LaBP (B) in which 3D bioprinting is based on the deposition of droplets. Modified from Mandrycky et al. (2016).

Lithography-based bioprinting utilizes light to selectively crosslink a photosensitive bioink in a reservoir or vat to create the 3D object (Li et al., 2023; Schwab et al., 2020). Different lithography-based bioprinting techniques exist and are categorized based on the exact mechanism of irradiation of the bioink. Examples of lithography-based bioprinting techniques include stereolithography (SLA) and dynamic light processing (DLP). (Schwab et al., 2020) In both SLA and DLP, the 3D object is created layer-by-layer. In SLA, a moving laser beam scans a layer of bioink in the printing position of the vat curing the photosensitive bioink point-by-point (Figure 5A). (Li et al., 2023) Instead, in DLP the curing is done plane-by-plane by projecting a 2D pattern of light to the layer of bioink using a digital mirror device (DMD) or a liquid crystal display (LCD) projection system (Figure 5B) (Li et al., 2023; Schwab et al., 2020). Therefore, DLP is faster than SLA as the whole layer of bioink can be cured in one individual light exposure. In both techniques, after the layer has been bioprinted, the build platform is moved up (bottom-up approach) or down (top-down approach) in z-direction to allow new bioink to flow to the printing position so that the next layer can be cured by the laser. (Li et al., 2023) Advantages of lithography-based bioprinting techniques include high resolution of down to 10 μm , fast fabrication speeds, and that the technique is a nozzle-free approach (Li et al., 2023; Schwab et al., 2020). A disadvantage of lithography-based bioprinting is that it requires photosensitive bioinks often needing ultra-violet (UV) light for polymerization which can be harmful to cells (Derakhshanfar et al., 2018; Knowlton et al., 2017; Lim et al., 2020). Additionally,

despite the high resolution, curved surfaces often appear as steps or terraces and therefore the resolution is still not ideal for creating curved constructs such as the cornea (Jia et al., 2023).

A) Stereolithography (SLA)



B) Dynamic light processing (DLP)

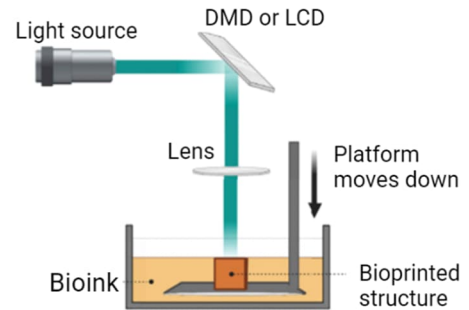


Figure 5. Illustrations of lithography-based bioprinting approaches. As examples, SLA with bottom-up approach (A) and DLP with top-down approach (B). Modified from Li et al. (2023).

6. BIOINKS

Groll et al. (2018) have defined bioinks as “a formulation of cells suitable for processing by an automated biofabrication technology that may also contain biologically active components and biomaterials”. Therefore, bioinks are 3D bioprintable formulations where cells are a mandatory component of the bioink. Additionally, the bioink may include biomaterials and biologically active components such as growth factors and cytokines, however, these are not mandatory components. Instead, biomaterials which are used for printing and are seeded with cells post-fabrication, are referred to as biomaterial inks. (Groll et al., 2018)

There are various requirements for a bioink, such as requirements based on the 3D bioprinting approach. For example, in extrusion-based bioprinting, individual cells and/or cell aggregates respond negatively to the shear stress during bioprinting reducing cell viability (Cui et al., 2020). Furthermore, as SLA and DLP are based on photopolymerization, the bioinks used in these approaches must have a photocrosslinkable component (Li et al., 2023). Therefore, biomaterials are also often incorporated into the bioink, and for this one of the most common choices is hydrogels. For example, in extrusion-based bioprinting, the hydrogel functions as a cell delivery vehicle protecting cells during bioprinting. (Cui et al., 2020) Hydrogels used in bioinks will be discussed further in Chapter 6.1 along with their crosslinking mechanisms (Chapter 6.2).

Karvinen and Kellomäki (2023) have defined that an ideal bioink should be “printable and easily manipulated by the printer, have controllable chemical, physical, functional, material and biological properties, have suitable viscosity and rheological properties, contain sterile and endotoxin free starting materials, be stable during printing procedure, enable homogeneous distribution of cells, and consider manufacture impact on cell viability”. Therefore, bioinks have requirements from both the 3D bioprinting approach itself as well as the cells which are embedded in the bioink. Consequently, one of the major challenges associated with 3D bioprinting is the development of bioink formulations that both meet the physicochemical requirements of the 3D bioprinting approach as well as the biological requirements of cells (Schwab et al., 2020). To underline this, the concept of “biofabrication window” has been introduced which describes the relationship between biocompatibility and shape fidelity of a bioink (Karvinen and Kellomäki, 2023; Schwab et al., 2020). In this context, shape fidelity describes how well the bioprinted structure matches the original 3D model (Karvinen and Kellomäki, 2023). Traditionally, bioinks

with good shape fidelity are stiff due to high polymer concentration and crosslinking density. However, the biological performance of cells, such as cell proliferation, migration, and differentiation, are reduced. Nevertheless, novel approaches have been developed where structures with high shape fidelity can be printed with low stiffness materials. (Schwab et al., 2020) Due to the multiple requirements set for bioinks, it is important to characterize bioinks. The characterization of bioinks is discussed in Chapter 6.3.

6.1 Hydrogels

Hydrogels are 3D hydrophilic polymer networks that can hold substantial amounts of water or biological fluids (Mantha et al., 2019). Hydrogels are used for 3D bioprinting and TE in general, since they mimic natural ECM components and allow cell encapsulation in a highly hydrated as well as mechanically supportive 3D environment (Dell et al., 2022). Moreover, the high-water content of hydrogels, helps the diffusion of nutrients in the structure (Mantha et al., 2019) and hydrogels can be modified to improve their biocompatibility, cellular adhesion, mechanical and shear-thinning properties (Dell et al., 2022). Therefore, hydrogels are the most used biomaterials in 3D bioprinting (Mancha Sánchez et al., 2020).

Hydrogels used in 3D bioprinting can be divided into synthetic polymer-based, natural polymer-based, and modified natural polymer-based hydrogels (Fang et al., 2023). The advantages of synthetic polymers include easy industrial production and ease of chemical modification (Dell et al., 2022). Instead, natural polymers are derived from natural sources and have better biological properties than synthetic polymers, including improved biocompatibility, biodegradability, cell affinity, and low toxicity (Dell et al., 2022; Fang et al., 2023). However, natural polymer-based hydrogels often have poor mechanical properties and therefore natural polymers have been functionalized to create modified natural polymer-based hydrogels. These hydrogels have improved mechanical properties and reduced sensitivity to environmental conditions while still maintaining the excellent biocompatibility of natural hydrogels. (Chimene et al., 2020; Fang et al., 2023) Next, commonly used natural and modified natural polymer-based hydrogels for bioinks will be introduced focusing on hydrogels which have been used for corneal applications.

Alginate is an unbranched natural anionic polysaccharide derived from brown seaweeds and is physically crosslinked with divalent cations such as calcium to form hydrogels (Hu et al., 2021). Alginate is used in 3D bioprinting due to having high biocompatibility, being inexpensive, nonimmunogenic and biodegradable (Balters and Reichl, 2023). However, it degrades slowly, suffers from poor printability, and has inadequate support for cell proliferation. Additionally, a major drawback of alginate is the lack of cell binding motifs in

alginate leading to poor cellular adhesion. Therefore, alginate is often combined with other biomaterials such as collagen. (Balters and Reichl, 2023; Dell et al., 2022) In these bioinks alginate usually acts as a structural stabilizer and thickening agent (Dell et al., 2022).

Collagen-based hydrogels for bioinks are mainly formed from type I (Col I) (Stepanovska et al., 2021). Col I is the main component in the connective tissues of mammals and is the most abundant protein in the ECM of corneas (Balters and Reichl, 2023; Stepanovska et al., 2021). Collagen is often used in bioinks due to exhibiting low immunological reactions and increasing cell growth, adhesion and attachment due to having cell binding motifs its structure. However, collagen has a slow gelation time, up to 30 minutes at 37 °C, and has low mechanical strength. (Balters and Reichl, 2023) Therefore, collagen can be combined with other biomaterials as done with corneal bioinks where gelatin and alginate were combined with collagen (Balters and Reichl, 2023; Kutlehria et al., 2020; Wu et al., 2016). Moreover, to increase mechanical strength, collagen can be chemically modified with methacrylate (Balters and Reichl, 2023; Isaacson et al., 2018). Chemical modification of natural polymers with methacrylate allows photocrosslinking of the polymers which leads to the formation of covalent bonds which can improve mechanical properties of the structure (Muir and Burdick, 2021). Crosslinking generally, as well as photocrosslinking will be discussed in more detail in the next chapter.

Gelatin is produced as a result of partial hydrolysis of collagen and thus gelatin has similar properties as collagen. These include biocompatibility, transparency and the presence of cell binding motifs which improve cell attachment. As an advantage over collagen, gelatin is more soluble, has reduced antigenicity and gellates more easily. However, gelatin needs to be cooled to reach a gel state which can negatively affect cell viability, and, like collagen, gelatin lacks mechanical stability. Therefore, gelatin is also combined with other biomaterials or chemically modified. (Balters and Reichl, 2023) Chemical modification of gelatin with methacrylate produces gelatin methacrylate (GelMA) which has been widely used in bioprinting due to easy synthesis with low cost, photocrosslinkability and biocompatibility (Rajabi et al., 2021). GelMA can be combined with other biomaterials to further increase mechanical properties (Balters and Reichl, 2023). For example, He et al. (2022) combined GelMA and poly(ethylene glycol) diacrylate (PEGDA) to increase the toughness of bioprinted corneal structures.

HA is an unbranched polysaccharide, naturally found in the ECM of various tissues and one of the most commonly used biomaterials for bioinks (Balters and Reichl, 2023; Dell et al., 2022). This is because HA is biocompatible, biodegradable, hydrophilic, supports cell signaling, wound repair, matrix organization and has anti-inflammatory effects (Dell

et al., 2022; Ding et al., 2023). Nevertheless, due to poor mechanical strength and a fast degradation rate, HA is not suitable alone for 3D bioprinting (Ding et al., 2023). Therefore, HA is often chemically modified with functional groups to limit its degradation and increase stability in bioinks (Dell et al., 2022). Various modifications can be made. For example, to make photocrosslinkable bioinks HA can be modified with methacrylate, acrylate and tyramine groups (Sekar et al., 2023). As another example, HA can be functionalized with hydrazide and aldehyde groups to create HA-based bioinks via hydrazone crosslinking (Mörö et al., 2022; Sekar et al., 2023). Under normal conditions, HA is not found in the ECM of the cornea (Balters and Reichl, 2023) but has still been utilized in corneal bioinks (Mörö et al., 2022; Sorkio et al., 2018).

Decellularized ECM extracted from different tissues or organs has also been used for bioinks (Khoshnood and Zamanian, 2020). The advantage of decellularized ECM bioinks is that the bioink contains a wide range of ECM components and thus resembles more closely the native tissue providing high cellular survival and functionality (Khoshnood and Zamanian, 2020; Mandrycky et al., 2016). However, decellularized ECM bioinks have poor mechanical properties and extraction of ECM from a specific tissue or organ is extremely expensive and labor intensive compared to polymer-based bioinks (Khoshnood and Zamanian, 2020). An alternative approach to obtain decellularized ECM for bioinks is cell-derived ECM which can be obtained by culturing cells that synthesize, secrete, and assemble ECM components around them. Once enough ECM has been deposited, the cells can be removed through decellularization. Thus, cell-derived ECM is more easily obtained and can be scaled up through the culture of cells in bioreactors. (Dzobo et al., 2019)

Finally, it is important to emphasize that bioinks containing only one type of hydrogel as biomaterial component in the bioink normally either sacrifice biocompatibility or shape fidelity needed for successful extrusion-based bioprinting. Therefore, the introduction of one or more components into a bioink can improve the biofunctionality or enhance the mechanical stability to maintain shape fidelity of the bioink. Often these types of multi-component bioinks involve more than one type of crosslinking mechanism and therefore understanding the crosslinking chemistry of the components is important. (Cui et al., 2020) Next, crosslinking mechanisms used are discussed.

6.2 Crosslinking

To be able to maintain shape fidelity of printed constructs, crosslinking of the hydrogel in the bioink is essential. Incomplete crosslinking of the hydrogel can lead to the collapse of the printed construct. (Cui et al., 2020) Therefore, crosslinking affects the stability and

mechanical properties of the hydrogel (Zennifer et al., 2022). Additionally, the crosslinking process can affect cell viability and functionality, and therefore should be carefully designed (Cui et al., 2020). The crosslinking approach used depends on the polymer backbone, functional side groups of the polymer and their crosslinking mechanism (Zennifer et al., 2022). Crosslinking of hydrogels can be broadly divided into physical or chemical crosslinking (Cui et al., 2020; Zennifer et al., 2022).

Physical crosslinking is a result of noncovalent interactions between polymer chains. These interactions include hydrophobic interactions, electrostatic interactions, hydrogen bonds and stereocomplexation. As the noncovalent interactions are reversible and are influenced by the environment, e.g., temperature, pH and ions present, solely physically crosslinked hydrogels have poor mechanical stability when compared to chemically crosslinked hydrogels. Nevertheless, hydrogels crosslinked using physical crosslinking have shear-thinning behavior and reversibility of bond formation under applied pressure, thus being attractive for extrusion-based bioprinting. (Cui et al., 2020) As an example, alginate hydrogels are physically crosslinked using divalent cations, such as calcium, which bind to guluronic residues in adjacent alginate chains via electrostatic interactions between opposite charges (Cui et al., 2020; Hu et al., 2021; Wan et al., 2008).

Chemical crosslinking is a result of covalent bonding of chemically reactive functional groups. Reaction mechanisms for the covalent bonding include free radical polymerization, click chemistry, thiol-ene chemistry, Schiff's-base reactions and enzymatic crosslinking reactions. (Cui et al., 2020) A form of chemical crosslinking is photocrosslinking, which includes reaction mechanisms that are based on the absorption of light energy to initiate chemical reactions leading to the formation of covalent bonds between the reactive functional groups (Zennifer et al., 2022). Next, the chemical crosslinking approaches, photocrosslinking and click chemistry, are introduced in more detail as they are the main crosslinking approaches utilized in the bioinks of this thesis.

6.2.1 Photocrosslinking

Photocrosslinking is one of the most commonly used crosslinking approaches in 3D bioprinting since it enables the spatiotemporal control of crosslinking reactions with light (Zennifer et al., 2022). Light is considered a good external control method to manipulate the properties of hydrogels since the exposed area, light intensity and wavelength can be chosen and also duration of exposure can be easily controlled by simply turning the light on and off (Choi et al., 2019; Zennifer et al., 2022). Photocrosslinkable bioinks contain photoinitiators and pre-polymers in addition to cells (Choi et al., 2019). Photoinitiators are molecules that upon exposure to UV or visible light produce reactive species

that trigger a polymerization process where the pre-polymers are polymerized, i.e. cross-linked (Choi et al., 2019; Schwab et al., 2020). Two common photoinitiators used in 3D bioprinting are Irgacure 2959 and lithium phenyl-2,4,6-trimethylbenzoylphosphinate (LAP) (Lim et al., 2020). Photocrosslinking of bioinks in extrusion-based bioprinting is performed after the deposition of each layer or after printing the entire structure (Schwab et al., 2020).

Photocrosslinking reaction mechanisms used in bioprinting include free radical polymerization, thiol-ene photocrosslinking, and photomediated redox crosslinking (Choi et al., 2019; Lim et al., 2020; Zennifer et al., 2022). From these, free radical polymerization is currently the most common reaction mechanism utilized to fabricate chemically cross-linked hydrogels (Cui et al., 2020; Zennifer et al., 2022). Therefore, free radical polymerization is explained next in more detail.

Free radical polymerization, or chain-growth polymerization is generally composed of three different stages which are initiation, propagation, and termination (Zennifer et al., 2022). In the first step, initiation, light exposure causes light-induced cleavage of the photoinitiator creating free radicals. The generated free radicals react with specific functional groups of the pre-polymer, such as methacrylate and acrylate, forming new covalent bonds and reactive radical intermediates. Next, in propagation, these reactive radical intermediates react with subsequent functional groups leading to chain growth. (Lim et al., 2020) Finally, in termination, the propagation is ended with one of the following mechanisms: 1) radical coupling where two chain ends are combined to form one continuous chain, 2) disproportionation where two chain ends terminate to form a chain with a saturated terminal group and a chain with a nonsaturated terminal group, or 3) by using a chain transfer agent to transfer the radical intermediate away from the propagating chain (Lim et al., 2020; Zennifer et al., 2022). This mechanism of free radical polymerization is presented in Figure 6A. Photocrosslinkable hydrogels GelMA and HAMA, which have been extensively explored in the biomedical field and utilized in bioinks, are generally photocrosslinked using free radical polymerization of methacrylate groups (Choi et al., 2019; Lim et al., 2020). HAMA is the photocrosslinkable polymer used for the bioink of this thesis, and the free radical polymerization of HAMA is illustrated in Figure 6B.

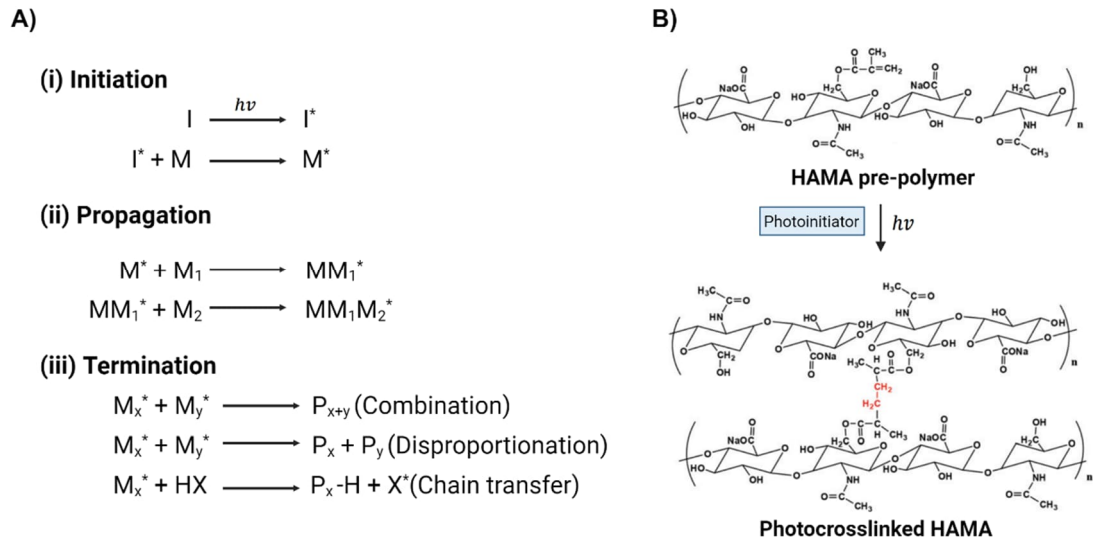


Figure 6. Mechanism of free radical polymerization (A) and free radical polymerization of HAMA (B). Modified from Zennifer et al. (2022) and Zhou et al. (2016). Created with BioRender.com.

Important considerations for photocrosslinking include assessing the effect of light on cells and crosslinking efficiency in the bioink (Knowlton et al., 2017). These depend on the chosen photoinitiator, its concentration, light intensity, exposure time and wavelength as well as the degree of reactive functional groups in polymers (Lim et al., 2020; Zennifer et al., 2022).

The absorption peak of the chosen photoinitiator determines the wavelength of light that must be applied to the bioink for successful crosslinking (Knowlton et al., 2017). However, the wavelength has an impact on cell viability as shorter wavelengths decrease cell viability (Knowlton et al., 2017; Zennifer et al., 2022). Wavelengths in the UV range of 320 – 400 nm can damage the nuclear DNA of cells which may contribute to genomic mutations and carcinogenesis in the cell. However, even more damaging are wavelengths in the UV range of 290 – 320 nm which can induce apoptosis. (Knowlton et al., 2017) Therefore, the use of visible light (400 – 700 nm) for photocrosslinking of bioinks has been researched (Knowlton et al., 2017; Zennifer et al., 2022). If UV light is used, a wavelength of 365 nm is often chosen to minimize genotoxicity and cytotoxicity, since it is closer to the visible light range (Lim et al., 2020). Also, a longer exposure time, increased photoinitiator concentration and light intensity reduce the viability of the cells in the bioprinted structure (Lim et al., 2020; Zennifer et al., 2022). In these cases it has been suggested that the radicals generated from the cleavage of the photoinitiator would be responsible for the reported cytotoxicity. Bioinks can be photocrosslinked generally with UV light if the total light dosage is minimized. Nevertheless, as the cytotoxic impact

of radicals can significantly affect cell behavior, it is important to wash bioprinted structures containing cells after light exposure whenever possible to remove any potentially harmful radicals. (Lim et al., 2020)

Regarding mechanical properties, polymer crosslink density can be tuned in free-radical polymerization by changing photoinitiator concentration, light intensity, and the degree of reactive functional groups in polymers. In general, a higher degree of crosslinking within polymer networks leads to improved mechanical properties. (Lim et al., 2020) In addition to cell viability, the wavelength of the light affects the optical penetration depth in the bioprinted structure. UV light has decreased optical penetration depth when compared to visible light, which can result in poorly crosslinked areas in interior regions of the bioprinted structures. (Zennifer et al., 2022)

6.2.2 Click chemistry

Click chemistry based hydrogels are formed spontaneously upon mixing two or more reactive compounds (Mueller et al., 2022). The major advantage of click chemistry is that the reaction is bio-orthogonal meaning the reaction can happen in a biological environment without having an effect on biomolecules or interfering with biochemical processes (Bird et al., 2021; Jiang et al., 2014). Therefore, click-chemistry can be used to encapsulate cells in bioinks since the reaction does not interfere with the cells. Other advantages of click chemistry include high reactivity, superb selectivity, mild reaction conditions (Jiang et al., 2014), and the possibility to adjust gelation and degradation rate with the choice of reactive components (Mueller et al., 2022).

There are various click reactions, the most common being the copper(I)-catalyzed azide-alkyne click reaction (Cui et al., 2020; Jiang et al., 2014). This click reaction is bio-orthogonal, but the copper catalyst is potentially cytotoxic (Jiang et al., 2014), and therefore limits its use in 3D bioprinting. Instead, hydrazone crosslinking, where aldehyde and hydrazide groups react to form a hydrazone bond (Koivusalo et al., 2019; Nie et al., 2023) has shown great potential for bioink crosslinking (Mörö et al., 2022). The reaction has no toxic reagents or side products in addition to having high reactivity and simple reaction conditions (Jiang et al., 2014; Koivusalo et al., 2019). Hydrazone crosslinking belongs to the group of pseudo-click reactions, meaning that the reaction has moderate orthogonality (Jiang et al., 2014; Koivusalo et al., 2019). Hydrazone crosslinked HA has been used in bioinks for extrusion-based bioprinting (Mörö et al., 2022; Wang et al., 2018). Additionally, hydrazone crosslinking has been utilized for injectable gellan gum-hyaluronan-hydrogels (Karvinen et al., 2017).

6.3 Characterization of Bioinks

Bioink characterization is needed for studying the multiple requirements set for bioinks including printability, cytocompatibility, suitable mechanical properties, suitable degradation kinetics and safe degradation byproducts (Karvinen and Kellomäki, 2023). Next, some key aspects that need to be considered in pre- and post-printing characterization will be introduced for extrusion-based bioprinting (Figure 7).

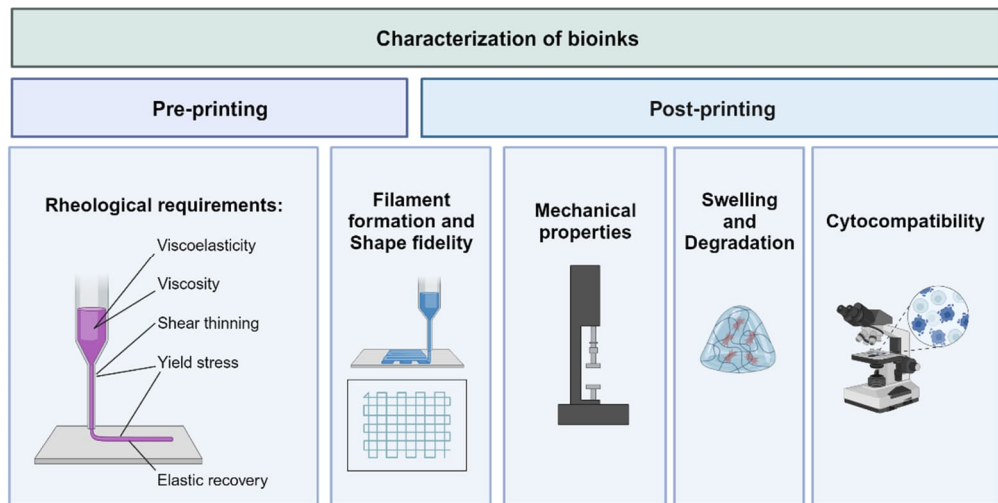


Figure 7. Key aspects to be considered in bioink characterization (Deo et al., 2020; Karvinen and Kellomäki, 2023; Schwab et al., 2020). Created with BioRender.com.

In extrusion-based bioprinting, printability generally refers to suitable extrudability, filament formation and shape fidelity (Karvinen and Kellomäki, 2023; Schwab et al., 2020). The printability of bioinks mainly depends on their rheological properties and thus the rheological properties during extrusion, recovery and self-supporting stages should be characterized for successful 3D bioprinting (Ding et al., 2023). Pre-printing characterization of printability consists of assessing the key rheological properties of the bioink including viscosity, shear-thinning properties, viscoelasticity, yield stress, and elastic recovery to predict extrudability, filament formation and shape fidelity (Schwab et al., 2020).

Viscosity of bioinks is characterized pre-printing as viscosity along with nozzle diameter and printing pressure influences the shear stress acting on cells in the nozzle during extrusion. Viscosity describes how much fluid resists flow under a stress, and in 3D bioprinting viscosity characterizes the ability of the bioink to flow through the nozzle onto the printing surface. High viscosity bioinks have reduced flow ensuring that the printed structure holds its shape better after printing. However, high viscosity bioinks require higher pressure to flow leading to increased shear stresses which are harmful for cells. In hydrogel-based bioinks, viscosity depends on the concentration, molecular weight,

and degree of branching of the polymer as well as addition of rheological modifiers and temperature. Bioinks with high viscosity can be obtained by increasing the concentration, molecular weight, and degree of branching of the polymer. (Karvinen and Kellomäki, 2023)

An important concept related to viscosity is shear-thinning. With a shear-thinning material, viscosity decreases when shear rate increases (Karvinen and Kellomäki, 2023). This is especially important for extrusion-based bioprinting since shear-thinning characteristics of a bioink allow the bioink to flow through the nozzle due to the decrease in viscosity as shear rate increases during extrusion and, once exiting the nozzle, allows the bioink to immediately recover and solidify to provide shape fidelity since as the shear rate drops viscosity increases after extrusion (Cui et al., 2020; Karvinen and Kellomäki, 2023; Schwab et al., 2020). Shear rate sweeps can be used to study the viscosity of bioinks and to determine whether the bioink is shear-thinning (Karvinen and Kellomäki, 2023). To mimic bioinks going through a needle, shear rate sweeps often use a range of shear rates from low to high (Deo et al., 2020; Karvinen and Kellomäki, 2023).

Bioinks used for extrusion-based bioprinting need to have flow properties during extrusion of the bioink through the nozzle as well as elastic shape retention properties after exiting the nozzle. This combination of viscous flow and elastic shape retention is called viscoelasticity and is described using the storage and loss modulus. (Schwab et al., 2020) The storage modulus depicts the amount of energy elastically stored within the bioink during deformation and therefore related to the elastic shape retention whereas the loss modulus depicts the amount of energy dissipated by the bioink and therefore associated with viscous flow (Deo et al., 2020; Schwab et al., 2020). Viscoelasticity protects cells from shear stress during extrusion and an inadequate storage modulus can lead to the collapse of printed structures (Karvinen and Kellomäki, 2023). Viscoelastic properties of bioinks can be determined with oscillatory rheology. Based on the ratio between the loss and storage modulus, the damping factor ($\tan(\delta)$) can be utilized to identify a suitable balance between flow and shape retention. (Karvinen and Kellomäki, 2023; Schwab et al., 2020)

In addition to the storage modulus, shape retention of the bioink can be characterized by studying yield stress (Schwab et al., 2020). Yield stress is the minimum stress that has to be applied on the material for it to flow. If a stress above this is applied, polymer network interactions are interrupted allowing the material to flow. (Deo et al., 2020) Therefore, yield stress depicts the force needed to start bioink extrusion (Karvinen and Kellomäki, 2023). Additionally, increased yield stress mostly improves filament formation and stiffness of the printed structure (Schwab et al., 2020). Rheology can be used to

study yield stress for example by determining shear stress at the crossover point of storage and loss modulus in oscillatory measurements (Karvinen and Kellomäki, 2023). Finally, elastic recovery, the time dependent response of the bioink after shear induced deformation, can also be studied by performing recovery tests to analyze the ability of the bioink to restore its elastic properties when exposed to alternating high and low shear stress (Schwab et al., 2020).

When a continuous filament can be extruded, post-printing characterization can be done. This includes the evaluation of shape fidelity of printed filaments and structures (Schwab et al., 2020). High shape fidelity of the bioprinted constructs should be maintained over the desired time period, for example over the period needed for cell culture. Shape fidelity of printed structures can be characterized in several ways. Quantitatively shape fidelity can be evaluated post-printing for example by assessing the homogeneity of single filaments by measuring fiber diameter in different parts of the extruded filament and comparing the measured values. (Karvinen and Kellomäki, 2023) Another way to evaluate shape fidelity is evaluating the shape of the pores in printed grid structures designed with square shape pores. By measuring the perimeter and area of the pore, the pore factor can be calculated with the following equation

$$Pore\ Factor = \frac{L^2}{16A}, \quad (1)$$

where L is the perimeter of the pore and A the pore area. The pore factor describes how close the printed pores are to a square shape. (Ouyang et al., 2016; Soltan et al., 2019) A perfectly square pore has a pore factor of 1, and thus matches the design exactly, has proper gelation as well as precise material deposition (Karvinen and Kellomäki, 2023; Soltan et al., 2019). Instead, a pore factor below 1 indicates a more circular shape of the pore and under gelation of the bioink (Soltan et al., 2019). In contrast, a pore factor over 1 indicates over gelation of the bioink and leads to poorly constructed pores with cracks and ridges (Karvinen and Kellomäki, 2023). According to Ouyang et al. (2016) the pore factor should be in the range of 0.9 – 1.1. Other approaches to analyze shape fidelity of printed structures include evaluating filament merging in the intersection of two filaments and analyzing the height of the structure in multilayered constructs (Schwab et al., 2020).

It is also important to characterize the mechanical properties of printed constructs (Karvinen and Kellomäki, 2023). Ultimately, it would be desirable that the mechanical properties of the printed structure would match the ones of native tissue to provide mechanical stability once implanted (Deo et al., 2020). In addition to suitable stiffness ensuring that the printed construct can support itself, stiffness influences cell behavior. The mechani-

cal properties of bioprinted structures can be characterized using compression and tensile tests to determine the ability of the bioink to withstand deformation. It is important to take into account that the mechanical properties of bioprinted structures may be different from casted hydrogels since bioprinted structures may contain voids and during bioprinting polymer chains may align. (Karvinen and Kellomäki, 2023)

Another important aspect to be characterized post-printing is the swelling and degradation of the bioprinted structures. Swelling occurs once the bioprinted structure is either cultured in cell culture media or implanted *in vivo*. (Karvinen and Kellomäki, 2023) The mechanical properties of the bioprinted structure can be influenced by the swelling since as the amount of fluid increases in the bioprinted structure the distance between crosslinks can increase leading to a decrease in the crosslinking density which affects the mechanical properties of the printed structure. Still, swelling can be also beneficial since it enables the diffusion of cellular waste products and possible entrapped therapeutics. (Deo et al., 2020; Karvinen and Kellomäki, 2023) Moreover, as bioprinted structures should remain stable both *in vitro* and *in vivo* to give support to cells until they have produced their own ECM, hydrogels with suitable degradation rates must be chosen (Karvinen and Kellomäki, 2023). The swelling behavior of hydrogels can be analyzed by calculating the swelling ratio during incubation (Jongprasitkul et al., 2022; Koivusalo et al., 2019). Similarly, swelling, and subsequent degradation can be analyzed by calculating the remaining weight percentage at each timepoint with the following equation

$$\text{Remaining weight \%} = \frac{\text{Measured weight}}{\text{Initial Weight}} \times 100, \quad (2)$$

(Mörö et al., 2022).

One of the most essential parts of bioink characterization is the evaluation of cytocompatibility of the bioink (Deo et al., 2020). Crosslinking density and molecular weight of polymers in the bioink are critical factors influencing cell behavior. As an example, lower crosslinking density allows nutrient and waste diffusion which aids cell proliferation, migration, and tissue formation. (Karvinen and Kellomäki, 2023) Also, it is important to understand the bioink-cell interactions to know how the cells can be stimulated by the bioink and how degradation byproducts effect the cells (Deo et al., 2020). Moreover, the effect of shear forces, printing pressure and polymer crosslinking agents on cells should be evaluated (Deo et al., 2020; Karvinen and Kellomäki, 2023). For this, different types of cytotoxicity/viability assays can be performed such as the Live/Dead assay. However, these methods usually concentrate on cell viability and do not consider other cellular processes such as differentiation and secretion of proteins. (Deo et al., 2020) Therefore, alongside cell viability, cell proliferation, differentiation and adhesion should be studied

(Karvinen and Kellomäki, 2023). For example, PrestoBlue™ analysis can be used to quantitatively measure the proliferation of cells, and immunofluorescence (IF) staining can be used to study differentiation, proliferation (e.g., proliferation marker Ki67), and adhesion (e.g., vinculin staining to monitor focal adhesion points) (Deo et al., 2020; Möro et al., 2022; PrestoBlue™, 2023; Sorkio et al., 2018).

7. 3D BIOPRINTING OF CORNEA

As discussed, 3D bioprinting can overcome limitations of conventional TE fabrication techniques by allowing the automated fabrication of complex 3D constructs with multiple cell types and biomaterials (Cui et al., 2020). Therefore, 3D bioprinting enables the creation of cornea mimicking structures with the several cell types, multiple layers, curved corneal geometry and mechanical properties of the cornea (Zhang et al., 2019b). Also, since corneal tissue is avascular, the major limitation of bioprinting, vascularization of the bioprinted constructs, is bypassed (Balters and Reichl, 2023). Moreover, as an immune-privileged tissue, rejection and inflammatory responses are less likely in the cornea than in other tissues (Fuest et al., 2020, p. 3). Thus, the corneal tissue is an attractive application area for 3D bioprinting, and bioprinted cornea mimicking structures have the potential to overcome the shortage of donor corneas (Balters and Reichl, 2023; Barrientez et al., 2019). The research conducted on 3D bioprinting of cornea to date is summarized in Table 1.

Table 1. Summary of research articles on 3D bioprinting of cornea

	3D bioprinting approach	Main bioink components	Cell type	Cell density (cell/ml)
Epithelial layer				
<i>Wu et al. 2016</i>	Extrusion	Rat Col I, Alginate, Gelatin	human corneal epithelial cells	1×10^6
<i>Zhong et al. 2021</i>	DLP	GelMA or Hyaluronic acid glycidyl methacrylate (HAGM)	rabbit LSCs or human LSCs	$10 - 20 \times 10^6$
Stromal layer				
<i>Isaacson et al. 2018</i>	Extrusion (FRESH)	Alginate, Methacrylated Col I	hCSKs	2×10^6
<i>Duarte Campos et al. 2019</i>	DoD bioprinting	Bovine Col I, Agarose	hCSKs	1×10^6
<i>Kim et al. 2019a</i>	Extrusion	Cornea-derived decellularized ECM	hTMSCs	5×10^6
<i>Mahdavi et al. 2020a</i>	SLA	GelMA	hCSCs	8×10^6
<i>Kilic Bektas and Hasirci 2020</i>	Extrusion	GelMA	hCSKs	1×10^6
<i>Kutlehria et al. 2020</i>	Extrusion	Alginate, Gelatin, Bovine Col I	hCSKs	3×10^6

<i>Song et al. 2022</i>	Extrusion	Bovine Col I	hCSCs	0.2x10 ⁶
<i>Mörö et al. 2022</i>	Extrusion	Col I, HA, HA-ALD and HA-CDH or HA-DA-CDH	hASCs or hASC-CSKs	1.1x10 ⁶
<i>Boix-Lemonche et al. 2023</i>	Extrusion	Nanocellulose, Alginate, Human Col I	hBM-MSCs, hCS-MSCs or hASCs	1.5x10 ⁶
<i>Zhang et al. 2023</i>	DLP	GelMA, Cornea-derived decellularized ECM	human corneal fibroblasts	0.1x10 ⁶
<i>Endothelial layer</i>				
<i>Kim et al. 2018</i>	Extrusion	Gelatin	human corneal endothelial cells	3x10 ⁶
<i>Epithelial and stromal layer</i>				
<i>Sorkio et al. 2018</i>	LaBP	<u>Epithelium:</u> LN521, HA <u>Stroma:</u> Human Col I with plasma and thrombin	<u>Epithelium:</u> hESC-LSC <u>Stroma:</u> hASCs	30x10 ⁶
<i>He et al. 2022</i>	DLP	GelMA, PEGDA	<u>Epithelium:</u> rabbit corneal epithelial cells <u>Stroma:</u> rabbit ASCs	1x10 ⁶
<i>Layer not specified</i>				
<i>Zhang et al. 2019a</i>	Extrusion	Alginate, Gelatin	human corneal epithelial cells	2x10 ⁶
<i>Kim et al. 2019b</i>	Extrusion	Cornea-derived decellularized ECM	hTMSCs	1x10 ⁶
<i>Peng et al. 2022</i>	Extrusion	Alginate, Gelatin	human corneal fibroblast	0.4x10 ⁶

Many different 3D bioprinting approaches have been used to 3D bioprint cornea mimicking structures (Table 1). The most common approach is extrusion-based-bioprinting which has been utilized for the epithelial (Wu et al., 2016), stromal (Boix-Lemonche et al., 2023; Isaacson et al., 2018; Kilic Bektas and Hasirci, 2020; Kim et al., 2019a; Kutlehria et al., 2020; Mörö et al., 2022; Song et al., 2022) and endothelial layer (Kim et al., 2018). The epithelial layer has also been bioprinted using DLP (He et al., 2022; Zhong et al., 2021) and LaBP (Sorkio et al., 2018) whereas stromal structures have been printed using DoD bioprinting (Duarte Campos et al., 2019), SLA (Mahdavi et al., 2020a), LaBP (Sorkio et al., 2018) and DLP (He et al., 2022; Zhang et al., 2023).

Various biomaterials have been used in bioinks for the 3D bioprinting of cornea mimicking structures. These biomaterials used in bioinks are mainly hydrogels since they provide a suitable environment for cells to thrive as discussed in Chapter 6.1. In most cases multiple biomaterials have been combined for the bioink to acquire the desired properties (Table 1). Col I is used as a component in many corneal bioinks (Boix-Lemonche et al., 2023; Duarte Campos et al., 2019; Kutlehria et al., 2020; Mörö et al., 2022; Song et al., 2022; Sorkio et al., 2018; Wu et al., 2016) as it is the major structural protein of the corneal stroma (España and Birk, 2020; Meek and Knupp, 2015) and due to its many advantages discussed in Chapter 6.1 including the presence of cell binding motifs (Balters and Reichl, 2023). Another common corneal bioink component is alginate (Boix-Lemonche et al., 2023; Isaacson et al., 2018; Kutlehria et al., 2020; Peng et al., 2022; Wu et al., 2016; Zhang et al., 2019a) due to being inexpensive, biocompatible and nonimmunogenic (Balters and Reichl, 2023). Also, gelatin has been widely used in corneal bioinks (Kim et al., 2018; Kutlehria et al., 2020; Peng et al., 2022; Wu et al., 2016; Zhang et al., 2019a) due to having similar properties as collagen but gelling more easily (Chapter 6.1) (Balters and Reichl, 2023). Moreover, the chemically modified form of gelatin, GelMA has been used (He et al., 2022; Kilic Bektas and Hasirci, 2020; Mahdavi et al., 2020a; Zhang et al., 2023; Zhong et al., 2021) since it can be easily photocrosslinked to increase mechanical stability (Balters and Reichl, 2023) and is required for SLA and DLP as these bioprinting approaches are based on photopolymerization (Li et al., 2023). Other biomaterials used as bioink components for corneal bioinks include methacrylated Col I (Isaacson et al., 2018), PEGDA (He et al., 2022), agarose (Duarte Campos et al., 2019), cornea-derived decellularized ECM (Kim et al., 2019a, 2019b; Zhang et al., 2023), nanocellulose (Boix-Lemonche et al., 2023), laminin (Sorkio et al., 2018) and HA (Mörö et al., 2022; Sorkio et al., 2018; Zhong et al., 2021).

As the cellular component for the bioink multiple different cell types have been used from both human and animal origin. For the epithelial layer human corneal epithelial cells (Wu et al., 2016), rabbit corneal epithelial cells (He et al., 2022), primary rabbit LSCs, primary human LSCs (Zhong et al., 2021) and human ESC -derived LSCs (hESC-LSCs) have been used. Most bioinks for the stromal layer have utilized either hCSKs (Duarte Campos et al., 2019; Isaacson et al., 2018; Kilic Bektas and Hasirci, 2020; Kutlehria et al., 2020) or hCSCs (Mahdavi et al., 2020a; Song et al., 2022). Also, human corneal fibroblasts have been used (Peng et al., 2022; Zhang et al., 2023). Stems cells used for the stromal layer are human bone marrow-derived MSCs (hBM-MSCs) (Boix-Lemonche et al., 2023), human corneal stroma-derived MSCs (hCS-MSCs) (Boix-Lemonche et al., 2023), hASCs (Boix-Lemonche et al., 2023; Mörö et al., 2022; Sorkio et al., 2018), hASC-CSKs

(Mörö et al., 2022), rabbit adipose tissue -derived stem cells (rabbit ASCs) (He et al., 2022) and human turbinate derived MSCs (hTMSCs) (Kim et al., 2019a, 2019b). For the endothelial layer, primary human corneal endothelial cells (Kim et al., 2018) have been used.

All studies published regarding 3D bioprinting of corneal structures (Table 1) have reported high cell viability after printing, but cell morphology differs between publications. In the stroma of the human cornea, hCSKs have dendritic cell morphology with long and branching cellular processes (Yam et al., 2020). Therefore, it would be important for hCSKs to have similar morphology in bioprinted stromal structures. Dendritic cell morphology of hCSKs (Duarte Campos et al., 2019), hASC-CSKs (Mörö et al., 2022), hCSCs (Song et al., 2022) as well as elongated morphology of hCSCs (Mahdavi et al., 2020a), hASCs (Mörö et al., 2022; Sorkio et al., 2018) and human corneal fibroblasts (Zhang et al., 2023) has been reported after bioprinting. However, some studies have reported rounded morphology of hCSKs (Kilic Bektas and Hasirci, 2020; Kutlehria et al., 2020). These studies attributed the rounded morphology to dense crosslinking and overall stiffness of the structures limiting the mobility of the cells and preventing cell interactions as well as elongation (Kilic Bektas and Hasirci, 2020; Kutlehria et al., 2020).

Symmetric curvature of the cornea is essential for optimal refractive power (Sridhar, 2018, p. 192). In addition, curved corneal geometry is known to influence hCSC migration and collagen alignment as well as to support the growth, stratification, and differentiation of human corneal epithelial cells *in vitro* (Gouveia et al., 2017; Isaacson et al., 2018). Therefore, several studies have attempted to recreate this curved corneal geometry. The curved dome-like structure has been created by printing concentric circles (Isaacson et al., 2018; Kutlehria et al., 2020; Zhang et al., 2019a), concentric annuluses (He et al., 2022; Mahdavi et al., 2020a) or a spiral (Song et al., 2022). Many studies have used external support structures as substrates to enable the printing of a curved dome-like cornea (Isaacson et al., 2018; Kutlehria et al., 2020; Song et al., 2022; Zhang et al., 2019a). Isaacson et al. (2018) used extrusion-based bioprinting and a concave support structure in combination with the FRESH -method to maintain the printed shape of corneal stromal structures. Also, Kutlehria et al. (2020) used a substrate with 6 concave wells to maintain the dimensions of the printed corneal stromal structures during extrusion-based bioprinting. Similarly, Song et al. (2022) used a concave substrate during extrusion-based bioprinting to print corneal stroma mimicking structures. Instead, Zhang et al. (2019a) used a convex support structure during extrusion-based bioprinting of cornea. Moreover, Mahdavi et al. (2020a) used SLA and a sacrificial layer of gelatin to create the curved geometry of the corneal stroma. After photocrosslinking of each layer,

uncrosslinked bioink was removed and the sacrificial gelatin was added into the hollow part of the structure (Mahdavi et al., 2020a). However, some studies have been published where no external support structures were needed to create the curved geometry. Duarte Campos et al. (2019) used DoD bioprinting to print corneal stromal structures and He et al. (2022) used DLP to print corneal structures with epithelium and stroma without the need for external support structures.

As discussed in Chapter 2.1, the cornea is composed of three cellular layers which are the epithelium, stroma, and endothelium. 3D bioprinting has been studied for fabricating all these layers, however, most studies focus on the fabrication of only one layer. A few studies have reported combining the epithelial and stromal layers (He et al., 2022; Sorkio et al., 2018). He et al. (2022) used DLP to print dome-shaped corneal structures with epithelial and stromal layers. Rabbit corneal epithelial cells were used for the epithelial layer whereas rabbit ASCs were used for the stromal layer. In both layers, blended GelMA and PEGDA were used as bioink components with LAP as photoinitiator. The 3D bioprinted corneal structure was assessed *in vivo* in a rabbit ALK model. During the implantation process, the corneal structure could be handled without collapse. Over the observation period of 28 days, the implanted corneal structure remained in place and transparent, and had no clear inflammation or neovascularization. Additionally, no visible scar was observed, and successful re-epithelialization and stromal regeneration occurred. Moreover, based on the gene expressions of the CSK specific markers, keratocan and ALDH 3A1, as well as lumican expression detected by IF staining, the rabbit ASCs of the stromal layer were able to differentiate into CSKs. (He et al., 2022) Instead, Sorkio et al. (2018) used a human recombinant laminin 521 (LN521) -based bioink containing hESC-LSCs for the epithelial layer and a human Col I -based bioink containing hASCs for the stromal layer. Using LaBP and a Matrigel™ absorption layer, 3D stromal structures were first printed from the hASC containing human Col I -based bioink following which multiple layers of hESC-LSC containing LN521 -based bioink was printed on top of the stromal structure. To prevent shrinkage during culture, non-transparent Matri-derm® supportive sheets had to be used. Without the supportive sheet, when printed on a transparent substrate, the 3D corneal structures had moderate transparency. Additionally, the hESC-LSCs formed a stratified epithelium with four to six cell layers after 3 days of culture. (Sorkio et al., 2018) However, Sorkio et al. (2018) stated that the co-culture conditions of the two cell types should be developed further to enable longer culture periods *in vitro*.

8. AIM OF THE THESIS

The lack of donor corneas needed for corneal transplantation (Gain et al., 2016) and the several drawbacks of keratoprotheses (Zhang et al., 2019b), have driven the research of 3D bioprinting of corneal structures. To enable the creation of corneal tissue and its multiple layers, different cell types must be co-cultured after 3D bioprinting of the structure. hPSC-LSCs have great potential as the cell source for the epithelial layer (Hongisto et al., 2017; Mikhailova et al., 2014), however, they require a complex medium during cell culture. Their LSC medium (CnT-07, CELLnTEC) contains various undisclosed components (CELLnTEC, 2023), and previously 3D bioprinted structures from HA-DA stromal bioink have not maintained their structural stability when cultured in this medium. This thesis aimed to enhance the stiffness and stability of this HA-DA stromal bioink in the LSC medium co-culture condition to enable the co-culture of 3D bioprinted cornea mimicking structures with stroma and epithelium. For this, photocrosslinking was chosen as the additional crosslinking approach as it is one of the most common ways of crosslinking bioinks. The HA-DA stromal bioink composition was modified by adding a HAMA component to achieve a photocrosslinkable HA-DA HAMA stromal bioink. Thus, the hypothesis of this thesis was that by adding the photocrosslinkable component, HAMA, to the existing HA-DA stromal bioink, the structural stability of bioprinted stromal structures could be enhanced in the co-culture condition. The main objectives of this thesis were as follows:

- 1) To optimize the HA-DA HAMA stromal bioink composition.
- 2) To study the effect of the HAMA component in the bioink by comparing the HA-DA and HA-DA HAMA stromal bioinks.
- 3) To study and compare the effect of LSC medium, and to determine whether the stiffness and stability of the HA-DA HAMA stromal bioink had improved in the medium.
- 4) To 3D bioprint cornea mimicking structures with stroma and epithelium.

9. MATERIALS AND METHODS

In this chapter, the materials and methods applied in the experimental part of the thesis are described. First, the HA-DA stromal bioink composition was modified by adding a HAMA component to achieve a photocrosslinkable HA-DA HAMA stromal bioink. A suitable HA-DA HAMA stromal bioink composition was determined for the LSC medium co-culture condition. Following this, the developed HA-DA HAMA stromal bioink was compared to the original HA-DA stromal bioink by characterizing the bioinks and bioprinted stromal structures after incubation in LSC medium or phosphate buffered saline (PBS). Briefly, printability, shape fidelity, viscosity, swelling behavior, handling, mechanical properties, and transparency were compared. After this, the cytocompatibility of both bioinks with hASC-CSKs was assessed and compared. Finally, based on the comparison of the HA-DA and HA-DA HAMA stromal bioink, cornea mimicking structures with stroma and epithelium were bioprinted using a different HA-DA stromal bioink for the stroma and a HA-DA bioink specific for the epithelium. Also, two different co-culture conditions were tested. The workflow of the experimental part of this thesis is presented in Figure 8.

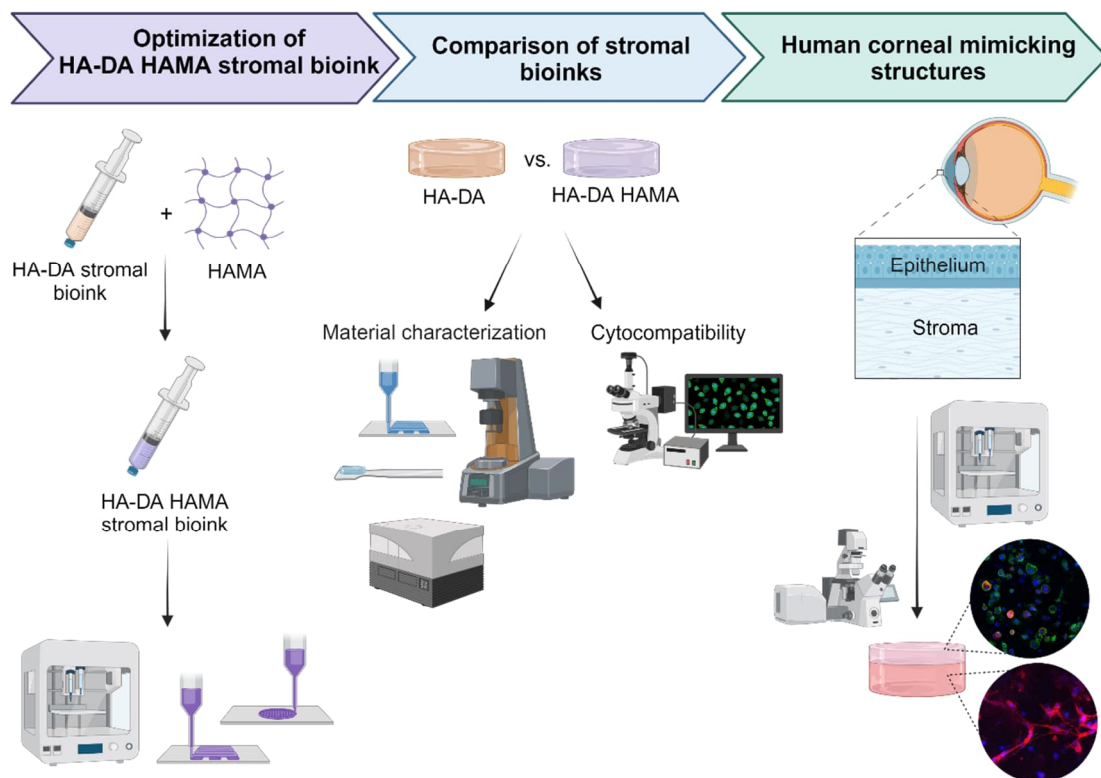


Figure 8. The workflow of the experimental part of this thesis. Created with BioRender.com

9.1 Crosslinking components for bioinks

HA-aldehyde (HA-ALD) and HA with dopamine and carbodihydrazide modification (HA-DA-CDH) were used as crosslinking components in bioinks of this thesis. HA-ALD was synthesized as previously described by Wang et al. (2013) and HA-DA-CDH synthesis was conducted as reported by Koivusalo et al. (2019). After synthesis and lyophilization, the components were stored at -20 °C before use. At the beginning of bioink preparation, both crosslinking components were dissolved into 10, 12, 13, 14 or 16 mg/ml concentration in 1X Dulbecco's Phosphate Buffered Saline (PBS, Euroclone S.p.A).

For the HA-DA HAMA stromal bioink, HAMA (PhotoHA®, CELLINK) was used as an additional crosslinking component. Stock solutions of 3% and 4% HAMA were prepared by dissolving the polymer in 1X PBS with 0.25% LAP (CELLINK) at 4 °C overnight. The dissolved HAMA solutions were stored at 4 °C.

9.2 Preparation of bioinks

The HA-DA stromal bioink was composed of the following components. HA-ALD and HA-DA-CDH were used as crosslinking components and were dissolved before bioink preparation as described in Chapter 9.1. Primary rheological modifier unmodified sodium hyaluronate (unmodified HA, Novamatrix) was dissolved in sterile 5X PBS with 0.4 M NaCl at a concentration of 1% (w/v). As an additional rheological modifier and to increase cytocompatibility, OptiCol™ Human Collagen Type I 3 mg/ml (Cell Guidance Systems Ltd) was used. Additionally, the bioink contained a 1X PBS component. Right before bioink mixing, the Human Collagen Type I was neutralized to a pH of 7.4 with 1 M NaOH in the presence of 10X Dulbecco's phosphate buffered saline (Euroclone S.p.A). The components were mixed together with a dual syringe system where a female-female Luer lock combined two syringes. After mixing with the dual syringe system for 30 s, the bioink was transferred into a 30 cc barrel (Nordson EFD) with the cartridge piston. With bioinks without cells, the bioinks were crosslinked for 20 minutes at room temperature (RT) before printing.

The HA-DA HAMA stromal bioink was prepared similarly, but the primary rheological modifier, unmodified HA, was replaced partially or fully with 3% or 4% HAMA. This will be described in detail in Chapter 9.4.

For cornea mimicking structures with stroma and epithelium, the HA-DA stromal bioink described above was used with crosslinking components HA-ALD and HA-DA-CDH dissolved into 16 mg/ml concentration. For the epithelial layer of the structure, a HA-DA

bioink specific for the epithelium was used. The composition of this bioink and preparation are described in the Confidential supplement.

9.3 3D bioprinting setup and printing procedure

The extrusion-based 3D bioprinter 3D-Bioplotter® Manufacturer Series by EnvisionTEC (Gladbeck) was used. After crosslinking the bioink, the barrel with bioink was loaded into the low temperature printhead of the 3D bioprinter and the temperature of the printhead was set at 20 °C. The UV curing head of the bioprinter was used to crosslink the HA-DA HAMA structures with following parameters: wavelength 365 nm, height from last layer 32.1 mm and UV beam brightness 60 mW/cm². When printing HA-DA and HA-DA HAMA stromal bioinks, blunt 27 G needles with an inner diameter of 200 µm (0.50 inches, CEL-LINK) were used and the needle height at first layer was set at 160 µm. Printing was performed at RT on 35 mm petri dishes (TC-treated, Corning®). Instead, for the HA-DA bioink specific for the epithelium, the needle diameter used is described in the Confidential supplement and printing was performed on printed cylindrical stromal structures. The printing of cornea mimicking structures with stroma and epithelium is explained in detail in Chapter 9.8.

The 3D models used were designed in STL format with Perfactory RP software and sliced with interval which was 80% of the inner diameter of the needle. The inner structures of the printed layers and UV programs were created in Visual machine software (EnvisionTEC, Gladbeck). The dimensions, 3D models and inner structures of the grids and cylindrical structures used in this thesis are summarized in Table 2. The printed grid and cylindrical structures were stabilized for 30 and 60 minutes respectively at 37 °C with 5% CO₂ in a humid environment which was created by pipetting 1X PBS or cell culture medium to the edges of the culture dish. After stabilization, 2 – 3 ml of cell culture medium or 1 X PBS was added to cover the printed structure and the structures were left to incubate at 37 °C with 5% CO₂.

Table 2. Summary of dimensions and inner structures of 3D bioprinted grid and cylindrical structures of this thesis

Structure	Grid structure for HA-DA HAMA stromal bioink optimization	Grid structure for printability and shape fidelity assessment	Cylindrical structure to mimic corneal stroma	Cylindrical structure to mimic corneal epithelium
<i>Dimensions</i>	15 mm x 15 mm	12.5 mm x 12.5 mm	Ø 12 mm	Ø 12 mm
<i>3D model</i>	Box	Box	Cylinder	Cylinder
<i>Slicing interval</i>	160 µm	160 µm	160 µm	<i>Found in Confidential supplement</i>
<i>Layer count</i>	6	4	4	2
<i>Inner structure</i>	Grid	Grid	Grid	Grid
<i>Distance between strands</i>	2.5 mm	2.5 mm	0.4 mm	0.4 mm
<i>Contour count</i>	1	1	1 – 2*	1
<i>Distance from contour</i>	0.1	0.16 mm	0.1 mm	0.1 mm
<i>Distance between contours</i>	-	-	0.2 mm*	-

*1 contour in cornea mimicking structures with stroma and epithelium (Chapter 9.8), other structures had 2 contours with 0.2 mm distance between contours.

9.4 Optimization of HA-DA HAMA stromal bioink

To determine the best HA-DA HAMA stromal bioink composition for the LSC medium co-culture condition, grid and cylindrical structures were printed with different bioink compositions, UV exposure times and timing of UV exposure after printing. Using 15 mm x 15 mm grid structures with six perpendicular layers and 2.5 mm distance between filaments (Table 2), printability and shape fidelity immediately after printing were evaluated by imaging the structures with the built-in camera of the 3D bioprinter. Moreover, printed four-layered cylindrical structures mimicking corneal stroma (Table 2), were used to assess the stability of the structures in the LSC medium co-culture condition by incubating the structures in LSC medium (CnT-07 Epithelial Proliferation Medium, CELLnTEC) for up to 14 days. At the end of incubation, LSC medium was removed, and the structures were handled with spatula to evaluate the stability of the structures.

First, the composition of a HA-DA stromal bioink containing crosslinking components HA-DA-CDH and HA-ALD dissolved into concentration of 14 mg/ml was modified by replacing partially or fully the primary rheological modifier, unmodified HA, with 4% HAMA (Compositions 1 and 2, Table 3). 30 s UV exposure time was used, and UV exposure of

printed structure was done 1 h after printing. Following these tests, a HA-DA stromal bioink containing crosslinking components HA-DA-CDH and HA-ALD dissolved into concentration of 12 mg/ml was modified as previously with 4% HAMA (Compositions 3 and 4, Table 3). 30, 60 and 120 s UV exposure times were tested, and UV exposure of printed structure was done 1 h after printing. Next, the concentration of stock HAMA solution was decreased from 4% to 3%. Using 3% HAMA, tests were performed with a HA-DA stromal bioink containing crosslinking components HA-DA-CDH and HA-ALD dissolved into concentration of 14 mg/ml by again partially or fully replacing the unmodified HA (Compositions 5 and 6, Table 3). 30, 60 and 120 s UV exposure times were tested, and UV exposure of printed structure was done 1 h after printing. These initially tested HA-DA HAMA stromal bioink compositions and used printing parameters are summarized in Table 3.

Table 3. *Initially tested HA-DA HAMA stromal bioink compositions and printing parameters used to print the bioinks.*

<i>Bioink composition</i>	<i>HA-DA-CDH and HA-ALD stock concentration (mg/ml)</i>	<i>HAMA stock concentration (%)</i>	<i>Amount of re-placed unmodified HA (%)</i>	<i>UV exposure time (s)</i>	<i>Timing of UV exposure after printing</i>	<i>Printing pressure and speed</i>
1	14	4	100	30	1 h	1 bar, 9 mm/s
2	14	4	50	30	1 h	1 – 1.1 bar, 8 – 9 mm/s
3	12	4	100	30, 60 or 120	1 h	0.8 – 1.1 bar, 8 mm/s
4	12	4	50	30, 60 or 120	1 h	1 bar, 8 mm/s
5	14	3	100	30, 60 or 120	1 h	0.9 – 1 bar, 8 mm/s
6	14	3	50	30, 60 or 120	1 h	1 bar, 8 mm/s

Based on these tests, HA-DA stromal bioink with HA-DA-CDH and HA-ALD dissolved into 13 – 14 mg/ml concentration where unmodified HA was fully replaced with 3% HAMA was chosen as the bioink composition for the HA-DA HAMA stromal bioink. Also, 60 s UV exposure time was settled on. From here after, this bioink will be referred to as HA-DA HAMA stromal bioink.

Finally, also timing of UV exposure after printing was tested. The HA-DA HAMA stromal bioink was tested with UV exposure given immediately after printing or 1 h after printing to printed structures. Based on the handling of the printed structures on day 7, UV exposure given immediately after printing was chosen.

9.5 Characterization of stromal bioinks

After choosing the best HA-DA HAMA stromal bioink composition, the chosen HA-DA HAMA stromal bioink was compared to the original HA-DA stromal bioink with same HA-DA-CDH and HA-ALD concentration. The compositions of these two bioinks and printing parameters used to print the bioinks are presented in Table 4.

Table 4. *Composition of stromal bioinks compared in this thesis and the printing parameters used to print the bioinks.*

Bioink	Bioink components	UV	Printing pressure and speed
HA-DA	HA-DA-CDH, HA-ALD, Unmodified HA, Col I	No UV	0.8 – 1.1 bar, 8 – 9 mm/s
HA-DA HAMA	HA-DA-CDH, HA-ALD, 3% HAMA, Col I	60 s, immediately after printing	1 – 1.1 bar, 8 -9 mm/s

These HA-DA and HA-DA HAMA stromal bioinks were compared by characterizing the printability and shape fidelity of grid structures printed with the same parameters in two different incubation conditions. As the co-culture condition, LSC medium was used. For comparison, 1X PBS was used as previously described in Möro et al. (2022). Also, shear-thinning properties of the bioinks were compared by measuring their viscosities. In addition, cylindrical structures to mimic corneal stroma (Table 2) were printed to analyze the stability and handling, swelling behavior, transparency, and mechanical properties of the two bioinks in the two different incubation conditions.

9.5.1 Printability and shape fidelity

Printability and shape fidelity of the two bioinks were compared by printing 12.5 mm x 12.5 mm grids with four perpendicular layers and 2.5 mm distance between filaments (Table 2). Printing parameters of 1.1 bar pressure and 8 mm/s speed were used to print the four layered grid structures. The printed structures were imaged with the built-in camera of the 3D bioprinter immediately after printing and after incubation in PBS or LSC medium for 7 and 14 days at 37 °C with 5% CO₂. On day 7 and 14, the liquid was carefully removed before imaging. ImageJ Fiji software was used to measure filament thickness, pore area and perimeter of the pore from the images. Eight randomly selected filaments

and the nine center pores were analyzed at each time point from each grid structure. Also, the number of remaining open pores in the grid structures were counted. On day 0, immediately after printing six grid replicates were analyzed (n=6) and on day 7 and 14 three grid replicates were analyzed (n=3) for each condition. The shape of the pore was analyzed further by calculating its pore factor using Equation 1.

9.5.2 Viscosity of bioinks

Viscosities of HA-DA HAMA and HA-DA stromal bioinks were measured with Discovery HR-2 hybrid rheometer (TA Instruments) to determine the shear-thinning properties of the two bioinks. Continuous flow sweeps with shear rate ranging from 0.01 to 100 1/s were performed for all samples with 20 mm parallel plate geometry at 20 °C. A 1 mm gap was set manually for each sample to prevent over- and underfill. The bioinks were prepared before measurement as described previously in Chapter 9.2 into a syringe. After 20 minutes of crosslinking, 400 – 500 µl of bioink was injected between the plates of the rheometer and measurement of the first replicate was started. All in all, four 400 – 500 µl bioink replicates were measured (n=4) per bioink. The measurements were performed within 1 h of starting the measurement of the first replicate.

9.5.3 Swelling behavior of bioprinted structures

Bioprinted cylindrical stromal structures (Table 2) were incubated in PBS or LSC medium at 37 °C with 5% CO₂ to analyze the swelling behavior of the bioinks in different incubation conditions. Four replicates for both incubation conditions were printed from HA-DA stromal bioink (n=4) and five replicates for both incubation conditions were printed from HA-DA HAMA stromal bioink (n=5). The structures were printed on pre-weighed cell culture dishes. After 1 h of stabilization and 30 minutes of immersion into incubation medium, the liquid was carefully removed, and initial weight of the structure was determined. The printed structures were also weighed on day 1, 3, 7, 10 and 14, and incubation medium was removed carefully each time. The swelling behavior of the structures was analyzed by calculating the remaining weight percentage at each timepoint using Equation 2.

9.5.4 Handling of bioprinted structures

The handling of bioprinted HA-DA and HA-DA HAMA cylindrical stromal structures (Table 2) was evaluated on day 7 and 14 after incubation in PBS or LSC medium. Before handling, incubation medium was removed carefully. The structures were then handled with a spatula and imaged with mobile phone camera during handling.

9.5.5 Rheology of bioprinted structures

Viscoelastic properties of bioprinted HA-DA and HA-DA HAMA cylindrical stromal structures (Table 2) incubated in PBS or LSC medium were assessed by performing amplitude and frequency sweeps using the Discovery HR-2 hybrid rheometer (TA Instruments). Measurements were performed on day 1 and 7 after printing. Before each measurement, the incubation solution was carefully removed, and an 8 mm diameter cylinder was punched out from the printed structure with an 8 mm biopsy punch (Kai Industries Co., Ltd.). This piece of the printed structure was then set between the plates of the rheometer using a spatula. The gap was set manually for each sample ranging from 400 to 1100 μm .

Amplitude sweeps with oscillation strain ranging from 0.1% to 100% and a constant frequency of 1 Hz were performed with 8 mm parallel plate geometry at 20 °C. Based on amplitude sweeps, 1% strain was selected for frequency sweeps. Frequency sweeps with frequency ranging from 0.1 Hz to 10 Hz were performed with 8 mm parallel plate geometry at 20 °C. Number of parallel replicates in amplitude and frequency sweeps are presented in Table 5.

Table 5. *Number of parallel replicates in amplitude and frequency sweeps.*

<i>Timepoint</i>	<i>Incubation condition</i>	<i>Amplitude sweep</i>		<i>Frequency sweep</i>	
		<i>HA-DA</i>	<i>HA-DA HAMA</i>	<i>HA-DA</i>	<i>HA-DA HAMA</i>
Day 1	PBS	3	2	4	4
	LSC Medium	3	2	5	4
Day 7	PBS	2	2	4	5
	LSC Medium	3	2	4	3

9.5.6 Transparency

Transparency of bioprinted cylindrical stromal structures (Table 2) was examined visually and by measuring light absorbance using a multimode microplate reader (Spark®, Tecan). Visually the transparency was evaluated from printed acellular structures and cell-laden structures. The incubation medium was removed carefully from the culture dish. The culture dish with the structure was placed on printed text and imaged with mobile phone camera. Transparency of printed acellular HA-DA and HA-DA HAMA stromal structures in PBS or LSC medium were visually evaluated on day 1, 7 and 14 after printing. Similarly, the transparency of printed cell-laden structures was evaluated on day 1 and 7 after printing.

Light absorbance was measured on day 1 after printing, from printed acellular HA-DA and HA-DA HAMA stromal structures in LSC medium as previously reported by Kim et al. (2019b). Samples were washed before measurement for 1 h by changing 1X PBS once. 5 mm diameter cylinders were punched out from the printed structure with a 5 mm biopsy punch (Surgi-Cut®, Paramount Surgimed Ltd). The cylinders were placed into the wells of a 96 well plate (Nunclon 96 flat transparent, Thermo Fisher Scientific) and 20 µl of 1X PBS was pipetted on top of samples to prevent drying. As control, 90 µl of 1X PBS was pipetted into separate wells of the well plate. The light absorbance values in the range of 400 – 700 nm were measured with a wavelength step size of 5 nm at RT. Measurements were performed in triplicates (n=3). From the measured light absorbance values, light transmittance (T) was calculated with the following equation:

$$T (\%) = \frac{1}{10^A} \times 100$$

where A is the measured light absorbance.

9.6 Cells

hASC-CSKs were used to evaluate the cytocompatibility of the HA-DA and HA-DA HAMA stromal bioinks which is described in Chapter 9.7. hASC-CSKs were also used as the cell type for the stromal layer in cornea mimicking structures with stroma and epithelium. hASC-CSKs were chosen due to the multiple advantages of hASCs discussed in Chapter 4.3 and due to being previously used for 3D bioprinting by the research group (Mörö et al., 2022). The differentiation of hASC-CSKs is described in Chapter 9.6.2. Instead, ABCG2 enriched hPSC-LSCs were chosen as cell type for the epithelial layer of the cornea mimicking structure with stroma and epithelium due to extensive knowledge of these cells in the research group (Vattulainen et al., 2021, 2019).

9.6.1 hASC ethical statement

The hASC 5/18 were used under approvals from Regional Ethics Committee of the Expert Responsibility area of Tampere University Hospital that allow to extract and use hASCs for research purposes (R15161).

9.6.2 hASC-CSKs

For each cell experiment, a frozen stock of 0.5 million hASCs 5/18 were thawed, centrifuged and the supernatant was removed. Next, the hASCs were resuspended in hASC medium consisting of DMEM/F-12 (Gibco) supplemented with 5% Human Serum (Serena), 1% GlutaMAX™ (Gibco) and 1% penicillin-streptomycin (Gibco) and plated

into 2 or 3 T75 culture flasks (Nunc™ EasYFlask™ Cell Culture Flask, Thermo Fisher Scientific). The hASCs were stored in an incubator at 37 °C with 5% CO₂ and cultured for 4 – 6 days to expand cell amount. The cell culture medium was changed three times a week.

After expansion, the hASCs were washed with 1X PBS and enzymatically detached with TrypLE™ Select (Gibco). After 8 minutes of incubation at 37 °C with 5% CO₂, TrypLE™ was removed and hASC medium was added to the flasks. Subsequently, hASCs were centrifuged, the supernatant was removed, and the cells were resuspended in keratocyte differentiation medium (KDM) for counting with an automated cell counter (NucleoCounter® NC-202™, ChemoMetec). For differentiation, hASCs were plated at 7000 cells/cm² into CellBIND® T75 culture flasks (Corning®) in KDM consisting of Advanced DMEM (Gibco) supplemented with 1% GlutaMAX™, 1% penicillin-streptomycin 10 ng/ml basic human fibroblast growth factor (hFGF, PeproTech), 0.1 mM ascorbic acid-2-phosphate (Sigma-Aldrich) and 1 µM retinoic acid (Sigma-Aldrich). During the first five days of differentiation, the KDM was changed every day, after which the medium was changed three times a week. The hASCs were differentiated at passage 4 for two weeks before bioprinting. At time of bioprinting, hASCs differentiated towards CSKs were called hASC-CSKs.

On day 14 of differentiation, the hASC-CSKs were briefly washed with 1X PBS and detached with TrypLE™. After 16 minutes of incubation at 37 °C with 5% CO₂, Defined Trypsin Inhibitor (DTI, Gibco) was added. Next, the cells were centrifuged, and resuspended in KDM for counting with Bürker chamber. Subsequently, hASC-CSKs were centrifuged, resuspended in the 1X PBS component of the bioink and mixed as described in Chapter 9.2.

For the assessment of HA-DA and HA-DA HAMA stromal bioink cytocompatibility, cell density in the bioinks was 3 million cells/ml. These bioinks with cells were crosslinked for 40 – 55 minutes in the syringe barrel at RT before printing. Instead, in the stromal layer of cornea mimicking structures with stroma and epithelium, cell density of the HA-DA stromal bioink was 4 million cells/ml. This stromal bioink was crosslinked for 10 minutes in the syringe barrel before printing.

9.6.3 hPSC-LSCs

ABCG2 enriched hPSC-LSC population was used in the printing of the epithelial layer in the cornea mimicking structures with stroma and epithelium. The hPSC-LSCs from human iPSC line WT003.TAU.bC were derived as previously described by Vattulainen et al. (2019) and maintained in standard CnT-30 (CELLnTEC) differentiation conditions with

EC supplementation (50 ng/ml mouse recombinant epidermal growth factor (EGF, Invitrogen) and 3 μ M CHIR-99021 (Stemgent)) from day 10 for 3 passages before cryostorage. For printing, a frozen stock of hPSC-LSCs was thawed, centrifuged and the supernatant was removed. Next, the cells were resuspended in LSC medium (CnT-07, CELLnTEC) and plated onto round 100 mm cell culture dishes (Corning Falcon) coated with 5 μ g/cm² human placental Col IV (Sigma-Aldrich) and 0.5 μ g/cm² recombinant LN521 (LN521™, Biolamina). The hPSC-LSCs were stored in an incubator at 37 °C with 5% CO₂ and cultured for 7 days to expand cell amount. On day 7, the cells were briefly washed with 1X PBS and detached by enzymatic dissociation with TrypLE™ by incubating at 37 °C with 5% CO₂ for 4 minutes. After incubation, DTI was added, the cells were centrifuged, and resuspended in LSC medium for counting with Bürker chamber. Next, the hPSC-LSCs were centrifuged and resuspended in desired volume of LSC medium for the bioink preparation described in the Confidential supplement. hPSC-LSC cell density of the HA-DA bioink specific for the epithelium is reported in the Confidential supplement.

9.7 Cytocompatibility of stromal bioinks

The cytocompatibility of the HA-DA and HA-DA HAMA stromal bioinks were evaluated by printing the bioinks with hASC-CSKs into cylindrical stromal structures (Table 2). The cytocompatibility was assessed with Live/Dead analysis and IF staining. Also, the effect of UV exposure time on hASC-CSKs in HA-DA HAMA stromal structures was evaluated with Live/Dead analysis. The different cell-laden structures compared, and UV parameters used are presented in Table 6.

Table 6. Compared bioinks, UV and printing parameters.

<i>Bioink</i>	<i>UV exposure time</i>	<i>Printing pressure and speed</i>
HA-DA	No UV	0.4 – 0.8 bar, 8 – 9.6 mm/s
HA-DA HAMA	No UV	0.9 – 1 bar, 9.5 mm/s
HA-DA HAMA	UV 30 s, immediately after printing	0.7 – 0.9 bar, 9.5 – 12 mm/s
HA-DA HAMA	UV 60 s, immediately after printing	0.5 – 0.9 bar, 9.5 – 14.4 mm/s

9.7.1 Cell culture of 3D bioprinted stromal structures

The morphology of hASC-CSKs after bioprinting was followed by imaging samples with phase contrast microscope (Primovert, Carl Zeiss). Culture medium of printed cell-laden stromal structures was changed three times a week. The bioprinted stromal structures were cultured up to 21 days *in vitro*. The printed cell-laden stromal structures used to

study cytocompatibility of the bioinks (Table 6) were cultured in KDM. Additionally, one HA-DA cell-laden stromal structure, one HA-DA HAMA cell-laden stromal structure with 30 s UV exposure time and one HA-DA HAMA cell-laden stromal structure with 60 s UV exposure time were cultured in LSC medium (CnT-07, CELLnTEC) to assess the stability of these cell-laden stromal structures in the co-culture condition. The stability of these structures was followed visually and by imaging with phase contrast microscope.

9.7.2 Live/Dead

Viability of hASC-CSKs in HA-DA and HA-DA HAMA stromal structures with different UV exposure times (Table 6) were evaluated on day 1 and 7 with Live/Dead® Viability/Cytotoxicity Kit for mammalian cells (Thermo Fischer Scientific). Also, Live/Dead staining was performed for cell-laden HA-DA HAMA structures in LSC medium on day 14. The reagent solution consisted of calcein-acetoxymethyl ester (Ca-AM, live stain) and ethidium homodimer-1 (EthD-1, dead stain). Live/Dead staining was carried out with different protocols with different samples at different timepoints due to problems with permeability of stains. The incubation time in reagent solution and concentration of EthD-1 were changed. The reagent solution was made into 8 ml of 1X PBS and each time 1 µl of Ca-AM was added. The used protocols for each sample at each time point are summarized in Table 7.

Table 7. *Live/Dead protocols*

<i>Sample and time point</i>	<i>Incubation time</i>	<i>Volume of EthD-1</i>	<i>Volume of Ca-AM</i>	<i>Volume of PBS</i>
<i>HA-DA Day 1</i>	30 min	3 µl	1 µl	8 ml
<i>HA-DA Day 7</i>	30 min	3 µl	1 µl	8 ml
<i>HA-DA HAMA Day 1</i>	60 min	3 µl	1 µl	8 ml
<i>HA-DA HAMA Day 7</i>	60 min	1 µl	1 µl	8 ml
<i>HA-DA HAMA in LSC medium Day 14</i>	60 min	1 µl	1 µl	8 ml

Each time before adding reagent solution, the samples were briefly washed in 1X PBS. After incubation in reagent solution at 37 °C with 5% CO₂, the samples were imaged with Leica Dmi8 (Leica Microsystems). Z-stack images were taken, following which images were converted to maximum intensity projections (MIPs) and edited in ImageJ Fiji.

9.7.3 Immunofluorescence staining

IF staining was used to evaluate cell morphology, tissue formation and expression of cornea stroma specific markers in bioprinted HA-DA and HA-DA HAMA cylindrical stromal structures containing hASC-CSKs. Timepoints and performed staining are presented in Table 8. Alongside nuclei stain Hoechst, phalloidin stained actin filaments and gap junction protein connexin 43 (Cx43) staining were used to evaluate cell morphology and tissue formation whereas Col I and lumican were stained as cornea stroma specific markers.

Table 8. IF staining performed for each cell-laden HA-DA and HA-DA HAMA structure

<i>Bioink</i>	<i>Phalloidin, Cx43, Hoechst</i>	<i>Col I, Lumican, Hoechst</i>
HA-DA	Day 7 and 21	Day 7, 14 and 21
HA-DA HAMA, UV 30 s	Day 7 and 14	Day 14
HA-DA HAMA, UV 60 s	Day 7, 14 and 21	Day 14 and 21

At each timepoint, the sample was washed three times with 1X PBS and fixed with 4% paraformaldehyde (PFA, Electron Microscopy Sciences) for 45 minutes at RT. After fixing, samples were washed twice with 1X PBS and stored in 1X PBS at 4 °C. For permeabilization and blocking, fixed samples were incubated in 5% bovine serum albumin (BSA, Sigma-Aldrich) in 1X PBS with 0.1% Triton X-100 (Sigma-Aldrich) over night at RT. Thereafter, the primary antibodies in 5% BSA in 1X PBS were added. After incubation for 3 days at 4 °C, the samples were washed for 2 days by changing 1X PBS three times. Next, secondary antibodies in 5% BSA in 1X PBS were added and incubated over night at RT. Subsequently, the samples were washed over night by changing the 1X PBS three times. Finally, the samples were mounted with Vectashield® Antifade Mounting medium (Vector Laboratories) on glass bottom MatTek dishes (MatTek corporation) and stored at 4 °C. Before imaging, excess mounting medium was removed and cover slips were placed on top of the samples. The samples were imaged using confocal microscope (LSM 800, Zeiss). Taken z-stack images were deconvoluted with Huygens Essential software (Scientific Volume Imaging) following which the images were converted to MIPs and edited in ImageJ Fiji. Imaris (Oxford 12 Instruments) was used to create orthogonal visualizations of the z-stack images. The antibodies used for comparing HA-DA and HA-DA HAMA stromal structures with hASC-CSKs are summarized in Table 9.

Table 9. Summary of antibodies and other staining used for IF staining comparing HA-DA and HA-DA HAMA stromal structures with hASC-CSKs.

Antibody	Use	Manufacturer	Dilution
Primary Antibodies			
<i>Anti-Cx43, rabbit</i>	Visualization of gap junction protein Cx43	Abcam	1:100
<i>Anti-Col I, mouse</i>	Visualization of Col I	Abcam	1:100
<i>Anti-lumican, goat</i>	Visualization of lumican	R&D systems	1:50
Secondary Antibodies			
<i>Anti-rabbit, A488</i>	Binds to primary antibodies from rabbit	Invitrogen	1:400
<i>Anti-mouse, A488</i>	Binds to primary antibodies from mouse	Invitrogen	1:400
<i>Anti-goat, A568</i>	Binds to primary antibodies from goat	Invitrogen	1:400
Other			
<i>Phalloidin-tetramethylrhodamine B isothiocyanate A568</i>	Visualization of actin filaments	Sigma-Aldrich	1:80
<i>Hoechst 33342</i>	Visualization of cell nuclei	Invitrogen	1:1000

9.8 Human cornea mimicking structures with stroma and epithelium

In the final stage of this thesis, after characterizing and comparing the HA-DA and HA-DA HAMA stromal bioinks, cornea mimicking structures with stroma and epithelium were bioprinted. Based on the results, a HA-DA stromal bioink with an increased concentration of crosslinking components HA-ALD and HA-DA-CDH (Chapter 9.2) was used with hASC-CSKs for the stromal layer (Chapter 9.6.2). Instead, for the epithelial layer of the structure, a HA-DA bioink specific for the epithelium was used (Chapter 9.2) with hPSC-LSCs as cell type for the epithelial layer (Chapter 9.6.3). In addition to testing a proof-of-concept for extrusion-based 3D bioprinting of human cornea mimicking structures with stroma and epithelium, two different co-culture conditions were tested.

9.8.1 3D bioprinting procedure

After precrosslinking of bioinks, printing of cornea mimicking structures with stroma and epithelium was started. Each cornea mimicking structure was printed by first printing the stromal layer onto a petri dish. As the stromal layer, a four layered 12 mm diameter cylinder was printed (Table 2) with printing parameters of 1.1 – 1.2 bar pressure and 5 – 9 mm/s speed. Next, the epithelial layer was immediately printed on top of the stromal layer. As epithelial layer, a two layered 12 mm diameter cylinder was printed (Table 2) with printing parameters stated in the Confidential supplement. After printing, the structures were stabilized for 1 h as previously described in Chapter 9.3 before adding cell culture medium.

9.8.2 Co-culture of cornea mimicking structures

Cornea mimicking structures with stroma and epithelium were cultured in LSC medium (CnT-07, CELLnTEC) or a 1:1 mixture of KDM and LSC medium (KDM+LSC) to test two different co-culture conditions. For the first day after printing, the mediums contained 1 μ l/ml ROCK Inhibitor (Y-27632, Stemcell Technologies). On day 2, the culture medium was changed to the same culture medium without ROCK Inhibitor. After this, culture medium was changed three times a week. The bioprinted cornea mimicking structures were cultured up to 7 days *in vitro*.

9.8.3 Analysis of cornea mimicking structures

After printing, the morphology of hASC-CSKs and hPSC-LSCs in cornea mimicking structures with stroma and epithelium was followed with phase contrast microscope. Moreover, on day 4 and 7, IF staining was used to evaluate cell morphology as well as expression of LSC marker ABCG2 in the printed structures. The same IF staining and imaging protocol was used as previously in Chapter 9.7.3. The used antibodies are summarized in Table 10.

Table 10. Summary of antibodies and other staining used for IF staining of cornea mimicking structures.

Antibody	Use	Manufacturer	Dilution
Primary Antibody <i>Anti-ABCG2 (5D3), mouse</i>	Visualization of ABCG2, a biomarker for putative LSCs	Millipore	1:200
Secondary Antibody <i>Anti-mouse, A488</i>	Binds to primary antibodies from mouse	Invitrogen	1:400
Other <i>Phalloidin-tetramethylrhodamine B isothiocyanate A568</i>	Visualization of actin filaments	Sigma-Aldrich	1:80
<i>Hoechst 33342</i>	Visualization of cell nuclei	Invitrogen	1:1000

9.9 Statistical Analysis

Statistical analysis of printability, shape fidelity and storage moduli were done with IBM SPSS Statistics software. Nonparametric Mann-Whitney U test was used to determine statistical differences in filament thickness and pore factor between the two bioinks immediately after printing as well as differences between the storage moduli on day 1 and day 7. Nonparametric Kruskal-Wallis test was used for discovering statistical differences in relative filament thickness, relative pore area, and storage moduli between the bioinks in different incubation conditions. P-values < 0.05 were considered statistically significant.

10. RESULTS

10.1 Optimization of HA-DA HAMA stromal bioink

With the aim to enhance the stiffness and stability of the HA-DA stromal bioink, the best HA-DA HAMA stromal bioink composition for the LSC medium co-culture condition was first determined. Six different compositions were initially tested (Table 3). All compositions demonstrated good printability (Figure 9). Printed filaments were uniform and grid structures were clear for all bioink compositions. Some minor filament merging could be observed at the crossroads in grid structures for all bioink compositions. These observations indicate that all bioinks had good shape fidelity immediately after printing when compared to original 3D model. Moreover, cylindrical stromal structures were printed, and the effect of different UV exposure times was investigated. All structures stayed stable until the end of incubation and attached to the bottom of the printing substrate. To determine the best composition, handling of structures after incubation in LSC medium was chosen as the deciding factor. Since all bioink compositions in LSC medium were very soft it was difficult to detect small differences in handling as the handling was carried out by hand with a spatula.

Of all compositions, structures printed from compositions 1 and 2 with 4% HAMA and crosslinking components HA-DA-CDH and HA-ALD dissolved into concentration of 14 mg/ml were the softest after incubation in LSC medium. Composition 2 where half of the unmodified HA had been replaced with 4% HAMA was so soft that it could not be lifted onto the spatula on day 6 and broke during handling (Figure 9). Next, compositions 3, 4, 5 and 6 were tested with different UV exposure times. All structures printed with these compositions could be lifted onto spatula (Figure 9).

For composition 3 and 4, a longer UV exposure seemed to make the structure slightly stiffer and easier to handle. However, when lifted with a spatula all structures elongated significantly during lifting and had slightly lost their shape when on the spatula. This is demonstrated for composition 3 and 4 with 30 s UV exposure time in Figure 9. Even though not shown in Figure 9, structures with 60 and 120 s UV behaved similarly.

For composition 5 and 6, UV exposure time of 60 s seemed to make the structure slightly stiffer when compared to 30 s UV exposure time. No significant differences were observed between 60 and 120 s UV exposure time. In contrast to other bioink compositions, structures printed from compositions 5 and 6 did not elongate and kept their original

shape better when lifted with a spatula. Images of structures printed with composition 5 and 6 using different UV exposure times are presented in Figure 9.

Based on these observations, compositions 5 and 6 were chosen as best candidates for the HA-DA HAMA stromal bioink. No significant difference was observed between composition 5, where the unmodified HA had been fully replaced with 3% HAMA, and composition 6, where half of the unmodified HA had been replaced with 3% HAMA. Consequently, composition 5 was chosen based on aiming for a more densely crosslinked hydrogel network in the bioprinted structures by having higher HAMA concentration in the bioink. As UV exposure time of 60 s seemed to make the structures printed from composition 5 slightly stiffer, the 60 s UV exposure time was chosen.

Finally, timing of UV exposure after printing was investigated. Stromal structures printed with the chosen HA-DA HAMA stromal bioink were exposed to UV immediately after printing or 1 h after printing. On day 7 after printing the structures were handled. Structures exposed to UV immediately after printing kept their original shape better and seemed stiffer when handled. Therefore, UV exposure given immediately after printing was continued with for bioink characterization and cytocompatibility tests.

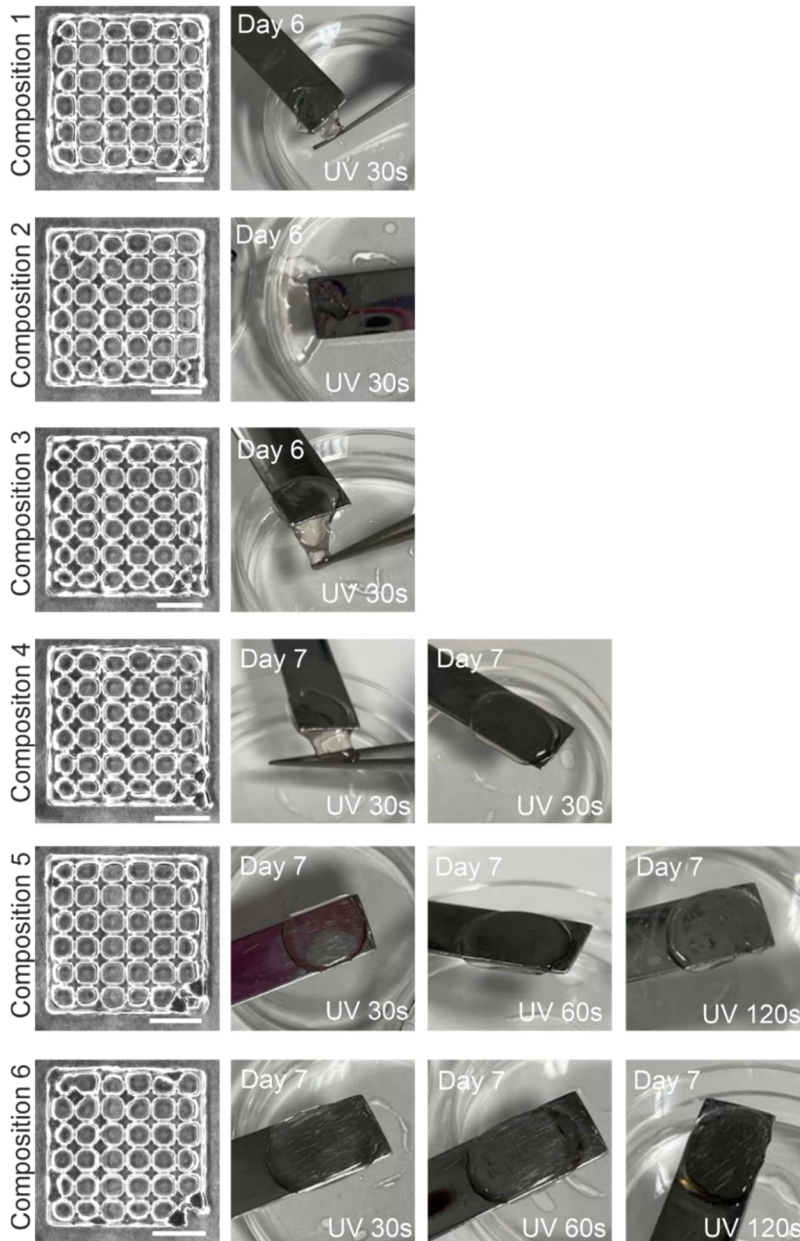


Figure 9. Initially tested HA-DA HAMA stromal bioink compositions. For each HA-DA HAMA stromal bioink composition, printed grid structure images immediately after printing for printability evaluation, and image of structure during handling on day 6 or 7. UV exposure time for each structure indicated in lower right corner. Scale bars 5 mm.

10.2 Characterization of stromal bioinks

After optimization of the HA-DA HAMA stromal bioink composition, the chosen HA-DA HAMA stromal bioink was compared to the original HA-DA stromal bioink with same HA-DA-CDH and HA-ALD concentration. These two bioinks were compared by characterizing the bioinks and their properties in two different incubation conditions: LSC medium co-culture condition and PBS. The results for printability, shape fidelity, swelling behavior, handling, rheological measurements, and transparency of the two bioinks are presented next.

10.2.1 Printability

The printability of the HA-DA and HA-DA HAMA stromal bioinks were compared by printing grid structures with four perpendicular layers with printing parameters of 1.1 bar pressure and 8 mm/s speed (Figure 10A). Overall, both bioinks demonstrated good printability with 27 G needle. Printed filaments were uniform and grid structures were clear with both bioinks. Some filament merging could be observed at the crossroads.

To further assess the printability of the bioinks, filament thickness was measured (Figure 10B) and pore factor was calculated (Figure 10C). Average filament thickness was greater ($p < 0.05$) for HA-DA stromal bioink (0.71 ± 0.07 mm) than for HA-DA HAMA stromal bioink (0.66 ± 0.06 mm) immediately after printing. Instead, the pore factor was similar between bioinks. The pore factor of the HA-DA stromal bioink was 0.88 ± 0.06 mm and for HA-DA HAMA stromal bioink 0.88 ± 0.04 mm. The pore factor was slightly below 1 but remained close to 1 for both bioinks. This indicates a slight circular shape of the pore, but still good shape fidelity compared to original 3D model. This is supported by the images of the grid structures (Figure 10A).

The shear-thinning properties of the bioinks were assessed by measuring their viscosities (Figure 11). Based on viscosity measurements, the peak viscosity value for the HA-DA stromal bioink was 826 ± 425 Pa·s and for the HA-DA HAMA stromal bioink 1028 ± 451 Pa·s, respectively. For both bioinks, the viscosities decreased as the shear rate was increased demonstrating shear-thinning properties for the bioinks. The shear-thinning behavior of the bioinks support the good printability seen with filament thickness and pore factor analysis in Figure 10.

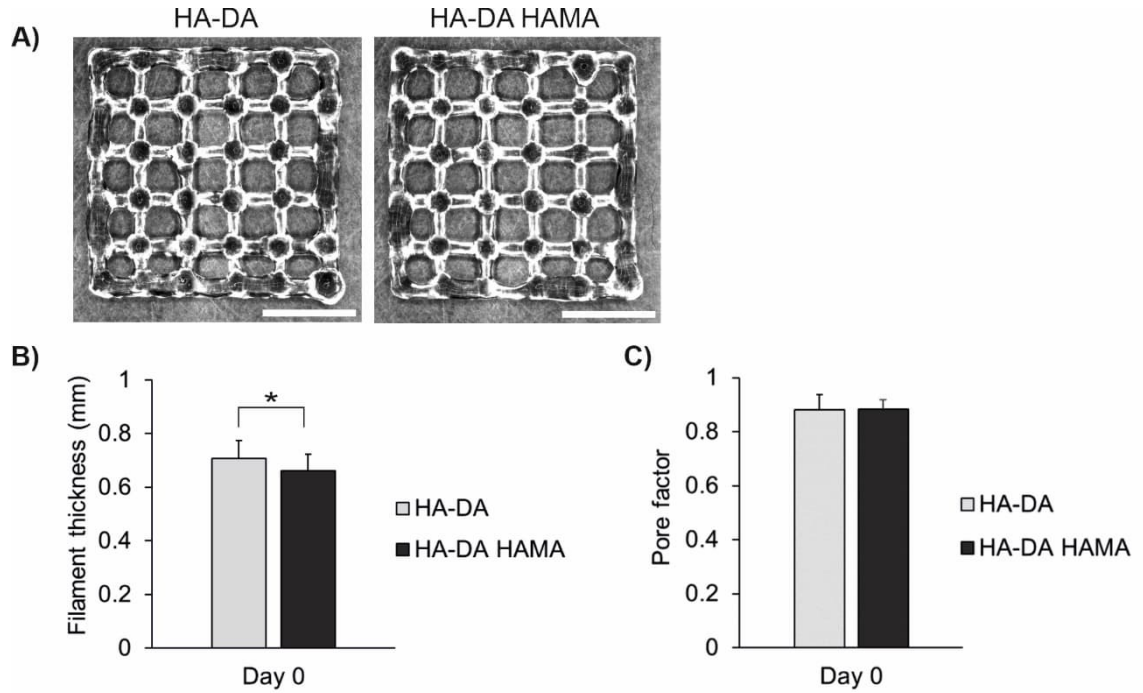


Figure 10. Printability of HA-DA and HA-DA HAMA stromal bioinks. Images of the printed grid structures (A), filament thickness ($p < 0.05$, $n=6$) (B) and pore factor ($n=6$) (C) on day 0. Scale bars 5 mm. Data is presented as mean values with \pm standard deviation.

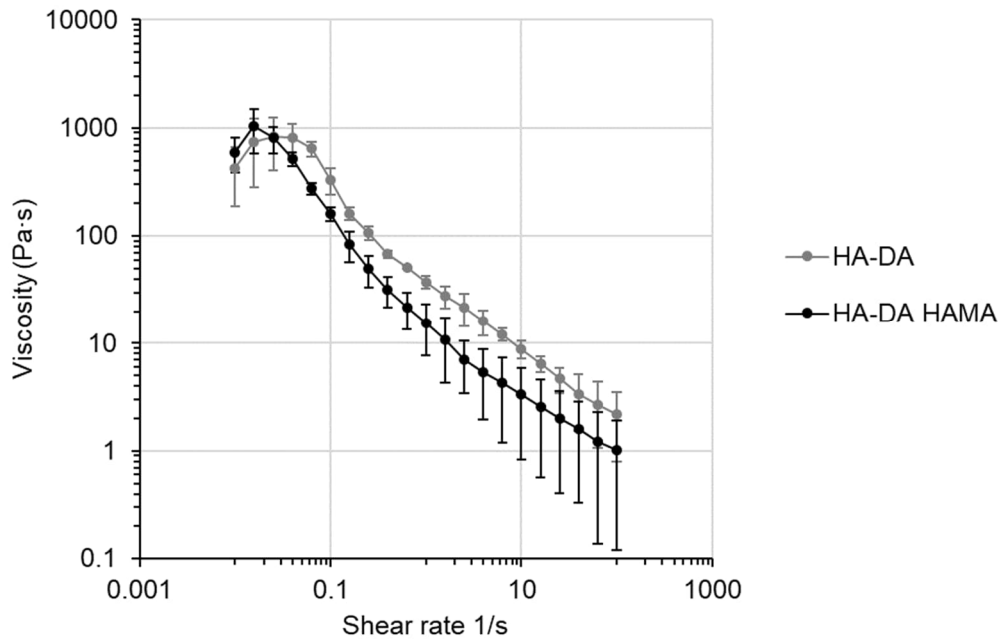


Figure 11. Viscosity with increasing shear rates for HA-DA and HA-DA HAMA stromal bioinks ($n=4$). Data is presented as mean values with \pm standard deviation.

10.2.2 Shape fidelity during incubation

Four layered grid structures were incubated in PBS or LSC medium to assess the effect of bioink composition and incubation conditions on shape fidelity of the structure. With both HA-DA and HA-DA HAMA stromal bioinks, filament swelling after immersion into incubation solution could be visually observed by comparing images taken immediately after printing (Figure 10A) to images of grid structures during incubation (Figure 12A). Moreover, more visible filament swelling could be observed in grids incubated in LSC medium (Figure 12A). Additionally, some of the pores at the edges of the grids had completely closed in both HA-DA and HA-DA HAMA grids during incubation in LSC medium. Furthermore, in one of the HA-DA grids in LSC medium, 2 pores of the 9 center pores had closed completely. On day 14 of incubation in LSC medium, from the 25 original pores, 8 ± 3 pores in HA-DA grids and 7 ± 2 pores in HA-DA HAMA grids had closed. Instead, all pores remained open in grids incubated in PBS indicating better stability of the bioinks in PBS.

To quantify the observed swelling, filament thickness was measured, and pore area was calculated from images taken of grid structures immediately after printing and on day 7 and 14 of incubation. The measured filament thickness is presented as relative filament thickness where the filament thicknesses on day 7 and 14 are normalized against day 0 (Figure 12B). Also, the measured pore area is presented as relative pore area where the pore areas on day 7 and 14 are normalized against day 0 (Figure 12C).

Between day 0 and 7 the average filament thickness increased for both bioinks in PBS and LSC medium indicating swelling of the filament caused by immersion into incubation medium (Figure 12B). The changes in pore area during the incubation period supports these results. Between day 0 and 7 the average pore area decreased for both bioinks in PBS and LSC medium (Figure 12C).

On day 7, for both bioinks, the relative filament thickness was significantly higher ($p < 0.05$) in LSC medium than in PBS (Figure 12B). This indicates that the bioinks had better shape fidelity in PBS than in LSC medium. On day 7, the average filament thickness for HA-DA stromal bioink was 1.29 ± 0.09 and 1.67 ± 0.10 times the initial filament thickness on day 0 in PBS and LSC medium, respectively. Similarly, the average filament thickness on day 7 for HA-DA HAMA stromal bioink was 1.25 ± 0.09 and 1.65 ± 0.14 times the initial filament thickness on day 0 in PBS and LSC medium, respectively. There was no significant difference in filament thicknesses between the bioinks in same incubation conditions indicating similar shape fidelity on day 7 (Figure 12B).

On day 14, in LSC medium the filament thickness had significantly ($p < 0.05$) increased when compared to day 0 for both bioinks (Figure 12B). The increase in filament thickness from day 7 to day 14 was greater for the HA-DA stromal bioink than for the HA-DA HAMA stromal bioink. On day 14 in LSC medium, the HA-DA stromal bioink was 2.04 ± 0.19 times the initial filament thickness on day 0 whereas the HA-DA HAMA stromal bioink was 1.82 ± 0.13 times the initial filament thickness on day 0. Similarly, on day 14, in LSC medium pore area had significantly ($p < 0.05$) decreased when compared to day 0 for both bioinks (Figure 12C). The decrease in pore area from day 7 to day 14 was greater for the HA-DA stromal bioink than for the HA-DA HAMA stromal bioink. On day 7, the average pore area in LSC medium for the HA-DA stromal bioink was 0.52 ± 0.10 and for the HA-DA HAMA stromal bioink 0.53 ± 0.10 times the initial pore area on day 0 whereas on day 14, the HA-DA stromal bioink was 0.28 ± 0.11 and the HA-DA HAMA stromal bioink was 0.40 ± 0.07 times the initial pore area on day 0. These findings imply that on day 14 in LSC medium the HA-DA HAMA stromal bioink had better shape fidelity than the HA-DA stromal bioink.

Instead, the filament thickness slightly decreased from day 7 to day 14 in PBS for both bioinks (Figure 12B). This decrease of the filament thickness from day 7 to day 14 was slightly greater for the HA-DA stromal bioink than for the HA-DA HAMA stromal bioink. On day 14, the average filament thickness in PBS for HA-DA stromal bioink was 1.15 ± 0.09 and for HA-DA HAMA stromal bioink 1.22 ± 0.10 times the initial filament thickness on day 0. Similarly, on day 14 in PBS the pore area increased between day 7 and 14 (Figure 12C). On day 7, the average pore area in PBS for the HA-DA stromal bioink was 0.75 ± 0.06 and for the HA-DA HAMA stromal bioink 0.80 ± 0.06 times the initial pore area on day 0 whereas on day 14, the average pore area for the HA-DA stromal bioink was 0.84 ± 0.11 and for the HA-DA HAMA stromal bioink 0.84 ± 0.05 times the initial pore area on day 0.

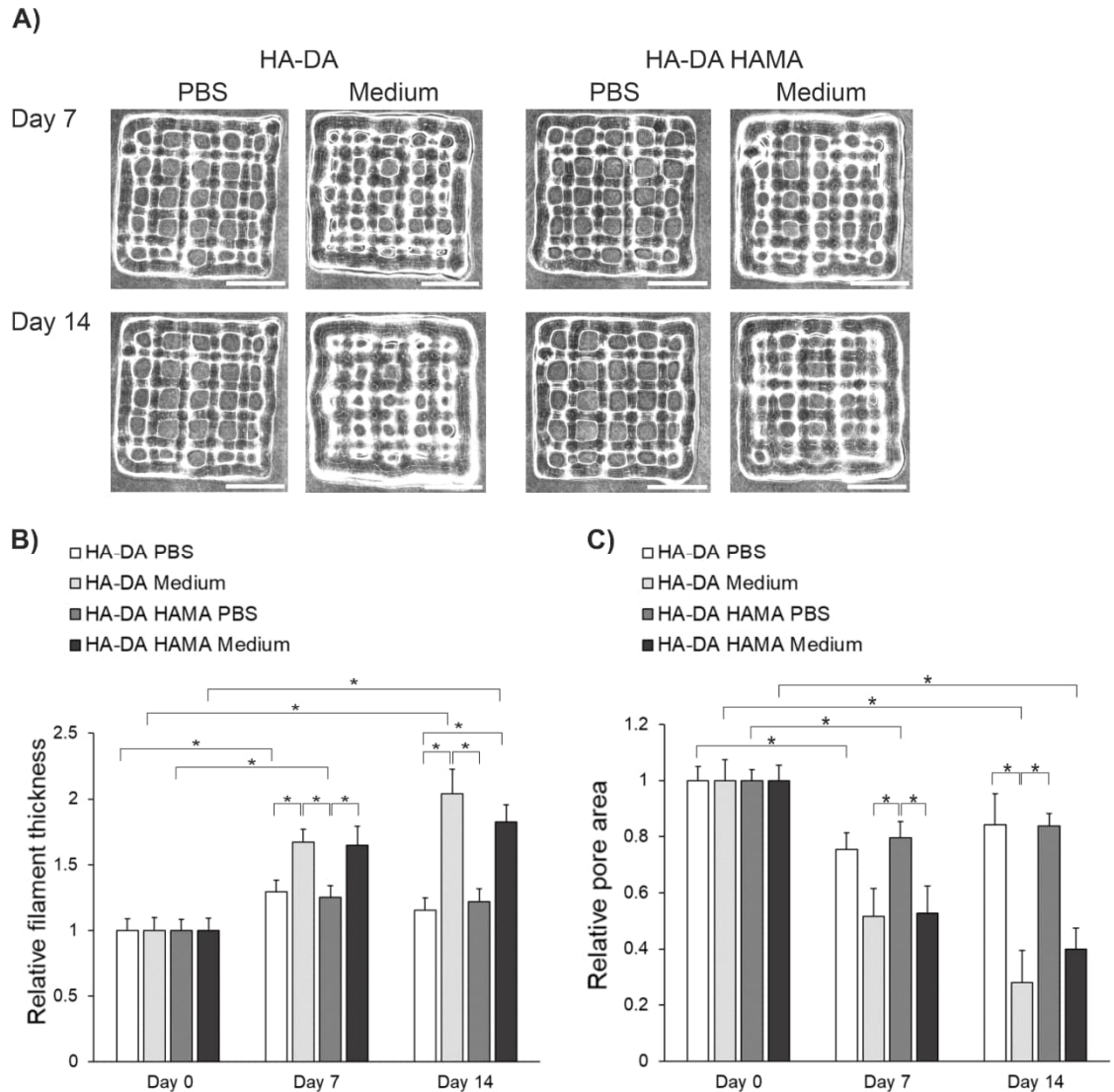


Figure 12. Shape fidelity of printed HA-DA and HA-DA HAMA grid structures during 14 days of incubation in PBS or LSC medium. Example images of printed HA-DA and HA-DA HAMA grid structures on day 7 and 14 of incubation. Scale bars 5 mm. (A). Relative filament thickness (B) and relative pore area (C) of HA-DA and HA-DA HAMA stromal bioinks during incubation. ($*p \leq 0.05$, $n=3$). All data is presented as mean values with \pm standard deviation.

10.2.3 Swelling behavior of bioprinted structures

To further assess the swelling behavior of the bioinks in different incubation conditions, printed cylindrical stromal structures were incubated in PBS or LSC medium. The swelling behavior of the printed structures was analyzed by calculating the change in weight % during 14 days of incubation (Figure 13). In LSC medium, the weight of the HA-DA structures increased on day 1, then slightly decreased on day 3, after which the weight continued to increase throughout the incubation period. In comparison, the HA-DA HAMA structures in LSC medium had a slight decrease in weight at day 1 after which the weight increased steadily until the end of the incubation period. The increase in

weight was slightly higher for the HA-DA structures than for the HA-DA HAMA structures in LSC medium. Instead, when incubated in PBS, the weight of both HA-DA and HA-DA HAMA cylinders decreased during the incubation period. The decrease in weight was more substantial for the HA-DA structures than for the HA-DA HAMA structures in PBS. Both, the greater swelling of the HA-DA structures in LSC medium as well as the larger decrease in weight of the HA-DA structures in PBS, is supported by the observations made in filament thickness and pore area during the 14-day incubation (Chapter 10.2.2).

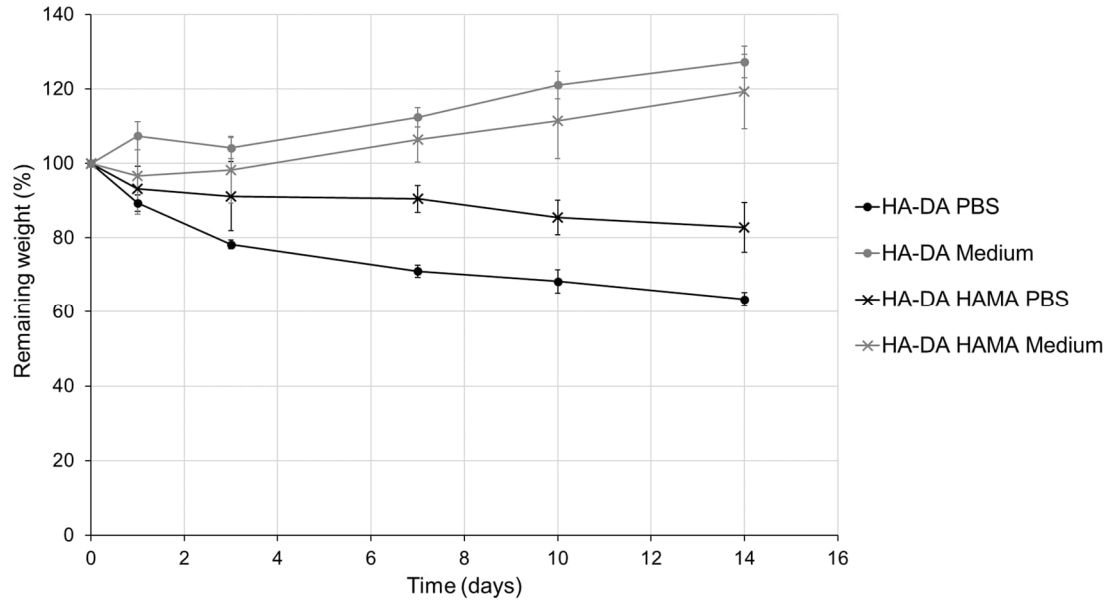


Figure 13. Remaining weight of printed cylindrical HA-DA and HA-DA HAMA stromal structures during incubation in PBS or LSC medium for 14 days. $N=4$ for HA-DA and $n=5$ for HA-DA HAMA in both conditions. Data is presented as mean values with \pm standard deviation.

10.2.4 Handling of bioprinted structures

Printed cylindrical HA-DA and HA-DA HAMA stromal structures were handled with spatula on day 7 and 14 after incubation in PBS or LSC medium (Figure 14). On day 7 after printing, all structures could be lifted onto a spatula. For both bioinks, structures in LSC medium were slightly more difficult to handle since the structures seemed to be softer than structures in PBS on day 7. When comparing the HA-DA and HA-DA HAMA structures, the HA-DA HAMA structures in PBS seemed more brittle and broke more easily during handling than HA-DA structures in PBS on day 7. Instead, HA-DA and HA-DA HAMA structures in LSC medium had similar handling on day 7. On day 14 after printing, all structures could be lifted onto spatula. For both bioinks, the difference in handling between structures in LSC medium and structures in PBS had grown as the structures in LSC medium were substantially softer than in PBS. HA-DA structures in LSC medium were very soft, elongated and lost their shape during handling whereas the HA-DA

HAMA structures in LSC medium kept their shape. As on day 7, the HA-DA HAMA structures in PBS seemed more brittle and broke more easily during handling than HA-DA structures in PBS on day 14.

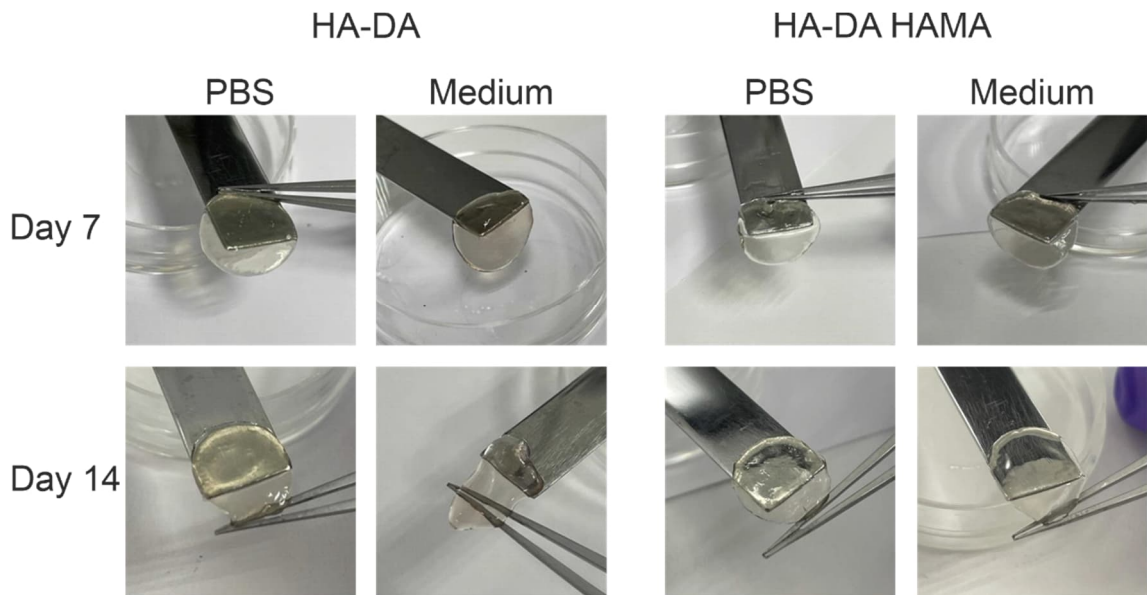


Figure 14. Handling of printed cylindrical HA-DA and HA-DA HAMA stromal structures with spatula. Structures incubated in LSC medium or PBS for 7 and 14 days.

10.2.5 Rheology of bioprinted structures

Cylindrical HA-DA and HA-DA HAMA stromal structures were incubated in PBS or LSC medium to assess the effect of bioink composition and incubation conditions on viscoelastic properties of the structures. Amplitude sweeps were performed for each condition on day 1 and 7 of incubation. The amplitude sweeps for HA-DA and HA-DA HAMA structures in PBS and LSC medium are presented for day 1 in Figure 15A and for day 7 in Figure 15B. The storage modulus was higher than the loss modulus in each condition in the linear viscoelastic region (LVER). This implies that the elastic behavior dominates over viscous behavior and that the structures are more solid than liquid. From the LVER, 1% strain was selected for frequency sweeps.

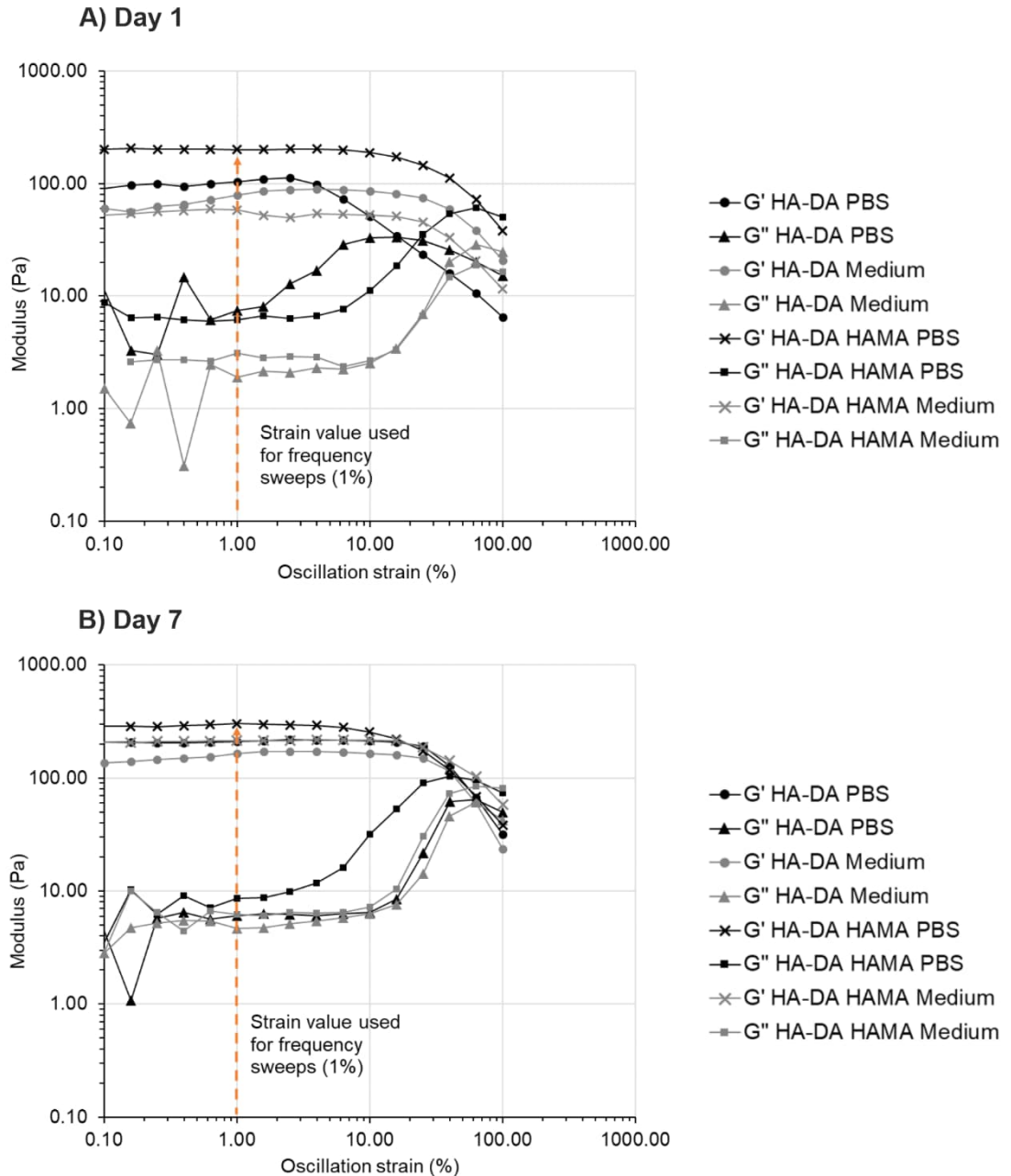


Figure 15. Amplitude sweeps with 1 Hz frequency for HA-DA and HA-DA HAMA stromal structures on day 1 (A) and 7 (B). Strain value chosen for frequency sweeps indicated with orange arrow. Storage modulus (G'), loss modulus (G''). $N=2$ for all HA-DA HAMA structures. $N=3$ for HA-DA structures in PBS on day 1 and in medium on day 1 and 7. $N=2$ for HA-DA structures in PBS on day 7. All data is presented as mean values.

Based on frequency sweeps, storage moduli at 1 Hz were compared (Figure 16). The storage moduli on day 1 and 7 for HA-DA structures were 162.02 ± 50.82 Pa and 163.46 ± 76.82 Pa in PBS, respectively, and 123.69 ± 24.24 Pa and 86.18 ± 24.35 Pa in LSC medium, respectively. Instead, the storage moduli on day 1 and 7 for HA-DA HAMA structures were 287.68 ± 59.29 Pa and 275.58 ± 94.85 Pa in PBS, respectively, and 279.05 ± 63.29 Pa and 76.57 ± 12.36 Pa in LSC medium, respectively.

On day 1, the storage moduli of HA-DA HAMA structures in LSC medium and PBS were significantly ($p < 0.05$) higher than the storage modulus of HA-DA structures in LSC medium indicating a more solid like appearance. Interestingly, on day 7, the storage modulus of HA-DA HAMA structures in LSC medium had decreased and there was no significant difference between the storage moduli of HA-DA HAMA and HA-DA structures in LSC medium. However, the storage modulus of HA-DA HAMA structures in PBS remained high on day 7 and was significantly ($p < 0.05$) higher than the storage moduli of HA-DA HAMA structures in LSC medium and HA-DA structures in LSC medium. Overall, the storage moduli of HA-DA structures remained relatively unchanged between day 1 and day 7 in both conditions whereas the storage modulus of HA-DA HAMA structures in LSC medium decreased between day 1 and 7 while HA-DA HAMA structures in PBS retained their storage moduli. This indicates that LSC medium has a notable effect especially on the HA-DA HAMA structures.

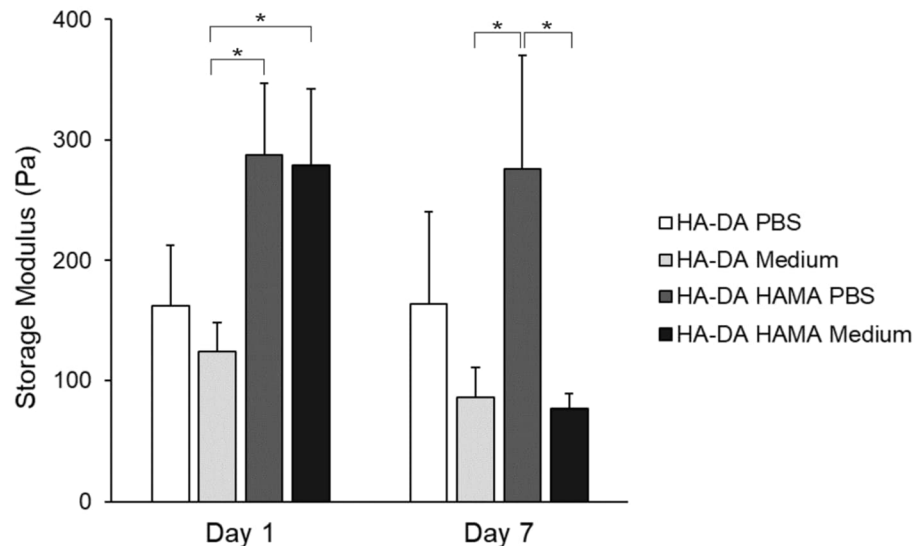


Figure 16. Storage moduli at 1 Hz from frequency sweeps for HA-DA and HA-DA HAMA stromal structures in PBS or LSC medium. $N=5$ for HA-DA medium and $n=4$ for HA-DA PBS, HA-DA HAMA medium and HA-DA HAMA PBS on day 1. $N=4$ for HA-DA medium and HA-DA PBS, $n=3$ for HA-DA HAMA medium and $n=5$ for HA-DA HAMA PBS on day 7. Data is presented as mean values with \pm standard deviation ($p < 0.05$).

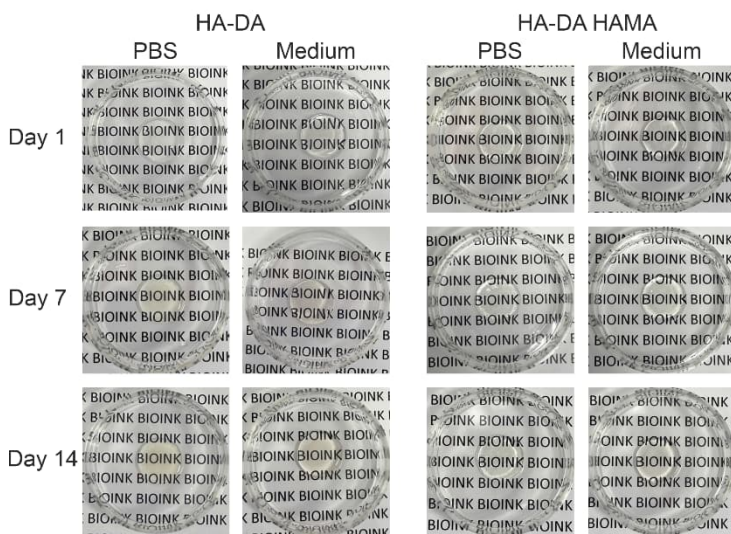
10.2.6 Transparency

Transparency is required for the correct function of the cornea (Fuest et al., 2020). Therefore, transparency of printed acellular HA-DA and HA-DA HAMA stromal structures in PBS and LSC medium were analyzed visually on day 1, 7 and 14 after printing (Figure 17A). Also, transparency of printed cell-laden structures was analyzed visually on day 1 and 7 after printing (Figure 17B).

In acellular structures, printed text was clearly visible through the structures in all timepoints. There was no major difference between transparency when comparing HA-DA and HA-DA HAMA structures in different incubation conditions on day 1, 7 and 14. However, during the incubation period HA-DA structures in PBS turned slightly yellow while remaining transparent on day 14. This change in color could not be observed as clearly in HA-DA structures in LSC medium most likely due to the pink color of the LSC medium also changing the color of the printed structures. Instead, in HA-DA HAMA structures in PBS, no clear change in color could be observed. In HA-DA HAMA structures in LSC medium, some change in color could be observed most likely due to the pink color of the LSC medium.

Also, in cell-laden structures, printed text was clearly visible through the structures in all timepoints. As with acellular structures, there was no major difference between transparency when comparing cell-laden HA-DA and HA-DA HAMA structures. Similarly, to acellular structures, the cell-laden HA-DA structures had turned slightly yellow on day 7 whereas this could not be observed to HA-DA HAMA structures.

A) Acellular structures



B) Cell-laden structures

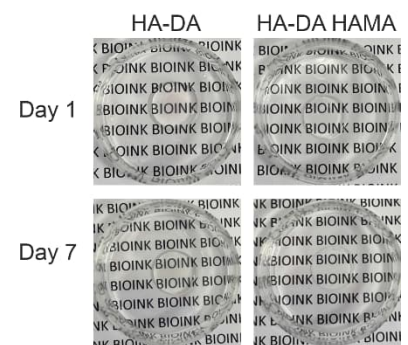


Figure 17. Visual transparency of acellular (A) and cell-laden (B) HA-DA and HA-DA HAMA stromal structures. Acellular structures have been incubated in PBS or LSC medium.

In addition to visual transparency, the transparency of printed acellular cylindrical stromal structures was evaluated by measuring the light absorbance of printed structures in the visible light spectrum (400 – 700 nm) after 1 day of incubation in LSC medium. From the measured absorbance values, light transmittance was calculated (Figure 18). The transparency of the printed structures was compared to the transparency of PBS as it is the major solvent in the bioink. PBS transmitted most of the light in the visible light spectrum of 400 – 700 nm where $89.6 \pm 0.1 - 91.3 \pm 0.2$ % transmittance was measured (Figure

18). Printed structures had lower light transmittance than PBS but demonstrated excellent transparency almost throughout the visible light spectrum as the printed structures had mostly transmittance values of over 75% (Ventura et al., 2005). HA-DA HAMA structures had higher transparency than HA-DA structures (Figure 18). The light transmittance for HA-DA HAMA and HA-DA structures was $83.7 \pm 1.1 - 89.9 \pm 0.5 \%$ and $74.4 \pm 4.2 - 86.4 \pm 1.5 \%$, respectively, in the visible light spectrum.

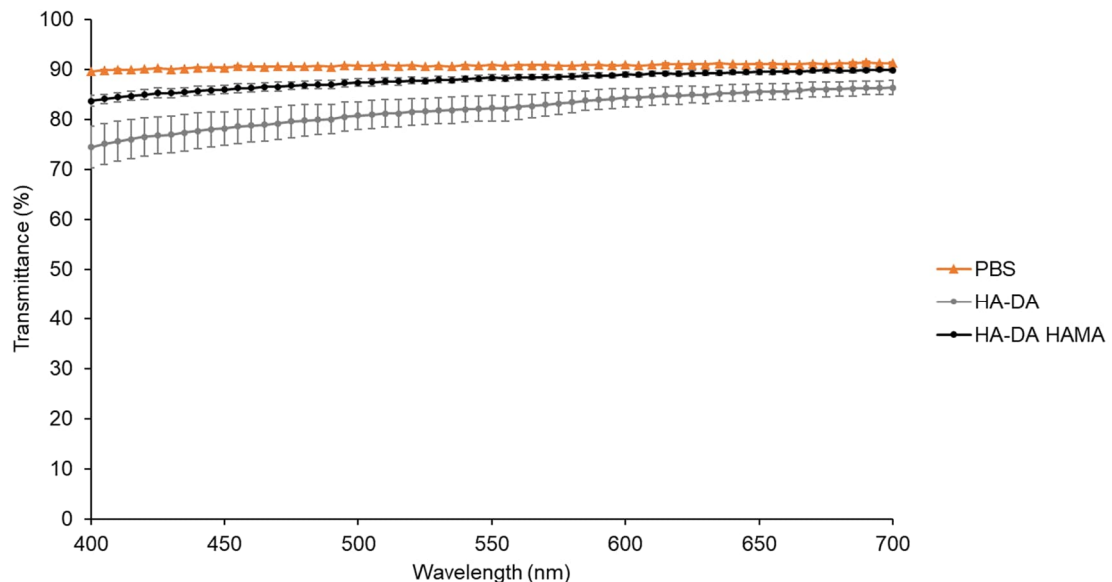


Figure 18. Light transmittance of printed HA-DA and HA-DA HAMA cylindrical stromal structures at different wavelengths of visible light spectrum compared with control (PBS). Data is presented as mean values with \pm standard deviation.

10.3 Cytocompatibility of stromal bioinks

Next, the cytocompatibility of both HA-DA and HA-DA HAMA stromal bioink was assessed with hASC-CSKs by printing cylindrical stromal structures. For the photocross-linkable HA-DA HAMA stromal bioink, the effect of UV exposure and exposure time on the cytocompatibility was also examined.

10.3.1 Live/Dead

Live/Dead assay was performed for hASC-CSKs printed in HA-DA stromal structures on day 1 to determine cell viability after printing and on day 7 to examine the cell viability during culture. Unfortunately, on day 1 the assay was performed incorrectly, and no Live/Dead results were obtained for hASC-CSKs printed in HA-DA structures on day 1. However, based on phase contrast images, already on day 1 many cells started to form

extensions indicating viable cells (Figure 19). On day 7, the viability of hASC-CSKs remained high, and cells started forming longer extensions and had elongated cell morphology (Figure 19).

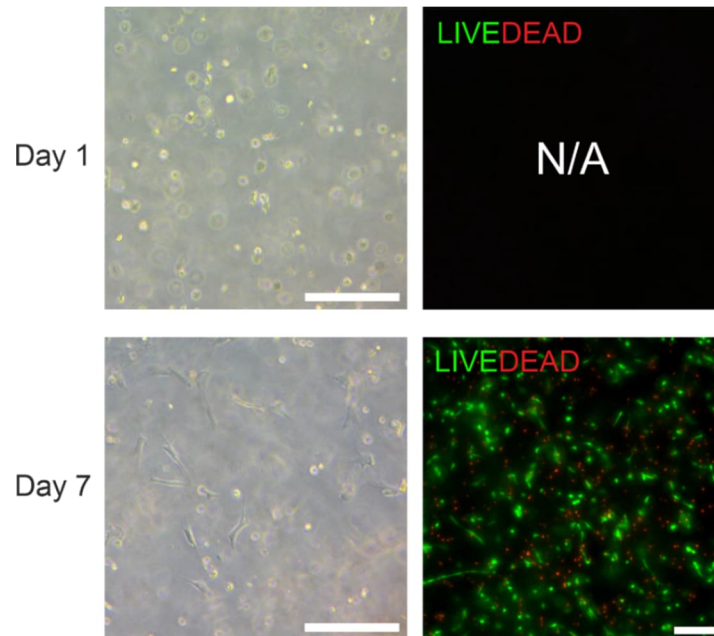


Figure 19. Phase contrast images of hASC-CSKs printed in HA-DA stromal structures demonstrating cell morphology on day 1 and 7. Viability of hASC-CSKs of respective sample day 7 after printing. Live cells (green), dead cells (red). Scale bars 200 μ m.

To assess the viability of hASC-CSKs in the printed HA-DA HAMA stromal structures and the effect of UV, Live/Dead assay was performed on day 1 and day 7 after printing (Figure 20). On day 1, when comparing the sample without UV exposure to the samples with UV exposure, the number of dead cells was slightly higher in samples with UV exposure. This indicates that the UV may have some effect on cell survival. Also on day 1, the number of cells expressing bright green color was higher in samples without UV exposure when compared to samples exposed to UV for 30 or 60 s (images taken with same settings). Moreover, in samples exposed to UV, all cells had rounded morphology on day 1 whereas few cells in samples without UV exposure had started to form extensions on day 1. Notably, no significant effects on cell viability were detected when increasing UV exposure time from 30 to 60 s. With both 30 and 60 s UV exposure times, the number of dead cells was already high on day 1 and slightly increased on day 7. Likewise, for samples without UV exposure, the number of dead cells slightly increased from day 1 to day 7. When comparing the cell morphologies on day 7, the cells in samples exposed to UV retained their rounded morphology whereas some cells in samples without UV exposure exhibited small extensions.

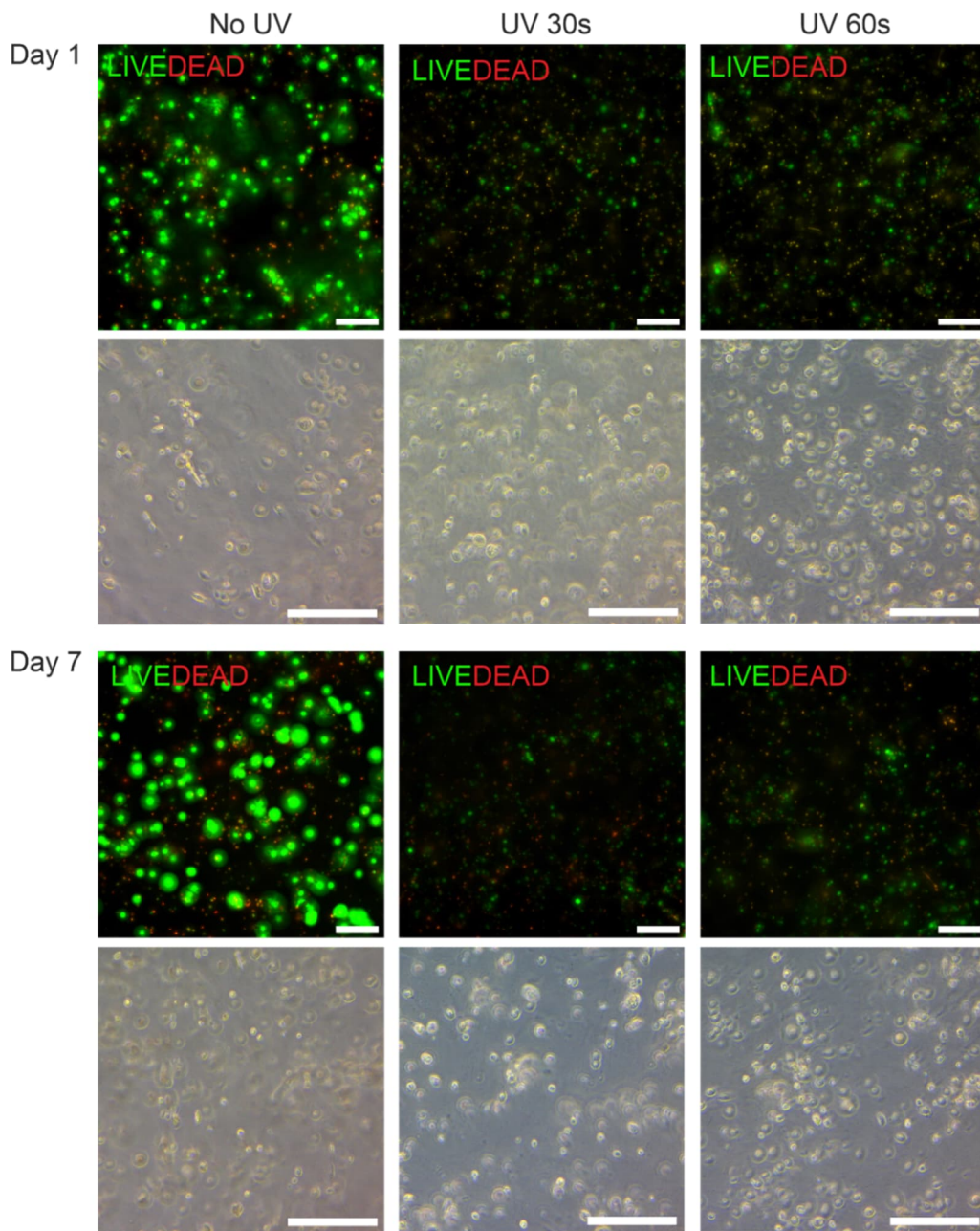


Figure 20. The effect of UV exposure on hASC-CSK viability in printed HA-DA HAMA stromal structures on day 1 and day 7 after printing, and phase contrast image of respective sample to demonstrate cell morphology. Live cells (green), dead cells (red). Scale bars 200 μm .

10.3.2 Immunofluorescence staining

Cell morphology, tissue formation after printing, and expression of cornea stroma specific markers were visualized by IF staining HA-DA and HA-DA HAMA cylindrical stromal structures containing hASC-CSKs. With HA-DA HAMA structures, the effect of different UV exposure times was also investigated.

Elongated morphology of hASC-CSKs was clearly observed by phalloidin stained actin filaments in HA-DA structures on day 7 (Figure 21) indicating that hASC-CSKs can migrate in the structure. Additionally, gap junction protein Cx43 was expressed as bright dots between cells indicating hASC-CSKs forming cell-cell interactions. Moreover, hASC-CSKs were observed growing on top of each other possibly within printed layers in the orthogonal visualization. At the end of culture on day 21, hASC-CSKs had grown in size and continued to form cellular networks (Figure 21) indicating that the cells are capable of tissue formation in the HA-DA stromal structures.

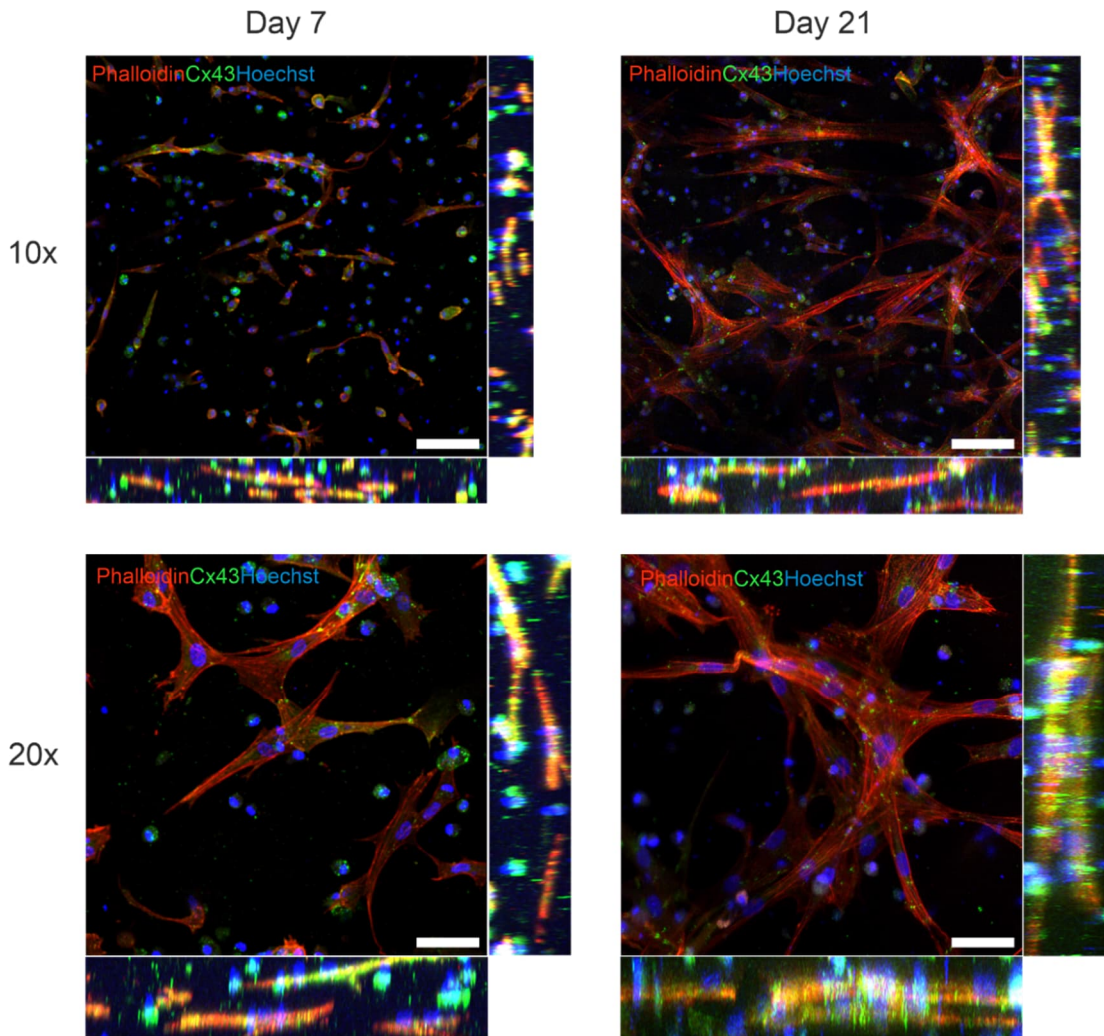


Figure 21. hASC-CSKs printed with HA-DA stromal bioink into cylindrical stromal structures on day 7 and 21. IF staining with nuclei stain Hoechst (blue), gap junction protein Cx43 (green) and Phalloidin (red). Scale bar for 10X 100 μm and 20X 50 μm .

Instead, in HA-DA HAMA stromal structures, hASC-CSKs had rounded morphology with both UV exposure times and no clear difference between UV exposure times was observed (Figure 22A and Figure 22B). Moreover, no changes in cell morphology were observed for either UV exposure time by the end of culture on day 14 for UV exposure 30 s (Figure 22A) and on day 21 for UV exposure 60 s (Figure 22B). These results show

that the hASC-CSKs retain rounded morphology in HA-DA HAMA stromal structures and therefore are not able to start tissue formation.

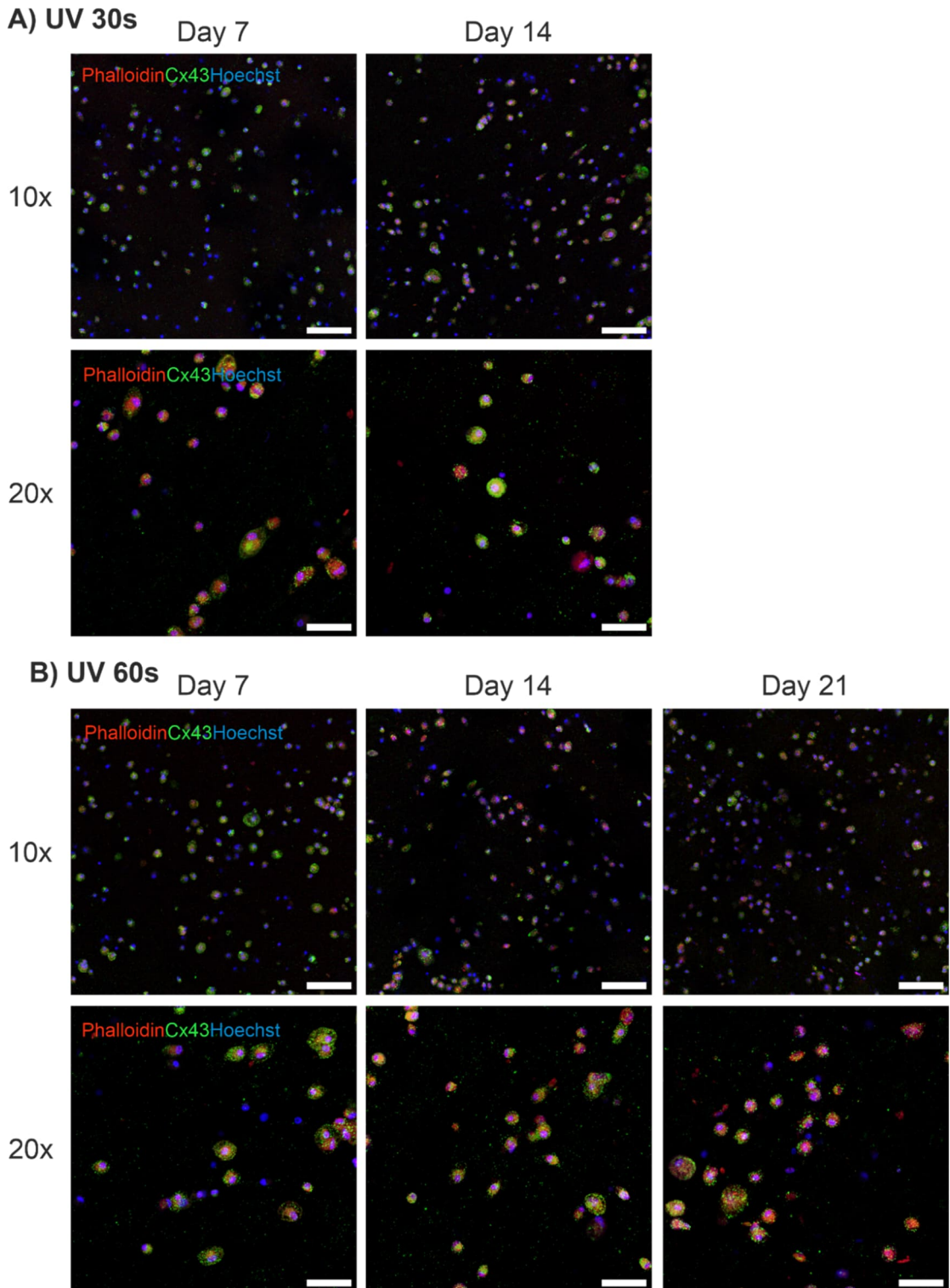


Figure 22. hASC-CSKs printed with HA-DA HAMA stromal bioink into cylindrical stromal structures with 30 s (A) and 60 s (B) UV exposure time. IF staining with nuclei stain Hoechst (blue), gap junction protein Cx43 (green) and Phalloidin (red). Scale bar for 10X 100 μm and 20X 50 μm.

The expression of Col I was studied as it is the major structural protein of the corneal stroma (España and Birk, 2020; Meek and Knupp, 2015). In native corneal ECM it is arranged as highly organized fibrils and is produced by hCSKs (S. Chen et al., 2015; Meek and Knupp, 2015). On day 7 in HA-DA stromal structures, some intracellular Col I expression was observed (Figure 23). In addition, extracellularly stained Col I was observed as haze around the cells on day 7 and did not have fiber-like appearance (Figure 23). On day 14 in HA-DA stromal structures, intracellular Col I expression was increased and extracellular Col I expression appears more fiber-like (Figure 23). On day 21 in HA-DA stromal structures, the intracellular Col I expression had decreased from day 14 whereas the extracellular Col I expression is clearly fiber-like (Figure 23).

The cornea stroma marker lumican is a SLRP and one of the main proteoglycans of the corneal stroma (Carlson et al., 2005). Lumican was expressed intracellularly by hASC-CSKs in HA-DA stromal structures on day 7 (Figure 23). On day 14, lumican was mostly expressed intracellularly, but some extracellular expression with fibrillar organization could be observed in the HA-DA stromal structures (Figure 23). The extracellular expression of lumican with fibrillar organization was increased on day 21 (Figure 23).

In HA-DA HAMA stromal structures, some possible Col I intracellular expression was observed on day 14 with both UV 30 and 60 s exposure times (Figure 24A). Extracellular Col I was observed as haze around the cells in the HA-DA HAMA stromal structures on day 14 (Figure 24A) which was similar to observations with HA-DA stromal structures on day 7. On day 21 in the HA-DA HAMA stromal structures, the Col I expression inside the cells remains the same as on day 14 (Figure 24B). Instead, based on the extracellular Col I expression on day 21 in HA-DA HAMA stromal structures it seemed like Col I had organized into randomly winding bundles around cells (Figure 24B). This extracellular Col I in HA-DA HAMA stromal structures differed significantly from the fiber-like appearance extending from cells observed in the HA-DA stromal structures on day 21.

In HA-DA HAMA stromal structures, some possible lumican expression was observed on day 14 (Figure 24A) as well as on day 21 (Figure 24B). The expression pattern did not change between day 14 and 21. In addition, on day 14 no differences between UV exposure times were observed (Figure 24A).

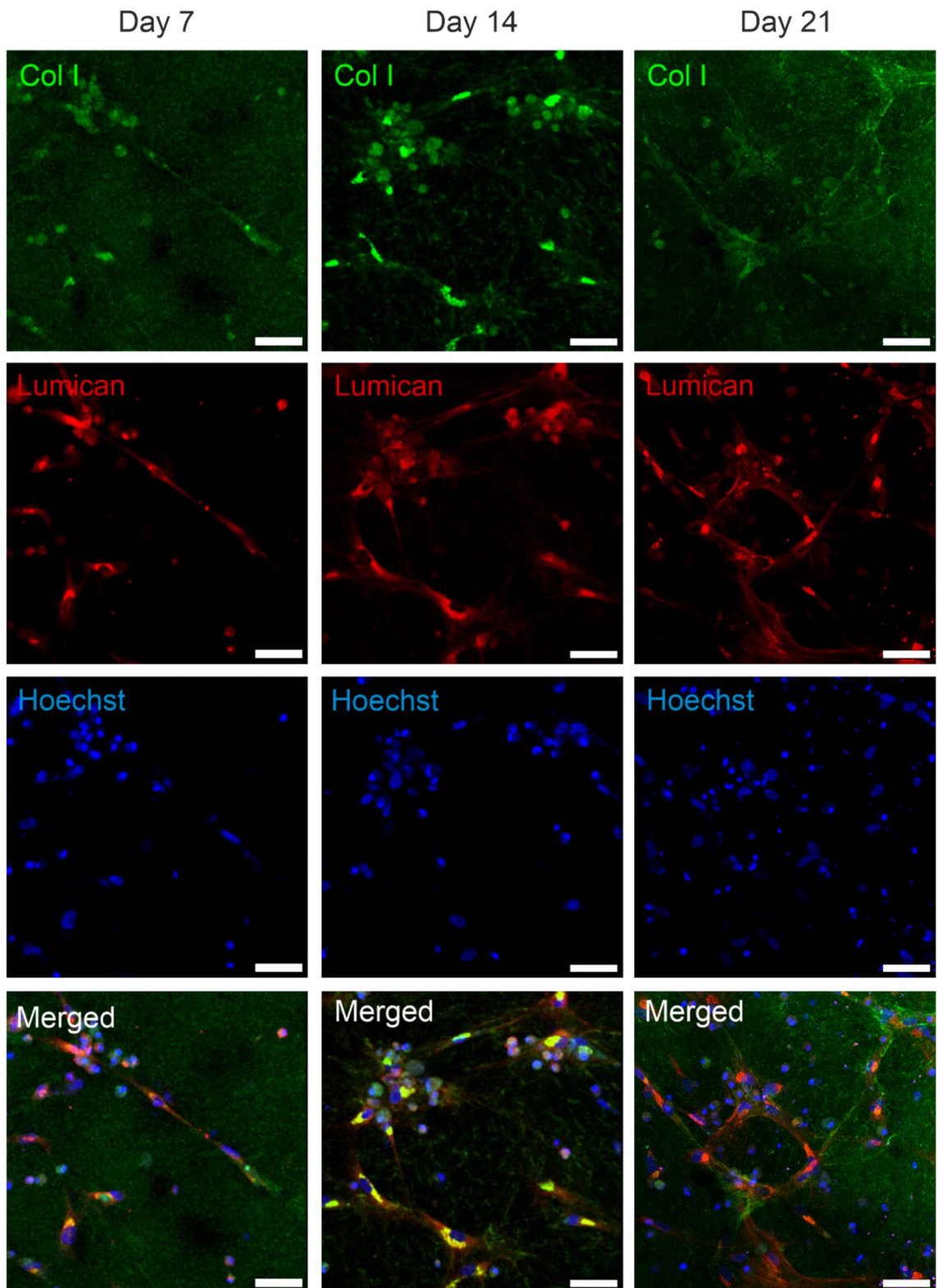


Figure 23. hASC-CSKs printed with HA-DA stromal bioink into cylindrical stromal structures. IF staining with Col I (green), Lumican (red) and nuclei stain Hoechst (blue). Scale bar 50 μ m.

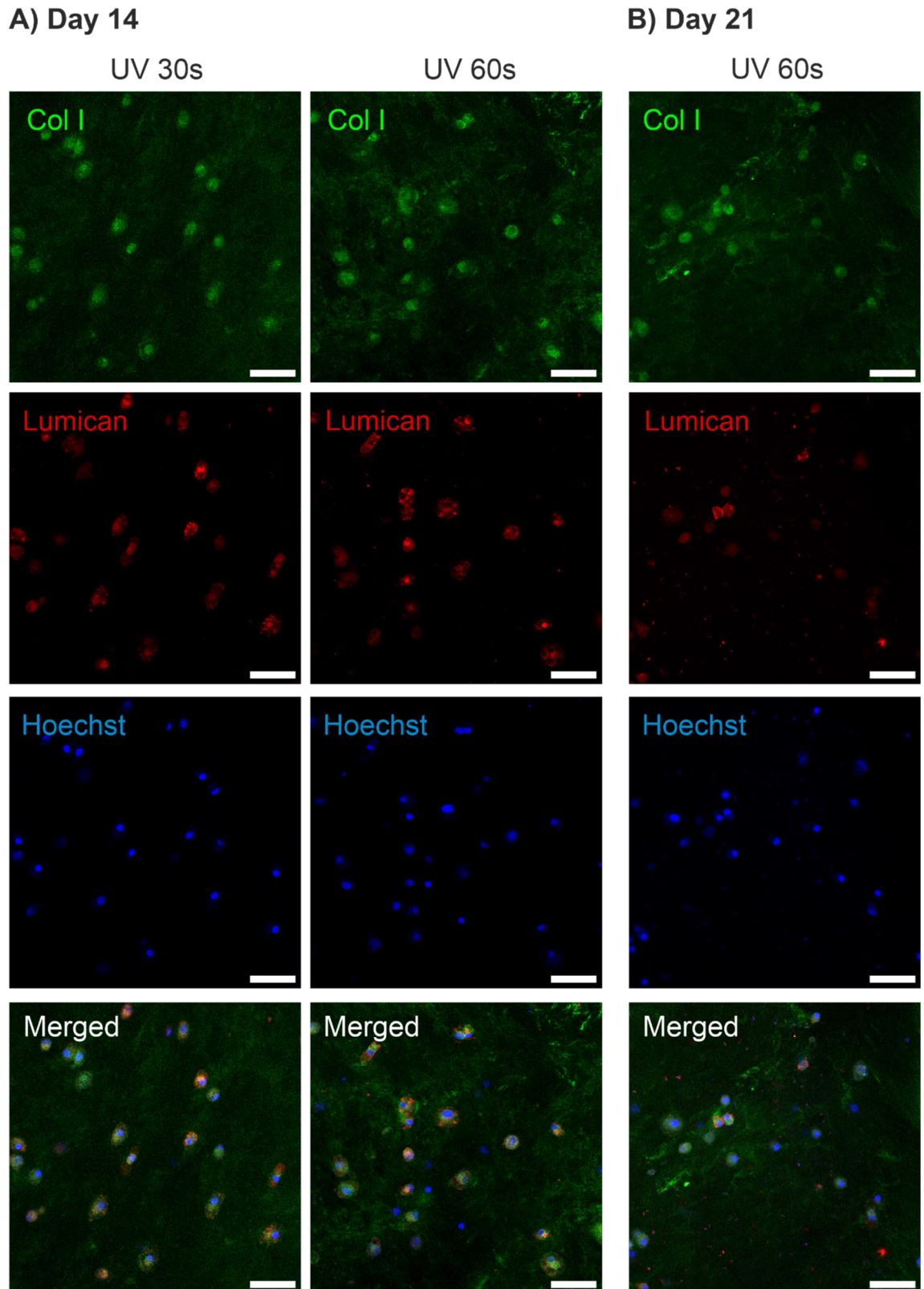


Figure 24. *hASC-CSKs printed with HA-DA HAMA stromal bioink into cylindrical stromal structures with 30 s and 60 s UV exposure time on day 14 (A) and with 60 s UV exposure time on day 21 (B). IF staining with Col I (green), Lumican (red) and nuclei stain Hoechst (blue). Scale bar 50 μ m.*

10.3.3 Stability of cell-laden stromal structures in LSC medium

All the cell-laden stromal structures used to study cytocompatibility in Chapter 10.3.1 and 10.3.2 were cultured in KDM. Additionally, some cell-laden stromal structures were cultured in LSC medium to assess the stability of these cell-laden structures in the co-culture condition.

On day 1 of culture in LSC medium, hASC-CSKs in HA-DA stromal structures started to form extensions (Figure 25A) indicating that the cells have survived printing and one day of culture in LSC medium. On day 1 and 2 of culture, the structure was still stable and attached to the bottom of the culture dish. However, on day 5 of culture the cell-laden structures had completely broken down as only small traces of the HA-DA structures as well as few cells can be seen at the bottom of the culture dish (Figure 25A).

Instead, cell-laden HA-DA HAMA stromal structures with 30 and 60 s UV exposure time were cultured in LSC medium for 14 days. Even though the structures remained stable until day 14, on day 6 they detached from the bottom of the culture dish. Similarly, to cell-laden HA-DA HAMA structures in KDM, the hASC-CSKs retained round morphology until the end of culture on day 14 (Figure 25B). Live/Dead staining was performed on day 14 for cell-laden HA-DA HAMA structures with 30 and 60 s UV exposure time (Figure 25B) and indicated that most of the cells in the HA-DA HAMA structures were dead on day 14.

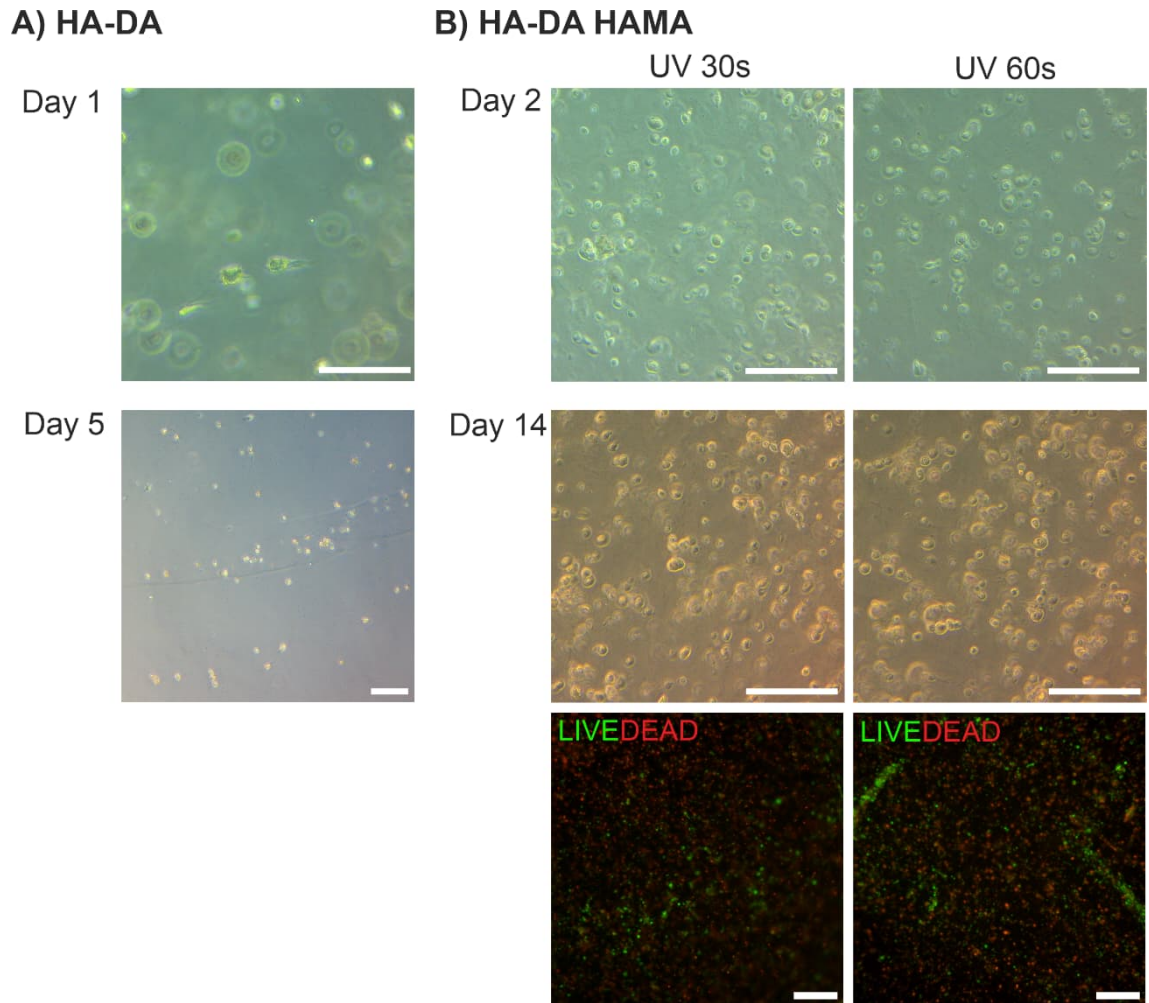


Figure 25. Cell-laden stromal structures cultured in LSC medium. Phase contrast images of hASC-CSKs printed in HA-DA stromal structures on day 1 and 5. Scale bars 100 μm for day 1 and 200 μm for day 5. (A). Phase contrast images of hASC-CSKs printed in HA-DA HAMA stromal structures with 30 s and 60 s UV exposure time on day 2 and 14. Scale bars 200 μm . Viability of hASC-CSKs of respective sample on day 14 after printing. Live cells (green), dead cells (red). Scale bars 400 μm . (B).

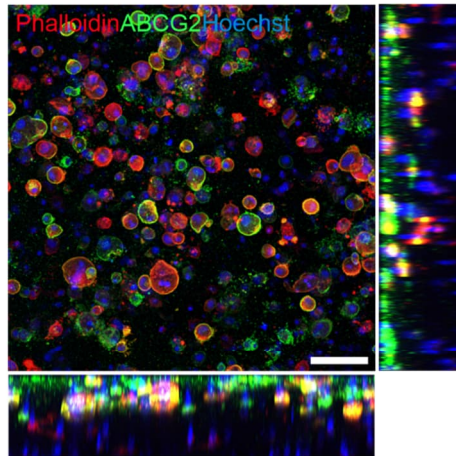
10.4 Human cornea mimicking structures with stroma and epithelium

Finally, based on the comparison of HA-DA and HA-DA HAMA stromal bioinks, cornea mimicking structures with stroma and epithelium were printed. Since hASC-CSKs retained rounded morphology in HA-DA HAMA stromal structures (Figure 22) and because HA-DA cell-laden stromal structures had completely broken down on day 5 of culture in LSC medium (Figure 25A), a HA-DA stromal bioink with an increased concentration of crosslinking components was used. Cornea mimicking structures with stroma and epithelium, were successfully created by first printing the stromal layer containing hASC-CSKs. On top, ABCG2 enriched hPSC-LSCs were printed as epithelial layer. These structures were cultured in two different co-culture conditions.

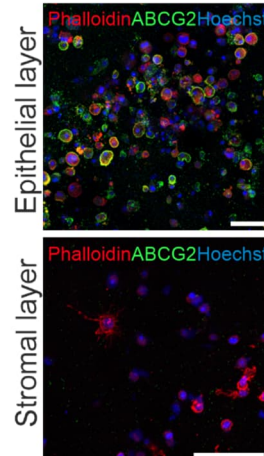
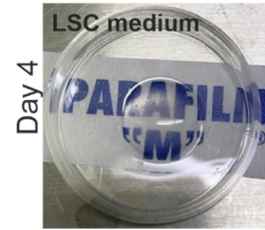
After 4 days of culture, all structures were stable and did not show signs of collapsing due to cell proliferation. Moreover, structures cultured in LSC medium showed good visual transparency (Figure 26B). The hPSC-LSCs expressed ABCG2, and clear separation of the epithelial and stromal layer could be observed in the structure in LSC medium on day 4 (Figure 26A). However, hASC-CSKs had mostly rounded morphology in the structure cultured in LSC medium (Figure 26A).

On day 7 of culture, structures in LSC medium had considerably swelled compared to day 4 (Figure 26D) whereas the structure in KDM+LSC medium had retained its shape (Figure 26F). In both co-culture conditions, hPSC-LSCs expressed ABCG2, and clear separation of the epithelial and stromal layer could be observed on day 7 (Figure 26C and E). However, the hPSC-LSCs were mostly separately dispersed in the epithelial layer and did not form stratified epithelium. In structures cultured in LSC medium, the hPSC-LSC amount had decreased when compared to day 4, and hASC-CSKs maintained rounded morphology (Figure 26C). Instead, in the structure cultured in KDM+LSC medium, elongated morphology of hASC-CSKs was clearly observed by phalloidin stained actin filaments and the amount of hPSC-LSCs was higher (Figure 26E). These results indicate that the KDM+LSC medium would be a more suitable co-culture condition for cornea mimicking structures with stroma and epithelium.

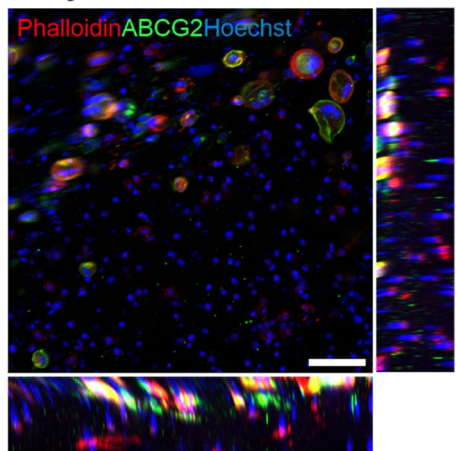
A) Day 4 LSC medium



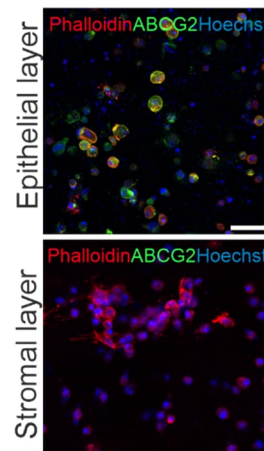
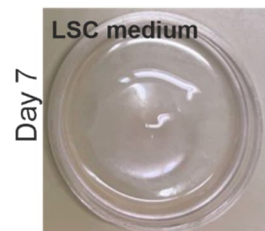
B)



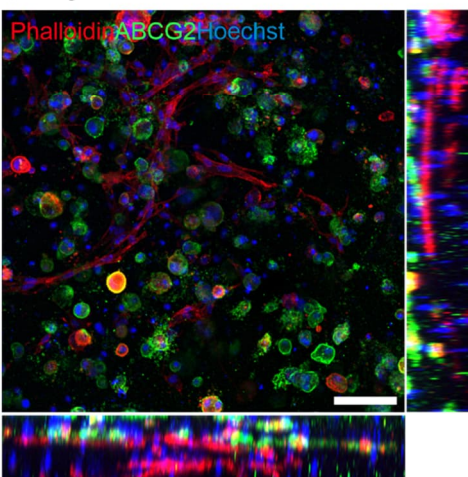
C) Day 7 LSC medium



D)



E) Day 7 KDM+LSC medium



F)

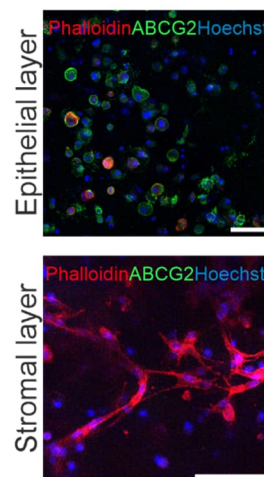
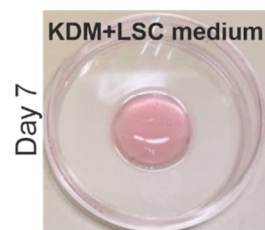


Figure 26. Human cornea mimicking structures with stroma and epithelium. IF staining with ABCG2 (green), Phalloidin (red) and nuclei stain Hoechst (blue) for orthogonal visualization of each structure demonstrating the separate epithelial and stromal layer as well as images from stromal and epithelial layer separately. Structures on day 4 (A) and day 7 (C) of culture in LSC medium as well as their visual appearance on day 4 (B) and day 7 (D). Structure on day 7 of culture in KDM+LSC medium (E) and its visual appearance (F). Scale bars 100 μ m.

11. DISCUSSION

3D bioprinting has emerged as a promising approach to produce corneal structures to alleviate the shortage of donor corneas needed for corneal transplantation (Balters and Reichl, 2023). When corneal structures with multiple layers of the cornea are 3D bioprinted, different cell types must be co-cultured following the 3D bioprinting process. While hPSC-LSCs show promise as the cell source for the epithelial layer (Hongisto et al., 2017; Mikhailova et al., 2014), they demand a complex LSC medium during cell culture (CELLnTEC, 2023). In this medium, the HA-DA stromal bioink has not previously maintained its structural stability, thus creating a challenge for bioprinting cornea mimicking structures with stroma and epithelium using this bioink. This thesis aimed to enhance the stiffness and stability of the HA-DA stromal bioink to enable co-culturing of 3D bioprinted cornea mimicking structures with stroma and epithelium in the LSC medium co-culture condition. To enhance the stiffness and stability of the HA-DA stromal bioink, the composition was modified by incorporating a HAMA component to create a photocrosslinkable HA-DA HAMA stromal bioink.

To date, HAMA has not been previously incorporated into corneal bioinks (Table 1). Instead, GelMA has mainly been used to create photocrosslinkable bioinks for SLA, DLP and extrusion-based bioprinting of corneal structures (He et al., 2022; Kilic Bektas and Hasirci, 2020; Mahdavi et al., 2020a; Zhang et al., 2023; Zhong et al., 2021). However, in bone and cartilage bioprinting HAMA has been widely used as a bioink component (Ghorbani et al., 2023) to increase stiffness (Kesti et al., 2015; Müller et al., 2015; Poldervaart et al., 2017; Shopperly et al., 2022) and long-term stability (Kesti et al., 2015; Poldervaart et al., 2017). Due to these previous observations, the incorporation of a HAMA component into the HA-DA stromal bioink to improve stiffness and stability was investigated. When the HA-DA stromal bioink is printed, the crosslinking components HA-ALD and HA-DA-CDH undergo hydrazone crosslinking creating a HA-based polymer network into the printed structure. Additionally, gelation of the Col I bioink component occurs (OptiCol™, 2023). Since the HA-DA HAMA stromal bioink has HAMA as an additional crosslinkable component, the bioprinted structures have a HAMA polymer network after photocrosslinking in addition to the HA-based polymer network and Col I. Therefore, the HA-DA HAMA stromal bioink is a hydrogel blend from which structures with complementary polymer networks can be created, and it was hypothesized that this HAMA polymer network would enhance the stiffness and stability of the bioprinted struc-

tures. As the formation of the HA-based polymer network is based on hydrazone crosslinking and the formation of the HAMA polymer network is based on photocrosslinking, the HA-DA HAMA stromal bioink uses a combination of different crosslinking mechanisms. To improve the biofunctionality or enhance the mechanical stability of bioinks, combinations of crosslinking mechanisms have been used previously in different kinds of multicomponent bioinks (Cui et al., 2020).

Next, the results for printability, shape fidelity, viscosity, swelling behavior, handling, mechanical properties, and transparency are discussed and compared between the HA-DA and HA-DA HAMA stromal bioinks. Also, the effect of LSC medium on these bioinks is examined following which the cytocompatibility of both bioinks with hASC-CSKs is discussed. Finally, this chapter is concluded with a discussion of and future perspectives for 3D bioprinting human cornea mimicking structures with stroma and epithelium.

11.1 Characterization of stromal bioinks

Before assessing the effect of the HAMA component in the HA-DA stromal bioink, the HA-DA HAMA stromal bioink composition was optimized without cells to find a composition with suitable printability, shape fidelity, and handling properties. These were characterized since printability and shape fidelity are important requirements of bioinks (Schwab et al., 2020) and the handling of printed structures gives indications about their stiffness and stability. Replacing the unmodified HA in the original HA-DA stromal bioink with HAMA created a HA-DA HAMA stromal bioink with good printability as well as good shape fidelity immediately after printing. When HA-DA HAMA stromal structures were exposed to UV immediately after printing, they were stable during incubation in the LSC medium co-culture condition and kept their original shape well during handling.

After optimizing the HA-DA HAMA stromal bioink, it was compared to the original HA-DA stromal bioink. Both the HA-DA and HA-DA HAMA stromal bioink had good printability and good shape fidelity immediately after printing supported by the pore factor being close to one for both bioinks. As the printing pressures did not significantly differ between the bioinks, same printing parameters were used. With these parameters, the HA-DA stromal bioink had greater filament thickness than the HA-DA HAMA stromal bioink. This could be due to the optimal printing pressure of the HA-DA stromal bioink being slightly lower than that of the HA-DA HAMA stromal bioink. In viscosity measurements, the peak viscosities did not significantly differ between HA-DA and HA-DA HAMA stromal bioink and the peak viscosity of HA-DA stromal bioink was only slightly lower. Therefore, the viscosity measurements support the observation of only a slight difference in printing pressures. Viscosity measurements also confirmed that both bioinks were shear-thinning

as the viscosities of the bioinks decreased when shear rate was increased. Based on this comparison, the HAMA component did not affect the printability or shear-thinning behavior of the HA-DA stromal bioink. Shear-thinning is an important characteristic of bioinks since it reduces unnecessary shear stresses towards cells in extrusion-based bioprinting and thus prevents cell death (Schwab et al., 2020). Also, shear-thinning allows the bioink to immediately recover and solidify after extrusion to provide shape fidelity since as the shear rate drops viscosity increases (Cui et al., 2020; Karvinen and Kellomäki, 2023; Schwab et al., 2020). Therefore, the observed shear-thinning behavior of the bioinks supports the good printability reported. These results are in line with previous viscosity measurements conducted by Mörö et al. (2022) for the HA-DA stromal bioink where it exhibited shear-thinning behavior.

Shape fidelity of bioprinted structures should be maintained after bioprinting for a desired time such as over the period of cell culture (Karvinen and Kellomäki, 2023). The swelling behavior of hydrogels, including those used in bioinks, is known to be influenced by environmental conditions (Ahmed, 2015). Consequently, the swelling behavior of the bioink affects shape fidelity (Karvinen and Kellomäki, 2023). Therefore, both stromal bioinks were characterized in two different incubation conditions: the LSC medium co-culture condition and PBS. First, the shape fidelity of printed grid structures was analyzed. When compared to the grids on day 0 before incubation, filament swelling and consequent decrease of pore area in the grids was observed in both incubation conditions visually and by analyzing the filament thickness as well as pore area. The swelling is due to the nature of the bioinks since the hydrogels in both bioinks swell upon immersion into liquid (Ahmed, 2015; Mantha et al., 2019). Over the incubation period, the swelling of the grid structures was greater in LSC medium than PBS for both bioinks indicating better shape fidelity and improved stability of the bioinks in PBS. The greater swelling in LSC medium can be caused by the inflow of medium components such as proteins. Different swelling behavior for HA-based hydrogel structures incubated in medium and PBS has also been previously reported by Koivusalo et al. (2019). They attributed the greater swelling in medium to the dynamic nature of the hydrazone bond and suggested that the bond may interact with proteins present in the medium (Koivusalo et al., 2019). The dynamic nature of the hydrazone bond means that the hydrazone bond is a dynamic covalent bond that has significantly higher strengths than physical bonds while still being reversible and having the ability to rearrange to permit cell spreading (Wang et al., 2018). Since the crosslinking of the HA-based hydrogels used by Koivusalo et al. (2019) is based on the same hydrazone crosslinking of HA-ALD and HA-DA-CDH used for the HA-DA and HA-DA HAMA stromal bioinks of this thesis, the greater swelling observed here in medium

could be due to the hydrazone bond interacting with proteins of the LSC medium. However, this is only one possible factor influencing swelling, and it should be noted that the bioinks of this thesis included other components in addition to HA-ALD and HA-DA-CDH whereas the HA-based hydrogels used by Koivusalo et al. (2019) were composed of only HA-ALD and HA-DA-CDH.

Comparison of the two bioinks in LSC medium revealed that on day 7 no significant difference in filament thicknesses between the bioinks occurred indicating similar shape fidelity on day 7. However, on day 14 of incubation, the observed increase in filament thickness and decrease in pore area were slightly smaller for the HA-DA HAMA stromal bioink implying lower swelling, better shape fidelity, and improved stability of the HA-DA HAMA stromal bioink in LSC medium. These findings are supported by the handling and swelling behavior of the printed stromal structures. There were no significant differences in handling on day 7 but on day 14 HA-DA stromal structures were considerably softer than HA-DA HAMA stromal structures losing their shape during handling. Moreover, the weight of both HA-DA and HA-DA HAMA stromal structures increased during incubation in LSC medium, and this increase was slightly smaller for HA-DA HAMA stromal structures. These results indicate that the addition of the HAMA component into the HA-DA stromal bioink slightly improves the stability of the bioink in LSC medium as filament swelling is reduced, handling is improved, and weight increase due to swelling is smaller. The improved stability could be due to the formation of the HAMA polymer network into the bioprinted structures after photocrosslinking and that this photocrosslinked HAMA polymer network decreases the swelling of the HA-DA HAMA structures. This would be in line with previous results where photocrosslinked HAMA reduced swelling of dopamine-grafted HA hydrogels (Nejati and Mongeau, 2023). The reduced swelling due to HAMA was attributed to the hydrophobic nature of methacrylate groups and to the photocrosslinking between the methacrylate groups (Nejati and Mongeau, 2023) which could also explain the observations made here.

Interestingly, the results for filament swelling, handling, and weight change of the bioinks in PBS differed significantly from those obtained for LSC medium. Instead of filament swelling continuing from day 7 to 14, the filament thickness slightly decreased, and pore area slightly increased from day 7 to day 14 in PBS for both bioinks and these changes were slightly greater in the HA-DA stromal bioink. Also, instead of weight increase during incubation, the weight of the stromal structures decreased during incubation in PBS and this decrease was more substantial in HA-DA stromal structures. Previously when characterizing the HA-DA stromal bioink structures Mörö et al. (2022) also observed weight

loss after initial swelling during incubation in PBS and offered as an explanation the removal of free unmodified HA and Col I added to the bioink formulation to improve the rheological properties of the bioink. Thus, here the decrease in filament thickness and weight is most likely also due to the removal of free unmodified HA and Col I from the HA-DA stromal bioink during incubation. Instead, as the unmodified HA is replaced with HAMA in the HA-DA HAMA stromal bioink, the decrease in filament thickness and weight could be due to the removal of free Col I from the bioink and the smaller changes observed when compared to the HA-DA stromal bioink could be attributed to removal of fewer components from the bioink. Alternatively, the smaller changes could be caused by the photocrosslinked HAMA polymer network decreasing the swelling of the HA-DA HAMA stromal structures as suggested earlier for structures incubated in LSC medium.

Mechanical properties are important for the stability of the material during cell culture and influence cellular behavior such as migration and stem cell differentiation (Caliari and Burdick, 2016). Therefore, the viscoelastic properties of printed stromal structures were analyzed. After 7 days of incubation, the storage moduli of stromal structures remained relatively unchanged in PBS for both bioinks whereas the storage moduli decreased in LSC medium. This was also observed during handling as stromal structures incubated in LSC medium were softer. These results indicate that LSC medium decreased the stiffness of stromal structures during incubation. Previously, Koivusalo et al. (2019) found that cell-laden HA-based hydrogels cultured for 24 h had a reduction in storage moduli when compared to acellular structures and suggested that this could be due to proteins and biomolecules present in the cell culture medium as well as cell surface proteins. Therefore, the decrease in stiffness observed here in bioprinted stromal structures could be due to the components of the LSC medium. The LSC medium components could disturb the stability of the hydrazone crosslinks in the bioink leading to a decrease in the number of crosslinks causing a decrease in the stiffness of the structure. Additionally, as stiffer networks with a higher degree of crosslinking typically exhibit lower swelling (Caliari and Burdick, 2016; Chimene et al., 2020), the decreased stiffness in LSC medium is in line with the more substantial swelling of structures in LSC medium.

As the aim was to enhance the stiffness and stability of the HA-DA stromal bioink, the effect of the HAMA component was also analyzed by comparing the storage moduli of HA-DA and HA-DA HAMA stromal structures. Based on storage moduli comparison at 1 Hz between bioinks, HA-DA HAMA stromal structures were significantly stiffer than HA-DA stromal structures in both incubation conditions on day 1. This confirms that the addition of HAMA to the HA-DA HAMA stromal bioink improves the stiffness of the bioprinted structures immediately after printing. However, as stated earlier, the storage

moduli of both bioinks decreased in LSC medium but this decrease was greater for HA-DA HAMA stromal structures to the extent that the storage moduli of HA-DA HAMA stromal structures had decreased to that of HA-DA stromal structures on day 7. This implies that LSC medium has a more considerable effect on the HA-DA HAMA stromal structures during incubation. Since HA-DA HAMA stromal structures have an additional HAMA polymer network, this network may influence the crosslinking of the HA-based polymer network in HA-DA HAMA stromal structures. If the HAMA polymer network influences the formation of the HA-based polymer network, the crosslinking density of the HA-based polymer network could be reduced. This could be caused by, for example, the HAMA polymer network limiting the available space or accessibility of reactive groups needed for the hydrazone crosslinking of the HA-based polymer network. Consequently, this less densely crosslinked HA-based polymer network in HA-DA HAMA stromal structures could be more susceptible to LSC medium as the medium could disturb the stability of the hydrazone bonds. As a result, by day 7 of incubation in LSC medium, the HA-DA HAMA stromal structures would have a very loosely crosslinked HA-based polymer network left, if any at all. This would leave behind a structure with substantially reduced stiffness due to the stiffness mainly relying on the stiffness of the HAMA polymer network with a highly porous structure. Moreover, an indication that the HA-based polymer network is indeed more susceptible to LSC medium than the HAMA polymer network and responsible for the decrease in stiffness of HA-DA HAMA stromal structures, is that on day 5 of culture in LSC medium, cell-laden HA-DA stromal structures had completely broken down whereas cell-laden HA-DA HAMA stromal structures could be cultured for 14 days without collapsing. However, it must be noted that cell-laden and acellular structures cannot directly be compared since cells and cellular functions may also affect the bioinks.

High transparency of the cornea is required for light transmission and refraction (Fuest et al., 2020). Human corneal light transmittance values increase with wavelength from 80% to 94% between 450 – 600 nm and is over 95% at wavelength 600 – 1000 nm (Beems and Van Best, 1990). Here, the transmittance of bioprinted structures was close to that of natural cornea. The transmittance for HA-DA and HA-DA HAMA stromal structures was 74.4 – 86.4% and 83.7 – 89.9%, respectively, in the visible light spectrum and are considered excellent in corneal transparency classification (Ventura et al., 2005). The results align with transmittance values previously reported for bioprinted corneal structures: 75 – 90% (Kutlehria et al., 2020), 65.8 – 99.5% (Boix-Lemonche et al., 2023), 78 – 95% (Mahdavi et al., 2020a) and 85 – 94% (Zhang et al., 2019a). Moreover, visual evaluation of transparency revealed that both acellular and cell-laden structures had

good transparency and that there was no major difference between transparency when comparing HA-DA and HA-DA HAMA structures. This is in accordance with earlier observations made by Mörö et al. (2022) who reported that HA-DA stromal bioink structures containing hASC-CSKs were transparent. These findings demonstrate that the HA-DA and HA-DA HAMA stromal bioinks could be appropriate for corneal TE regarding transparency. Interestingly, HA-DA acellular and cell-laden stromal structures turned slightly yellow while remaining transparent by day 7. This is caused by the gradual self-polymerization of the free dopamine moiety in the HA-DA-CDH crosslinking component and was also observed by Koivusalo et al. (2019) and Mörö et al. (2022) in acellular structures. Instead, HA-DA HAMA stromal structures remained transparent without any color change during incubation indicating that the gradual self-polymerization of dopamine does not occur and could be affected by the HAMA polymer network.

To conclude, based on characterizing the bioinks and bioprinted stromal structures without cells, the HA-DA HAMA stromal bioink seemed to have slightly improved stiffness and stability when compared to the HA-DA stromal bioink when considering handling, swelling, and shape fidelity of printed structures after 14 days of incubation in LSC medium. Also, on day 1 after printing HA-DA HAMA stromal structures were significantly stiffer than HA-DA stromal structures. However, on day 7 the stiffness of HA-DA HAMA stromal structures had reduced to that of HA-DA stromal structures. Notably, rheological tests were not performed for printed stromal structures on day 14 where the most prominent benefits of the HA-DA HAMA stromal bioink over the HA-DA stromal bioink had been observed in handling and shape fidelity. Based on these results for bioink characterization, the HA-DA HAMA stromal bioink seemed like a suitable option for the LSC medium co-culture condition. Additionally, it was discovered that the shape fidelity, swelling behavior, and mechanical properties of stromal structures significantly differed between the LSC medium co-culture condition and PBS. As a possible explanation for these findings, it was suggested that components of the LSC medium could disturb the hydrazone bonds of HA-based polymer networks in the bioinks leading to greater swelling and reduced mechanical properties. These findings demonstrate that the conditions where materials are characterized in should be chosen bearing in mind the final application since for example the composition of cell culture mediums differ largely from the commonly used PBS. Moreover, as the composition of cell culture medium varies largely between cell types, especially stem cells, (van der Sanden et al., 2010), and since manufacturers do not always disclose medium components, material characterization should

be always done for each application separately. This is especially important in 3D bioprinting applications since the shape fidelity of bioprinted structures should be maintained after bioprinting for a desired time period (Karvinen and Kellomäki, 2023).

11.2 Cytocompatibility of stromal bioinks

In addition to good printability, shape fidelity, and suitable mechanical properties, bioinks should enable the natural functions of cells (Deo et al., 2020; Karvinen and Kellomäki, 2023). The HA-DA stromal bioink demonstrated good cytocompatibility as viability was high on day 7 after printing and hASC-CSKs had elongated morphology in stromal structures. This corresponds with the excellent cytocompatibility of the HA-DA stromal bioink previously reported by Mörö et al. (2022). Instead, the number of dead cells was high in stromal structures printed with the HA-DA HAMA stromal bioink and viable cells retained rounded morphology throughout culture in HA-DA HAMA stromal structures with both 30 and 60 s UV exposure times. These results demonstrate that even though the HA-DA HAMA stromal bioink had improved stability for the LSC medium co-culture condition, it did not have the necessary cytocompatibility required for bioinks. This highlights that initial cell screenings should always be done when designing new bioinks for bioprinting (Karvinen and Kellomäki, 2023). Next, the differences and possible explanations for these observations are discussed in more detail.

It is known that UV light used in the crosslinking process of bioinks may affect cytocompatibility (Zennifer et al., 2022). UV light with wavelengths in the range of 320 – 400 nm can damage the DNA of cells and it has been also suggested that the free radicals formed from the cleavage of photoinitiators during photocrosslinking of bioinks could be responsible for cytotoxicity (Knowlton et al., 2017; Lim et al., 2020). UV light with wavelength of 365 nm was used in this thesis. It is a commonly used wavelength due to being closer to the visible light range and therefore used to minimize genotoxicity and cytotoxicity (Lim et al., 2020). Here, the results indicate that UV exposure may have some effect on cell viability as the number of dead cells was slightly higher in HA-DA HAMA stromal structures exposed to UV than in structures without UV exposure. Therefore, the unsuitable cytocompatibility of the HA-DA HAMA stromal bioink could be due to the free radicals formed during photocrosslinking which could be harmful to hASC-CSKs and/or the UV light of 365 nm used since it is in the DNA damaging UV light range. However, no significant effects on cell viability were detected when decreasing UV exposure time from 60 to 30 s. This could be due to a relatively small difference between these exposure times and therefore no significant differences would be observed after initial UV exposure. Nevertheless, good cell viability has been previously observed in 3D bioprinted

structures exposed to UV light. For example, hASCs bioprinted with GelMA as bioink and exposed to 180 s of UV light were reported to have a viability of 88.8% on day 1 and 93.6% on day 15 after extrusion-based-bioprinting (Albrecht et al., 2022). Also, hCSK viability has been over 95% after 3 weeks of culture in UV crosslinked GelMA structures printed using extrusion-based bioprinting (Kilic Bektas and Hasirci, 2020). Therefore, to evaluate whether the unsuitable cytocompatibility of HA-DA HAMA stromal bioink is due to the UV light or exposure time, the viability of hASC-CSKs could be assessed in the original HA-DA stromal bioink upon UV exposure. Also, the use of visible light for photocrosslinking could be tested since LAP, the used photoinitiator, also absorbs in the visible light range (405 nm) (Knowlton et al., 2017; Lim et al., 2020). An alternative reason for the unsuitable cytocompatibility could be the environment that HA-DA HAMA stromal bioink creates for the cells after photocrosslinking which is discussed next.

After bioprinting, bioinks should provide an environment that mimics the natural ECM supporting cellular functions (Deo et al., 2020). It is known that matrix stiffness influences the behavior of encapsulated cells and that stiff structures formed from densely cross-linked hydrogel networks can restrict cell migration and limit nutrient diffusion (Chimene et al., 2020). Previously, hCSKs showed rounded morphology in 3D bioprinted GelMA structures and this was attributed to high crosslinking density in the structures which may have restricted the cell mobility and diffusion of oxygen and growth medium (Kilic Bektas and Hasirci, 2020). Here, IF staining shows that the hASC-CSKs retain rounded morphology in HA-DA HAMA stromal structures throughout the 21-day culture. Therefore, another explanation for the inferior cytocompatibility of the HA-DA HAMA stromal bioink could be that the bioink cannot support cell migration and other cellular functions. This could be due to the high initial stiffness of the bioprinted structures and the rapid decrease of mechanical properties by day 7 creating an unsuitable environment for hASC-CSKs to grow and migrate in. However, it is important to consider that the characterization of mechanical properties was done without cells and with different culture medium. Therefore, to make better conclusions about the effects of matrix stiffness on the hASC-CSKs, the characterization should be performed with cell-laden structures in the same media. Instead in HA-DA stromal structures, hASC-CSKs were able to migrate and form cell-cell interactions indicated by elongated morphology and the expression of the gap junction protein Cx43 on day 7. By the end of culture on day 21, the hASC-CSKs had continued to form cellular networks demonstrating that the HA-DA stromal bioink can provide a more suitable environment for hASC-CSKs. Previously, Mörö et al. (2022) reported that when compared to hASCs in bioprinted HA-DA stromal structures, hASC-

CSKs had more dendritic cell morphology with roundish cell bodies and thin cellular extensions. Here, hASC-CSKs did not demonstrate such morphology which could be due to using a different hASC line or due to continuing differentiation before bioprinting for 14 days instead of seven days as reported by Mörö et al. (2022). Nonetheless, HA-DA stromal bioink showed superior cytocompatibility over HA-DA HAMA stromal bioink which will be discussed further next.

Cells should express their normal functions in printed constructs in addition to high viability (Wu et al., 2023), and thus the future success of corneal bioprinting relies on the ability of printed cells to facilitate ECM remodeling to establish the functionality of the tissue (Isaacson et al., 2018; Mörö et al., 2022). Therefore, here, the expression of cornea stroma specific markers Col I and lumican were evaluated. In native corneal ECM, Col I is arranged as highly organized fibrils and is produced by hCSKs (S. Chen et al., 2015; Meek and Knupp, 2015). IF staining shows that Col I expression changes in HA-DA stromal structures with hASC-CSKs during the 21-day culture. Extracellular Col I did not have fiber-like appearance on day 7 but by day 21 was clearly fiber-like. This fiber-like Col I observed on day 21 could be produced by hASC-CSKs as the intracellular expression decreased from day 14 to 21. However, since the HA-DA stromal bioink also contains human Col I, the observed fiber-like Col I could be from the bioink which may have self-assembled over time or been remodeled by the hASC-CSKs. To examine whether the fiber-like Col I is from the bioink or produced by the cells, gene expression profiling and IF staining could be performed for cell-laden HA-DA stromal structures with and without the Col I bioink component. If hASC-CSKs were responsible for the production or remodeling of the Col I it could indicate functionality of the cells since one of the important functions of hCSKs is to synthesize collagens and maintain ECM environment (Sridhar, 2018). Previously, Sorkio et al. (2018) have also observed fiber-like Col I in bioprinted stromal structures which was likely produced or remodeled by the bioprinted hASCs. Moreover, the expression of lumican was examined as lumican is one of the major proteoglycans of the stroma (Carlson et al., 2005). The cornea stroma specific marker lumican was expressed intracellularly throughout the culture and extracellular lumican expression with fibrillar organization increased during culture in HA-DA stromal structures. This is in accordance with earlier observations made by Mörö et al. (2022) who reported lumican expression with fibrillar organization in HA-DA stromal structures prepared with hASC-CSKs. Lumican expression of hASC-CSKs also indicates that differentiation of hASCs towards CSK lineage has been induced and continues in the bioprinted HA-DA stromal structure. Nevertheless, this should be confirmed with gene expression profiling with for example quantitative real-time polymerase chain reaction

(qPCR) analysis as previously reported by Mörö et al. (2022). Instead, in HA-DA HAMA stromal structures extracellular Col I was not fiber-like and only some possible intracellular lumican expression was observed demonstrating again that the HA-DA HAMA stromal bioink cannot support cellular functions, and that the HA-DA stromal bioink has superior cytocompatibility.

As the aim of this thesis was to modify the stiffness and stability of the HA-DA stromal bioink to enable the co-culture of 3D bioprinted cornea mimicking structures with stroma and epithelium in LSC medium, the stability of cell-laden stromal structures was also assessed in the co-culture condition. HA-DA stromal structures had completely broken down on day 5 of culture whereas HA-DA HAMA structures remained stable until the end of culture but had hardly any viable cells on day 14. This confirms that even though the structure remained stable until the end of culture the HA-DA HAMA stromal bioink is not cytocompatible with hASC-CSKs. Instead, the breaking down of HA-DA stromal structures by day 5 demonstrates the initial problem with HA-DA stromal structures not maintaining their structural stability when cultured in LSC medium. A reason for the rapid breakdown by day 5, which was not observed for acellular structures, could be the cells present in the bioink interfering with the crosslinking process decreasing the degree of crosslinking (Cui et al., 2020). Also, the rapid collapse of HA-DA stromal structures in LSC medium confirms that the LSC medium specifically has a significant effect on the HA-DA stromal bioink stability since cell-laden HA-DA stromal structures could be cultured in KDM until the end of incubation on day 21. The stability of the HA-DA stromal structures in KDM is in line with previous observations since cell-laden HA-DA stromal structures have been cultured up to day 21 in KDM and hASC medium (Mörö et al., 2022). Since the composition of the LSC medium is undisclosed, it is impossible to precisely compare the medium composition of KDM and LSC medium to determine why HA-DA stromal structures are more stable in KDM. Possibly, as LSC medium (CELLnTEC, 2023) has more medium components than KDM (Chapter 9.6.2) the combined effect of all these components could influence the HA-DA stromal structures.

11.3 Human cornea mimicking structures with stroma and epithelium

Finally, a proof-of-concept for extrusion-based 3D bioprinting of human cornea mimicking structures with stroma and epithelium was tested and the printed structures were co-cultured in two different co-culture conditions: LSC medium and KDM+LSC medium. As the cytocompatibility of the HA-DA HAMA stromal bioink was inadequate and the HA-DA

cell-laden stromal structures had collapsed during culture in LSC medium, the crosslinking component concentration of the HA-DA stromal bioink was increased to prolong the culture time in LSC medium. Increasing the concentration of crosslinking components in the bioink increases the number of crosslinks in bioprinted structures, and therefore should be more stable in the LSC medium. Structures were stable in both co-culture conditions on day 4 of culture. However, on day 7 structures in the LSC medium co-culture condition had swelled considerably while structures in the KDM+LSC co-culture condition remained stable. This implies that the LSC medium and the cells disturb the stability of the HA-DA stromal bioink, despite the culture time being prolonged from 5 to 7 days by increasing crosslinking component concentration. Also, as the structures are more stable in the KDM+LSC co-culture condition, the results confirm that the composition of the medium had a significant effect on the stability of the structure.

Previously, 3D bioprinting of corneal structures containing stromal and epithelial layers has been conducted using LaBP (Sorkio et al., 2018) and DLP (He et al., 2022). Therefore, to the best of my knowledge, this is the first time extrusion-based 3D bioprinting has been used for the fabrication of multiple layers of the cornea. Corneal structures containing stromal and epithelial layers were printed successfully and IF staining revealed that the epithelial and stromal layer were clearly separated as ABCG2 expressing hPSC-LSCs were only expressed on the uppermost part of the printed structures. Previously, Sorkio et al. (2018) reported bioprinted hESC-LSCs forming a stratified layer on the surface of bioprinted stromal structures. Here however the hPSC-LSCs did not form stratified epithelium and the cells were mostly dispersed separately within the epithelial layer. This could be due to the hPSC-LSC cell density being lower in this thesis when compared to Sorkio et al. (2018) who used a high cell density of 30 million cells/ml. Therefore, in the future, a higher cell density should be tested to see whether it could allow the formation of a stratified epithelium onto the stromal layer.

The clear separation of the epithelial and stromal layer could be observed in both co-culture conditions, but on day 7 the amount of hPSC-LSCs was lower in LSC medium and the hASC-CSK cell morphology differed significantly between the two conditions hASC-CSKs having elongated morphology only in KDM+LSC medium. A possible explanation for the reduced number of hPSC-LSCs on day 7 in LSC medium could be the more significant swelling observed in LSC medium than in KDM+LSC medium. This would be in line with previous observations where cell loss from hydrogels was attributed to swelling pulling cells further away from each other and the wash-out of unattached cells (Koivusalo et al., 2018). Notably, as the number of hPSC-LSCs on day 7 was higher and hASC-CSKs had elongated morphology only in KDM+LSC medium, the KDM+LSC

medium co-culture condition seems to be more suitable for the co-culture of cornea mimicking structures with stroma and epithelium. This is reasonable since the KDM+LSC medium contains components to support both cell types during culture. Typically, co-culture medium design gives more consideration to the relatively more sensitive cell type, which in this case was the hPSC-LSCs, but importantly an optimal co-culture medium should be designed to support the proliferation, differentiation, and maintenance of phenotypes of all co-cultured cell types (Wu et al., 2023). This is challenging and thus in the future, the KDM+LSC medium co-culture condition should be developed further and the effect of the co-culture condition on both cell types should be analyzed. Previously, the co-culture of human CSSCs and corneal epithelial cells led to more complete differentiation and growth of both cell types when compared to the culture of the cell types alone (Gosselin et al., 2018). Thus, also interactions between hASC-CSKs and hPSC-LSCs should be studied.

11.4 Future perspectives

In this thesis, a photocrosslinkable HA-DA HAMA stromal bioink was developed which showed slightly improved stability in the LSC medium co-culture condition. Nevertheless, the bioink did not have the necessary cytocompatibility. Thus, it was not used for bioprinting cornea mimicking structures with stroma and epithelium. To fully understand, why the HA-DA HAMA stromal bioink did not have adequate cytocompatibility, the effect of UV light or exposure time on the hASC-CSKs could be analyzed as discussed in Chapter 11.2. In addition, the possible effect of the HAMA polymer network on the HA-based polymer network crosslinking could be studied in more detail to understand the rapid changes happening in stiffness during incubation in LSC medium. For example, to determine whether the HAMA polymer network influences the crosslinking of the HA-based polymer network, the concentration of HAMA could be decreased in the bioink, to study if better hydrazone crosslinking of the HA-based polymer network occurs due to increased space for accessibility of reactive groups. This could create a HA-DA HAMA stromal bioink which does not have as rapid changes in stiffness during culture if the HA-based polymer network were better crosslinked. After this, it would be important to assess whether these changes in the bioink composition would affect the cytocompatibility of the bioink. Additionally, the cytocompatibility of the HA-DA HAMA stromal bioink could be studied with other cell types instead of hASC-CSKs. All in all, if the HA-DA HAMA stromal bioink were to be used for bioprinting of cornea mimicking structures in the future, further optimization of the composition of the bioink is needed together with cytocompatibility test of the modified compositions.

However, at the moment a more promising approach for bioprinting cornea mimicking structures with stroma and epithelium is using a HA-DA stromal bioink composition with increased crosslinking component concentration together with an appropriate culture medium which would be the KDM+LSC medium based on the findings of this thesis. In the future, the crosslinking component concentration of this bioink could be raised to further increase the crosslinking density and enable better stability during culture. The cytocompatibility of this bioink, as well as the effects of the suggested KDM+LSC medium on cell proliferation, differentiation, and phenotypes, should be studied. Also, in cornea mimicking structures with stroma and epithelium, cell densities should be optimized, and the interactions between different cell types should be analyzed. In order to utilize 3D bioprinted cornea mimicking structures for transplantation, *in vivo* studies of the structures are needed, the curved shape of the cornea should be considered, and structures with mechanical properties closer to those of the natural cornea should be created (Balters and Reichl, 2023).

12. CONCLUSIONS

The aim of this thesis was to enhance the stiffness and stability of the HA-DA stromal bioink to enable the co-culture of 3D bioprinted cornea mimicking structures with stroma and epithelium in the LSC medium co-culture condition. For this, a photocrosslinkable HA-DA HAMA stromal bioink was created and compared to the original HA-DA stromal bioink. The printability, viscosity, shape fidelity, swelling behavior, handling, mechanical properties, and transparency were first compared in stromal structures without cells. After this, the cytocompatibility of both bioinks with hASC-CSKs was assessed. Finally, based on the results cornea mimicking structures with stroma and epithelium were printed.

HA-DA and HA-DA HAMA stromal bioinks had similar printability, shear-thinning behavior, and transparency which were suitable for corneal 3D bioprinting. Moreover, based on characterizing the bioinks and printed stromal structures without cells in LSC medium, the HA-DA HAMA stromal bioink seemed to have improved characteristics regarding handling, swelling, and shape fidelity of printed structures. However, the HA-DA HAMA stromal bioink did not have the necessary cytocompatibility required for bioinks, and the cytocompatibility of the HA-DA HAMA stromal bioink was inferior when compared to the HA-DA stromal bioink. This demonstrated the importance and need for cytocompatibility tests as a part of bioink characterization. In addition, it was confirmed that the LSC medium co-culture condition has a significant effect on the HA-DA stromal bioink properties. Thus, bioink characterization should always be conducted considering the final application of the 3D bioprinted construct.

In the final part of this thesis, cornea mimicking structures with stroma and epithelium were printed successfully for the first time using extrusion-based bioprinting. For this, a HA-DA stromal bioink with increased crosslinking component concentration was used which prolonged the culture time but did not give sufficient stability in LSC medium. However, it was discovered that a co-culture condition combining KDM and LSC medium is more suitable as a co-culture condition for cornea mimicking structures with stroma and epithelium due to better fulfilling the needs of both cell types and due to the HA-DA stromal bioink having improved stability in the medium. Despite successful findings, further research is needed to optimize the cell density in the epithelial layer and to analyze the effect of the co-culture medium on cells. Consequently, this thesis advances the development of stable and functional bioprinted corneal structures and provides valuable information in the field of bioprinting multiple cell types into one structure.

REFERENCES

- Ahmad, S., Stewart, R., Yung, S., Kolli, S., Armstrong, L., Stojkovic, M., Figueiredo, F., Lako, M., 2007. Differentiation of Human Embryonic Stem Cells into Corneal Epithelial-Like Cells by In Vitro Replication of the Corneal Epithelial Stem Cell Niche. *Stem Cells Dayt. Ohio* 25, 1145–1155. <https://doi.org/10.1634/stemcells.2006-0516>
- Ahmed, E.M., 2015. Hydrogel: Preparation, characterization, and applications: A review. *J. Adv. Res.* 6, 105–121. <https://doi.org/10.1016/j.jare.2013.07.006>
- Albrecht, F.B., Schmidt, F.F., Volz, A.-C., Kluger, P.J., 2022. Bioprinting of 3D Adipose Tissue Models Using a GelMA-Bioink with Human Mature Adipocytes or Human Adipose-Derived Stem Cells. *Gels* 8, 611-. <https://doi.org/10.3390/gels8100611>
- Alió del Barrio, J.L., El Zarif, M., Azaar, A., Makdissy, N., Khalil, C., Harb, W., El Achkar, I., Jawad, Z.A., de Miguel, M.P., Alió, J.L., 2018. Corneal Stroma Enhancement With Decellularized Stromal Laminae With or Without Stem Cell Recellularization for Advanced Keratoconus. *Am. J. Ophthalmol.* 186, 47–58. <https://doi.org/10.1016/j.ajo.2017.10.026>
- Alió Del Barrio, J.L., El Zarif, M., de Miguel, M.P., Azaar, A., Makdissy, N., Harb, W., El Achkar, I., Arnalich-Montiel, F., Alió, J.L., 2017. Cellular Therapy With Human Autologous Adipose-Derived Adult Stem Cells for Advanced Keratoconus. *Cornea* 36, 952–960. <https://doi.org/10.1097/ICO.0000000000001228>
- Bakhshandeh, B., Zarrintaj, P., Oftadeh, M.O., Keramati, F., Fouladiha, H., Sohrabi-jahromi, S., Ziraksaz, Z., 2017. Tissue engineering; strategies, tissues, and biomaterials. *Biotechnol. Genet. Eng. Rev.* 33, 144–172. <https://doi.org/10.1080/02648725.2018.1430464>
- Balters, L., Reichl, S., 2023. 3D bioprinting of corneal models: A review of the current state and future outlook. *J. Tissue Eng.* 14. <https://doi.org/10.1177/20417314231197793>
- Barrientez, B., Nicholas, S.E., Whelchel, A., Sharif, R., Hjortdal, J., Karamichos, D., 2019. Corneal injury: Clinical and molecular aspects. *Exp. Eye Res.* 186, 107709–107709. <https://doi.org/10.1016/j.exer.2019.107709>
- Beems, E.M., Van Best, J.A., 1990. Light transmission of the cornea in whole human eyes. *Exp. Eye Res.* 50, 393–395. [https://doi.org/10.1016/0014-4835\(90\)90140-P](https://doi.org/10.1016/0014-4835(90)90140-P)
- Białkowska, K., Komorowski, P., Bryszewska, M., Miłowska, K., 2020. Spheroids as a Type of Three-Dimensional Cell Cultures-Examples of Methods of Preparation and the Most Important Application. *Int. J. Mol. Sci.* 21, 6225-. <https://doi.org/10.3390/ijms21176225>
- Bird, R.E., Lemmel, S.A., Yu, X., Zhou, Q.A., 2021. Bioorthogonal Chemistry and Its Applications. *Bioconjug. Chem.* 32, 2457–2479. <https://doi.org/10.1021/acs.bioconjchem.1c00461>
- Boix-Lemonche, G., Nagymihaly, R.M., Niemi, E.M., Josifovska, N., Johansen, S., Moe, M.C., Scholz, H., Petrovski, G., 2023. Intra-Corneal Implantation of 3D Bioprinted Scaffolds Containing Mesenchymal Stromal Cells using Femtosecond-Laser-Assisted Intrastromal Keratoplasty. *Macromol. Biosci.* e2200422–e2200422. <https://doi.org/10.1002/mabi.202200422>
- Burillon, C., Huot, L., Justin, V., Nataf, S., Chapuis, F., Decullier, E., Damour, O., 2012. Cultured autologous oral mucosal epithelial cell sheet (CAOMECS) transplantation for the treatment of corneal limbal epithelial stem cell deficiency. *Invest. Ophthalmol. Vis. Sci.* 53, 1325–1331. <https://doi.org/10.1167/iovs.11-7744>
- Caliari, S.R., Burdick, J.A., 2016. A practical guide to hydrogels for cell culture. *Nat. Methods* 13, 405–414. <https://doi.org/10.1038/nmeth.3839>
- Carlson, E.C., Liu, C.-Y., Chikama, T., Hayashi, Y., Kao, C.W.-C., Birk, D.E., Funderburgh, J.L., Jester, J.V., Kao, W.W.-Y., 2005. Keratocan, a Cornea-specific Keratan Sulfate Proteoglycan, Is Regulated by Lumican. *J. Biol. Chem.* 280, 25541–25547. <https://doi.org/10.1074/jbc.M500249200>
- CELLnTEC, 2023. URL <https://cellntec.com/products/cnt-07> (accessed 10.16.23).
- Chakrabarty, K., Shetty, R., Ghosh, A., 2018. Corneal cell therapy: with iPSCs, it is no more a far-sight. *Stem Cell Res. Ther.* 9, 287–287. <https://doi.org/10.1186/s13287-018-1036-5>
- Chan, A.A., Hertszenberg, A.J., Funderburgh, M.L., Mann, M.M., Du, Y., Davoli, K.A., Mich-Basso, J.D., Yang, L., Funderburgh, J.L., 2013. Differentiation of human embryonic stem cells into cells with corneal keratocyte phenotype. *PLoS One* 8, e56831–e56831. <https://doi.org/10.1371/journal.pone.0056831>

- Chan, B.P., Leong, K.W., 2008. Scaffolding in tissue engineering: general approaches and tissue-specific considerations. *Eur. Spine J.* 17, 467–479. <https://doi.org/10.1007/s00586-008-0745-3>
- Che, X., Wu, H., Jia, C., Sun, H., Ou, S., Wang, J., Jeyalatha, M.V., He, X., Yu, J., Zuo, C., Liu, Z., Li, W., 2019. A Novel Tissue-Engineered Corneal Stromal Equivalent Based on Amniotic Membrane and Keratocytes. *Invest. Ophthalmol. Vis. Sci.* 60, 517–527. <https://doi.org/10.1167/iovs.18-24869>
- Chen, G., QI, Y., NIU, L., DI, T., ZHONG, J., FANG, T., YAN, W., 2015. Application of the cell sheet technique in tissue engineering. *Biomed. Rep.* 3, 749–757. <https://doi.org/10.3892/br.2015.522>
- Chen, S., Mienaltowski, M.J., Birk, D.E., 2015. Regulation of corneal stroma extracellular matrix assembly. *Exp. Eye Res.* 133, 69–80. <https://doi.org/10.1016/j.exer.2014.08.001>
- Chen, Z., You, J., Liu, X., Cooper, S., Hodge, C., Sutton, G., Crook, J.M., Wallace, G.G., 2018. Biomaterials for corneal bioengineering. *Biomed. Mater. Bristol* 13, 032002–032002. <https://doi.org/10.1088/1748-605X/aa92d2>
- Chimene, D., Kaunas, R., Gaharwar, A.K., 2020. Hydrogel Bioink Reinforcement for Additive Manufacturing: A Focused Review of Emerging Strategies. *Adv. Mater. Weinh.* 32, e1902026-n/a. <https://doi.org/10.1002/adma.201902026>
- Choi, J.R., Yong, K.W., Choi, J.Y., Cowie, A.C., 2019. Recent advances in photo-crosslinkable hydrogels for biomedical applications. *BioTechniques* 66, 40–53. <https://doi.org/10.2144/btn-2018-0083>
- Costantini, M., Colosi, C., Świąszkowski, W., Barbetta, A., 2018. Co-axial wet-spinning in 3D bioprinting: state of the art and future perspective of microfluidic integration. *Biofabrication* 11, 012001. <https://doi.org/10.1088/1758-5090/aae605>
- Crabb, R.A., Hubel, A., 2008. Influence of Matrix Processing on the Optical and Biomechanical Properties of a Corneal Stroma Equivalent. *Tissue Eng. Part A* 14, 173–182. <https://doi.org/10.1089/ten.a.2007.0139>
- Cui, X., Li, J., Hartanto, Y., Durham, M., Tang, J., Zhang, H., Hooper, G., Lim, K., Woodfield, T., 2020. Advances in Extrusion 3D Bioprinting: A Focus on Multicomponent Hydrogel-Based Bioinks. *Adv. Healthc. Mater.* 9, e1901648-n/a. <https://doi.org/10.1002/adhm.201901648>
- Dell, A.C., Wagner, G., Own, J., Geibel, J.P., 2022. 3D Bioprinting Using Hydrogels: Cell Inks and Tissue Engineering Applications. *Pharmaceutics* 14, 2596-. <https://doi.org/10.3390/pharmaceutics14122596>
- DelMonte, D.W., Kim, T., 2011. Anatomy and physiology of the cornea. *J. Cataract Refract. Surg.* 37, 588–598. <https://doi.org/10.1016/j.jcrs.2010.12.037>
- Deng, S.X., Kruse, F., Gomes, J.A.P., Chan, C.C., Daya, S., Dana, R., Figueiredo, F.C., Kinoshita, S., Rama, P., Sangwan, V., Slomovic, A.R., Tan, D., 2020. Global Consensus on the Management of Limbal Stem Cell Deficiency. *Cornea* 39, 1291–1302. <https://doi.org/10.1097/ICO.0000000000002358>
- Deo, K.A., Singh, K.A., Peak, C.W., Alge, D.L., Gaharwar, A.K., 2020. Bioprinting 101: Design, Fabrication, and Evaluation of Cell-Laden 3D Bioprinted Scaffolds. *Tissue Eng. Part A* 26, 318–338. <https://doi.org/10.1089/ten.tea.2019.0298>
- Derakhshanfar, S., Mbeleck, R., Xu, K., Zhang, X., Zhong, W., Xing, M., 2018. 3D bioprinting for biomedical devices and tissue engineering: A review of recent trends and advances. *Bioact. Mater.* 3, 144–156. <https://doi.org/10.1016/j.bioactmat.2017.11.008>
- Di Iorio, E., Barbaro, V., Ruzza, A., Ponzin, D., Pellegrini, G., De Luca, M., 2005. Isoforms of DeltaNp63 and the migration of ocular limbal cells in human corneal regeneration. *Proc. Natl. Acad. Sci. - PNAS* 102, 9523–9528.
- Ding, Y.-W., Zhang, X.-W., Mi, C.-H., Qi, X.-Y., Zhou, J., Wei, D.-X., 2023. Recent advances in hyaluronic acid-based hydrogels for 3D bioprinting in tissue engineering applications. *Smart Mater. Med.* 4, 59–68. <https://doi.org/10.1016/j.smaim.2022.07.003>
- Downie, L.E., Bandlitz, S., Bergmanson, J.P., Craig, J.P., Dutta, D., Maldonado-Codina, C., Ngo, W., Siddireddy, J.S., Wolffsohn, J.S., 2021. BCLA CLEAR - Anatomy and physiology of the anterior eye. *Contact Lens Anterior Eye* 44, 132–156. <https://doi.org/10.1016/j.clae.2021.02.009>
- Du, Y., Roh, D.S., Funderburgh, M.L., Mann, M.M., Marra, K.G., Rubin, J.P., Li, X., Funderburgh, J.L., 2010. Adipose-derived stem cells differentiate to keratocytes in vitro. *Mol. Vis.* 16, 2680–2689.

- Dua, H.S., Shanmuganathan, V.A., Powell-Richards, A.O., Tighe, P.J., Joseph, A., 2005. Limbal epithelial crypts: a novel anatomical structure and a putative limbal stem cell niche. *Br. J. Ophthalmol.* 89, 529–532. <https://doi.org/10.1136/bjo.2004.049742>
- Duarte Campos, D.F., Rohde, M., Ross, M., Anvari, P., Blaeser, A., Vogt, M., Panfil, C., Yam, G.H.-F., Mehta, J.S., Fischer, H., Walter, P., Fuest, M., 2019. Corneal bioprinting utilizing collagen-based bioinks and primary human keratocytes. *J. Biomed. Mater. Res. A* 107, 1945–1953. <https://doi.org/10.1002/jbm.a.36702>
- Dziasko, M.A., Daniels, J.T., 2016. Anatomical features and cell-cell interactions in the human limbal epithelial stem cell niche. *Ocul. Surf.* 14, 322–330. <https://doi.org/10.1016/j.jtos.2016.04.002>
- Dzobo, K., Motaung, K.S.C.M., Adesida, A., 2019. Recent Trends in Decellularized Extracellular Matrix Bioinks for 3D Printing: An Updated Review. *Int. J. Mol. Sci.* 20, 4628–. <https://doi.org/10.3390/ijms20184628>
- El Zarif, M., Alió, J.L., Alió Del Barrio, J.L., Abdul Jawad, K., Palazón-Bru, A., Abdul Jawad, Z., De Miguel, M.P., Makdissy, N., 2021. Corneal Stromal Regeneration Therapy for Advanced Keratoconus: Long-term Outcomes at 3 Years. *Cornea* 40, 741–754. <https://doi.org/10.1097/ICO.0000000000002646>
- EMA, 2018. Holoclar [WWW Document]. Eur. Med. Agency. URL <https://www.ema.europa.eu/en/medicines/human/EPAR/holoclar> (accessed 9.26.23).
- Espana, E.M., Birk, D.E., 2020. Composition, structure and function of the corneal stroma. *Exp. Eye Res.* 198, 108137–108137. <https://doi.org/10.1016/j.exer.2020.108137>
- Espandar, L., Bunnell, B., Wang, G.Y., Gregory, P., McBride, C., Moshirfar, M., 2012. Adipose-Derived Stem Cells on Hyaluronic Acid-Derived Scaffold: A New Horizon in Bioengineered Cornea. *Arch. Ophthalmol.* 130, 202–208. <https://doi.org/10.1001/archophthalmol.2011.1398>
- Fagerholm, P., Lagali, N.S., Ong, J.A., Merrett, K., Jackson, W.B., Polarek, J.W., Suuronen, E.J., Liu, Y., Brunette, I., Griffith, M., 2014. Stable corneal regeneration four years after implantation of a cell-free recombinant human collagen scaffold. *Biomaterials* 35, 2420–2427. <https://doi.org/10.1016/j.biomaterials.2013.11.079>
- Fang, W., Yang, M., Wang, L., Li, W., Liu, M., Jin, Y., Wang, Yuhui, Yang, R., Wang, Ying, Zhang, K., Fu, Q., 2023. Hydrogels for 3D bioprinting in tissue engineering and regenerative medicine: Current progress and challenges. *Int. J. Bioprinting* 9, 759–759. <https://doi.org/10.18063/ijb.759>
- Feizi, S., Jafarinasab, M.R., Karimian, F., Hasanpour, H., Masudi, A., 2014. Central and peripheral corneal thickness measurement in normal and keratoconic eyes using three corneal pachymeters. *J. Ophthalmic Vis. Res.* 9, 296–304. <https://doi.org/10.4103/2008-322X.143356>
- Fuest, M., Yam, G.H.-F., Mehta, J.S., Duarte Campos, D.F., 2020. Prospects and Challenges of Translational Corneal Bioprinting. *Bioeng. Basel* 7, 71–. <https://doi.org/10.3390/bioengineering7030071>
- Gain, P., Jullienne, R., He, Z., Aldossary, M., Acquart, S., Cognasse, F., Thuret, G., 2016. Global Survey of Corneal Transplantation and Eye Banking. *JAMA Ophthalmol.* 134, 1–8. <https://doi.org/10.1001/jamaophthalmol.2015.4776>
- Ghasemi-Mobarakeh, L., Kolahreez, D., Ramakrishna, S., Williams, D., 2019. Key terminology in biomaterials and biocompatibility. *Curr. Opin. Biomed. Eng.* 10, 45–50. <https://doi.org/10.1016/j.cobme.2019.02.004>
- Ghorbani, F., Ghalandari, B., Khajehmohammadi, M., Bakhtiary, N., Tolabi, H., Sahranavard, M., Fathi-Karkan, S., Nazar, V., Hasan Niari Niar, S., Armoon, A., Ettelaei, M., Tavakoli Bani-izi, M., Collins, M.N., 2023. Photo-cross-linkable hyaluronic acid bioinks for bone and cartilage tissue engineering applications. *Int. Mater. Rev.* ahead-of-print, 1–42. <https://doi.org/10.1080/09506608.2023.2167559>
- Gonzalez, G., Sasamoto, Y., Ksander, B.R., Frank, M.H., Frank, N.Y., 2018. Limbal stem cells: identity, developmental origin, and therapeutic potential. *Wiley Interdiscip. Rev. Dev. Biol.* 7. <https://doi.org/10.1002/wdev.303>
- Gosselin, E.A., Torregrosa, T., Ghezzi, C.E., Mendelsohn, A.C., Gomes, R., Funderburgh, J.L., Kaplan, D.L., 2018. Multi-layered silk film coculture system for human corneal epithelial and stromal stem cells. *J. Tissue Eng. Regen. Med.* 12, 285–295. <https://doi.org/10.1002/term.2499>
- Gouveia, R.M., González-Andrades, E., Cardona, J.C., González-Gallardo, C., Ionescu, A.M., Garzon, I., Alaminos, M., González-Andrades, M., Connon, C.J., 2017. Controlling the

- 3D architecture of Self-Lifting Auto-generated Tissue Equivalents (SLATEs) for optimized corneal graft composition and stability. *Biomaterials* 121, 205–219. <https://doi.org/10.1016/j.biomaterials.2016.12.023>
- Groll, J., Burdick, J.A., Cho, D.-W., Derby, B., Gelinsky, M., Heilshorn, S.C., Jüngst, T., Malda, J., Mironov, V.A., Nakayama, K., Ovsianikov, A., Sun, W., Takeuchi, S., Yoo, J.J., Woodfield, T.B.F., 2018. A definition of bioinks and their distinction from biomaterial inks. *Biofabrication* 11, 013001–013001. <https://doi.org/10.1088/1758-5090/aaec52>
- Guérin, L.-P., Le-Bel, G., Desjardins, P., Couture, C., Gillard, E., Boisselier, É., Bazin, R., Germain, L., Guérin, S.L., 2021. The Human Tissue-Engineered Cornea (hTEC): Recent Progress. *Int. J. Mol. Sci.* 22, 1291-. <https://doi.org/10.3390/ijms22031291>
- Guo, Y., Xue, Y., Wang, P., Cui, Z., Cao, J., Liu, S., Yu, Q., Zeng, Q., Zhu, D., Xie, M., Zhang, J., Li, Z., Liu, H., Zhong, J., Chen, J., 2020. Muse cell spheroids have therapeutic effect on corneal scarring wound in mice and tree shrews. *Sci. Transl. Med.* 12. <https://doi.org/10.1126/scitranslmed.aaw1120>
- Hayashi, R., Ishikawa, Y., Sasamoto, Y., Katori, R., Nomura, N., Ichikawa, T., Araki, S., Soma, T., Kawasaki, S., Sekiguchi, K., Quantock, A.J., Tsujikawa, M., Nishida, K., 2016. Coordinated ocular development from human iPS cells and recovery of corneal function. *Nat. Lond.* 531, 376–380. <https://doi.org/10.1038/nature17000>
- He, B., Wang, J., Xie, M., Xu, M., Zhang, Y., Hao, H., Xing, X., Lu, W., Han, Q., Liu, W., 2022. 3D printed biomimetic epithelium/stroma bilayer hydrogel implant for corneal regeneration. *Bioact. Mater.* 17, 234–247. <https://doi.org/10.1016/j.bioactmat.2022.01.034>
- He, J., Ou, S., Ren, J., Sun, H., He, X., Zhao, Z., Wu, H., Qu, Y., Liu, T., Jeyalatha, V., Zhang, L., Li, Q., Reinach, P.S., Quantock, A., Hao, J., Liu, Z., Li, W., 2020. Tissue engineered corneal epithelium derived from clinical-grade human embryonic stem cells. *Ocul. Surf.* 18, 672–680. <https://doi.org/10.1016/j.jtos.2020.07.009>
- Hemaya, Maria, Hemaya, Monica, Habeeb, A., 2023. Evaluating Keratoplasty for Fuchs' Endothelial Corneal Dystrophy: A Literature Review. *Curēus Palo Alto CA* 15, e33639–e33639. <https://doi.org/10.7759/cureus.33639>
- Hinton, T.J., Jallerat, Q., Palchesko, R.N., Park, J.H., Grodzicki, M.S., Shue, H.-J., Ramadan, M.H., Hudson, A.R., Feinberg, A.W., 2015. Three-dimensional printing of complex biological structures by freeform reversible embedding of suspended hydrogels. *Sci. Adv.* 1, e1500758. <https://doi.org/10.1126/sciadv.1500758>
- Hongisto, H., Ilmarinen, T., Vattulainen, M., Mikhailova, A., Skottman, H., 2017. Xeno- and feeder-free differentiation of human pluripotent stem cells to two distinct ocular epithelial cell types using simple modifications of one method. *Stem Cell Res. Ther.* 8, 291–291. <https://doi.org/10.1186/s13287-017-0738-4>
- Hu, C., Lu, W., Mata, A., Nishinari, K., Fang, Y., 2021. Ions-induced gelation of alginate: Mechanisms and applications. *Int. J. Biol. Macromol.* 177, 578–588. <https://doi.org/10.1016/j.ijbiomac.2021.02.086>
- Hussain, Z., Pei, R., 2021. Scaffold-free and scaffold-based cellular strategies and opportunities for cornea tissue engineering. *Prog. Biomed. Eng. Bristol* 3, 32003-. <https://doi.org/10.1088/2516-1091/ac12d7>
- Isaacson, A., Swioklo, S., Connon, C.J., 2018. 3D bioprinting of a corneal stroma equivalent. *Exp. Eye Res.* 173, 188–193. <https://doi.org/10.1016/j.exer.2018.05.010>
- Iyer, G., Srinivasan, B., Agarwal, S., Talele, D., Rishi, E., Rishi, P., Krishnamurthy, S., Vijaya, L., Subramanian, N., Somasundaram, S., 2018. Keratoprosthesis: Current global scenario and a broad Indian perspective. *Indian J. Ophthalmol.* 66, 620–629. https://doi.org/10.4103/ijo.IJO_22_18
- Jester, J.V., 2008. Corneal crystallins and the development of cellular transparency. *Semin. Cell Dev. Biol.* 19, 82–93. <https://doi.org/10.1016/j.semcdb.2007.09.015>
- Jia, S., Bu, Y., Lau, D.-S.A., Lin, Z., Sun, T., Lu, W.W., Lu, S., Ruan, C., Chan, C.-H.J., 2023. Advances in 3D bioprinting technology for functional corneal reconstruction and regeneration. *Front. Bioeng. Biotechnol.* 10, 1065460–1065460. <https://doi.org/10.3389/fbioe.2022.1065460>
- Jiang, Y., Chen, J., Deng, C., Suuronen, E.J., Zhong, Z., 2014. Click hydrogels, microgels and nanogels: Emerging platforms for drug delivery and tissue engineering. *Biomaterials* 35, 4969–4985. <https://doi.org/10.1016/j.biomaterials.2014.03.001>
- Jirsova, K., Jones, G.L.A., 2017. Amniotic membrane in ophthalmology: properties, preparation, storage and indications for grafting—a review. *Cell Tissue Bank.* 18, 193–204. <https://doi.org/10.1007/s10561-017-9618-5>

- Jongprasitkul, H., Turunen, S., Parihar, V.S., Kellomäki, M., 2022. Two-step crosslinking to enhance the printability of methacrylated gellan gum biomaterial ink for extrusion-based 3D bioprinting. *Bioprinting* 25, e00185-. <https://doi.org/10.1016/j.bprint.2021.e00185>
- Karvinen, J., Kellomäki, M., 2023. Design aspects and characterization of hydrogel-based bioinks for extrusion-based bioprinting. *Bioprinting* 32, e00274-. <https://doi.org/10.1016/j.bprint.2023.e00274>
- Karvinen, J., Koivisto, J.T., Jönkkäri, I., Kellomäki, M., 2017. The production of injectable hydrazone crosslinked gellan gum-hyaluronan-hydrogels with tunable mechanical and physical properties. *J. Mech. Behav. Biomed. Mater.* 71, 383–391. <https://doi.org/10.1016/j.jmbbm.2017.04.006>
- Kauppila, M., Möro, A., Valle-Delgado, J.J., Ihalainen, T., Sukki, L., Puistola, P., Kallio, P., Ilmarinen, T., Österberg, M., Skottman, H., 2023. Toward Corneal Limbus In Vitro Model: Regulation of hPSC-LSC Phenotype by Matrix Stiffness and Topography During Cell Differentiation Process. *Adv. Healthc. Mater.* e2301396–e2301396. <https://doi.org/10.1002/adhm.202301396>
- Kesti, M., Müller, M., Becher, J., Schnabelrauch, M., D'Este, M., Eglin, D., Zenobi-Wong, M., 2015. A versatile bioink for three-dimensional printing of cellular scaffolds based on thermally and photo-triggered tandem gelation. *Acta Biomater.* 11, 162–172. <https://doi.org/10.1016/j.actbio.2014.09.033>
- Khoshnood, N., Zamanian, A., 2020. Decellularized extracellular matrix bioinks and their application in skin tissue engineering. *Bioprinting* 20, e00095-. <https://doi.org/10.1016/j.bprint.2020.e00095>
- Kilic Bektas, C., Hasirci, V., 2020. Cell loaded 3D bioprinted GelMA hydrogels for corneal stroma engineering. *Biomater. Sci.* 8, 438–449. <https://doi.org/10.1039/c9bm01236b>
- Kim, H., Jang, J., Park, J., Lee, K.-P., Lee, S., Lee, D.-M., Kim, K.H., Kim, H.K., Cho, D.-W., 2019a. Shear-induced alignment of collagen fibrils using 3D cell printing for corneal stroma tissue engineering. *Biofabrication* 11, 035017–035017. <https://doi.org/10.1088/1758-5090/ab1a8b>
- Kim, H., Park, M.-N., Kim, J., Jang, J., Kim, H.-K., Cho, D.-W., 2019b. Characterization of cornea-specific bioink: high transparency, improved in vivo safety. *J. Tissue Eng.* 10, 2041731418823382–2041731418823382. <https://doi.org/10.1177/2041731418823382>
- Kim, K.W., Lee, S.J., Park, S.H., Kim, J.C., 2018. Ex Vivo Functionality of 3D Bioprinted Corneal Endothelium Engineered with Ribonuclease 5-Overexpressing Human Corneal Endothelial Cells. *Adv. Healthc. Mater.* 7, e1800398-n/a. <https://doi.org/10.1002/adhm.201800398>
- Knowlton, S., Yenilmez, B., Anand, S., Tasoglu, S., 2017. Photocrosslinking-based bioprinting: Examining crosslinking schemes. *Bioprinting* 5, 10–18. <https://doi.org/10.1016/j.bprint.2017.03.001>
- Koivusalo, L., Karvinen, J., Sorsa, E., Jönkkäri, I., Väliäho, J., Kallio, P., Ilmarinen, T., Miettinen, S., Skottman, H., Kellomäki, M., 2018. Hydrazone crosslinked hyaluronan-based hydrogels for therapeutic delivery of adipose stem cells to treat corneal defects. *Mater. Sci. Eng. C* 85, 68–78. <https://doi.org/10.1016/j.msec.2017.12.013>
- Koivusalo, L., Kauppila, M., Samanta, S., Parihar, V.S., Ilmarinen, T., Miettinen, S., Oommen, O.P., Skottman, H., 2019. Tissue adhesive hyaluronic acid hydrogels for sutureless stem cell delivery and regeneration of corneal epithelium and stroma. *Biomaterials* 225, 119516–119516. <https://doi.org/10.1016/j.biomaterials.2019.119516>
- Kong, Z., Wang, X., 2023. Bioprinting Technologies and Bioinks for Vascular Model Establishment. *Int. J. Mol. Sci.* 24, 891-. <https://doi.org/10.3390/ijms24010891>
- Kutlehria, S., Dinh, T.C., Bagde, A., Patel, N., Gebeyehu, A., Singh, M., 2020. High-throughput 3D bioprinting of corneal stromal equivalents. *J. Biomed. Mater. Res. B Appl. Biomater.* 108, 2981–2994. <https://doi.org/10.1002/jbm.b.34628>
- Langer, R., Vacanti, J.P., 1993. Tissue Engineering. *Sci. Am. Assoc. Adv. Sci.* 260, 920–926. <https://doi.org/10.1126/science.8493529>
- Le, Q., Deng, S.X., 2019. The application of human amniotic membrane in the surgical management of limbal stem cell deficiency. *Ocul. Surf.* 17, 221–229. <https://doi.org/10.1016/j.jtos.2019.01.003>
- Li, G., Xu, F., Zhu, J., Krawczyk, M., Zhang, Y., Yuan, J., Patel, S., Wang, Y., Lin, Y., Zhang, Ming, Cai, H., Chen, D., Zhang, Meixia, Cao, G., Yeh, E., Lin, D., Su, Q., Li, W., Sen, G.L., Afshari, N., Chen, S., Maas, R.L., Fu, X.-D., Zhang, K., Liu, Y., Ouyang, H., 2015.

- Transcription Factor PAX6 (Paired Box 6) Controls Limbal Stem Cell Lineage in Development and Disease. *J. Biol. Chem.* 290, 20448–20454. <https://doi.org/10.1074/jbc.M115.662940>
- Li, W., Wang, M., Ma, H., Chapa-Villarreal, F.A., Lobo, A.O., Zhang, Y.S., 2023. Stereolithography apparatus and digital light processing-based 3D bioprinting for tissue fabrication. *iScience* 26, 106039–106039. <https://doi.org/10.1016/j.isci.2023.106039>
- Lim, K.S., Galarraga, J.H., Cui, X., Lindberg, G.C.J., Burdick, J.A., Woodfield, T.B.F., 2020. Fundamentals and Applications of Photo-Cross-Linking in Bioprinting. *Chem. Rev.* 120, 10637–10669. <https://doi.org/10.1021/acs.chemrev.9b00812>
- Mahdavi, S.S., Abdekhodaie, M.J., Kumar, H., Mashayekhan, S., Baradaran-Rafii, A., Kim, K., 2020a. Stereolithography 3D Bioprinting Method for Fabrication of Human Corneal Stroma Equivalent. *Ann. Biomed. Eng.* 48, 1955–1970. <https://doi.org/10.1007/s10439-020-02537-6>
- Mahdavi, S.S., Abdekhodaie, M.J., Mashayekhan, S., Baradaran-Rafii, A., Djalilian, A.R., 2020b. Bioengineering Approaches for Corneal Regenerative Medicine. *Tissue Eng. Regen. Med.* 17, 567–593. <https://doi.org/10.1007/s13770-020-00262-8>
- Mancha Sánchez, E., Gómez-Blanco, J.C., López Nieto, E., Casado, J.G., Macías-García, A., Díaz Díez, M.A., Carrasco-Amador, J.P., Torrejón Martín, D., Sánchez-Margallo, F.M., Pagador, J.B., 2020. Hydrogels for Bioprinting: A Systematic Review of Hydrogels Synthesis, Bioprinting Parameters, and Bioprinted Structures Behavior. *Front. Bioeng. Biotechnol.* 8, 776–776. <https://doi.org/10.3389/fbioe.2020.00776>
- Mandrycky, C., Wang, Z., Kim, K., Kim, D.-H., 2016. 3D bioprinting for engineering complex tissues. *Biotechnol. Adv.* 34, 422–434. <https://doi.org/10.1016/j.biotechadv.2015.12.011>
- Mantha, S., Pillai, S., Khayambashi, P., Upadhyay, A., Zhang, Y., Tao, O., Pham, H.M., Tran, S.D., 2019. Smart Hydrogels in Tissue Engineering and Regenerative Medicine. *Materials* 12, 3323-. <https://doi.org/10.3390/ma12203323>
- Matthysen, S., Van den Bogerd, B., Dhubbhghail, S.N., Koppen, C., Zakaria, N., 2018. Corneal regeneration: A review of stromal replacements. *Acta Biomater.* 69, 31–41. <https://doi.org/10.1016/j.actbio.2018.01.023>
- Meek, K.M., Knupp, C., 2015. Corneal structure and transparency. *Prog. Retin. Eye Res.* 49, 1–16. <https://doi.org/10.1016/j.preteyeres.2015.07.001>
- Mikhailova, A., Ilmarinen, T., Uusitalo, H., Skottman, H., 2014. Small-Molecule Induction Promotes Corneal Epithelial Cell Differentiation from Human Induced Pluripotent Stem Cells. *Stem Cell Rep.* 2, 219–231. <https://doi.org/10.1016/j.stemcr.2013.12.014>
- Møller-Pedersen, T., Ledet, T., Ehlers, N., 1994. The keratocyte density of human donor corneas. *Curr. Eye Res.* 13, 163–169. <https://doi.org/10.3109/02713689409042412>
- Mörö, A., Samanta, S., Honkamäki, L., Rangasami, V.K., Puistola, P., Kauppila, M., Narkilahti, S., Miettinen, S., Oommen, O., Skottman, H., 2022. Hyaluronic acid based next generation bioink for 3D bioprinting of human stem cell derived corneal stromal model with innervation. *Biofabrication* 15, 15020-. <https://doi.org/10.1088/1758-5090/acab34>
- Mueller, E., Poulin, I., Bodnaryk, W.J., Hoare, T., 2022. Click Chemistry Hydrogels for Extrusion Bioprinting: Progress, Challenges, and Opportunities. *Biomacromolecules* 23, 619–640. <https://doi.org/10.1021/acs.biomac.1c01105>
- Muir, V.G., Burdick, J.A., 2021. Chemically Modified Biopolymers for the Formation of Biomedical Hydrogels. *Chem. Rev.* 121, 10908–10949. <https://doi.org/10.1021/acs.chemrev.0c00923>
- Müller, M., Becher, J., Schnabelrauch, M., Zenobi-Wong, M., 2015. Nanostructured Pluronic hydrogels as bioinks for 3D bioprinting. *Biofabrication* 7, 035006–035006. <https://doi.org/10.1088/1758-5090/7/3/035006>
- Naylor, R.W., McGhee, C.N.J., Cowan, C.A., Davidson, A.J., Holm, T.M., Sherwin, T., 2016. Derivation of Corneal Keratocyte-Like Cells from Human Induced Pluripotent Stem Cells. *PLoS One* 11, e0165464–e0165464. <https://doi.org/10.1371/journal.pone.0165464>
- Nejad, A.R., Hamidieh, A.A., Amirkhani, M.A., Sisakht, M.M., 2021. Update review on five top clinical applications of human amniotic membrane in regenerative medicine. *Placenta Eastbourne* 103, 104–119. <https://doi.org/10.1016/j.placenta.2020.10.026>
- Nejati, S., Mongeau, L., 2023. Injectable, pore-forming, self-healing, and adhesive hyaluronan hydrogels for soft tissue engineering applications. *Sci. Rep.* 13, 14303–14303. <https://doi.org/10.1038/s41598-023-41468-9>
- Nie, L., Sun, Y., Okoro, O.V., Deng, Y., Jiang, G., Shavandi, A., 2023. Click chemistry for 3D bioprinting. *Mater. Horiz.* 1, 2727–2763. <https://doi.org/10.1039/d3mh00516j>

- Nikolova, M.P., Chavali, M.S., 2019. Recent advances in biomaterials for 3D scaffolds: A review. *Bioact. Mater.* 4, 271–292. <https://doi.org/10.1016/j.bioactmat.2019.10.005>
- OptiCol™, 2023. OptiCol™ Human Collagen Type I (3 mg/ml), 60 mg [WWW Document]. URL <https://www.cellgs.com/products/opticoland8482-human-collagen-type-i-3-mgml-60-mg.html#Documents> (accessed 11.15.23).
- Orwin, E.J., Borene, M.L., Hubel, A., 2003. Biomechanical and optical characteristics of a corneal stromal equivalent. *J. Biomech. Eng.* 125, 439–444. <https://doi.org/10.1115/1.1589773>
- Osaka University, 2019. World's first transplant of cornea made from iPS cells | Graduate School of Medicine / Faculty of Medicine, Osaka University. URL <https://www.med.osaka-u.ac.jp/eng/archives/5349> (accessed 11.9.23).
- Osei-Bempong, C., Figueiredo, F.C., Lako, M., 2013. The limbal epithelium of the eye - A review of limbal stem cell biology, disease and treatment. *BioEssays* 35, 211–219. <https://doi.org/10.1002/bies.201200086>
- Ouyang, L., Yao, R., Zhao, Y., Sun, W., 2016. Effect of bioink properties on printability and cell viability for 3D bioplotting of embryonic stem cells. *Biofabrication* 8, 035020–035020. <https://doi.org/10.1088/1758-5090/8/3/035020>
- Ovsianikov, A., Khademhosseini, A., Mironov, V., 2018. The Synergy of Scaffold-Based and Scaffold-Free Tissue Engineering Strategies. *Trends Biotechnol. Regul. Ed* 36, 348–357. <https://doi.org/10.1016/j.tibtech.2018.01.005>
- Pellegrini, G., Rama, P., Matuska, S., Lambiase, A., Bonini, S., Pcobelli, A., Colabelli, R.G., Spadea, L., Fasciani, R., Balestrazzi, E., Vinciguerra, P., Rosetta, P., Tortori, A., Nardi, M., Gabbriellini, G., Traverso, C.E., Macaluso, C., Losi, L., Percesepe, A., Venturi, B., Corradini, F., Panaras, A., Di Rocco, A., Guatelli, P., De Luca, M., 2013. Biological parameters determining the clinical outcome of autologous cultures of limbal stem cells. *Regen. Med.* 8, 553–567. <https://doi.org/10.2217/rme.13.43>
- Pellegrini, G., Traverso, C.E., Franzi, A.T., Zingirian, M., Cancedda, R., De Luca, M., 1997. Long-term restoration of damaged corneal surfaces with autologous cultivated corneal epithelium. *Lancet Br. Ed.* 349, 990–993. [https://doi.org/10.1016/S0140-6736\(96\)11188-0](https://doi.org/10.1016/S0140-6736(96)11188-0)
- Peng, B.-Y., Ou, K.-L., Liu, C.-M., Chu, S.-F., Huang, B.-H., Cho, Y.-C., Saito, T., Tsai, C.-H., Hung, K.-S., Lan, W.-C., 2022. A Three-Dimensional Bioprinted Copolymer Scaffold with Biocompatibility and Structural Integrity for Potential Tissue Regeneration Applications. *Polymers* 14, 3415-. <https://doi.org/10.3390/polym14163415>
- Pinnamaneni, N., Funderburgh, J.L., 2012. Concise Review: Stem Cells in the Corneal Stroma. *Stem Cells Dayt. Ohio* 30, 1059–1063. <https://doi.org/10.1002/stem.1100>
- Poldervaart, M.T., Goversen, B., de Ruijter, M., Abbadessa, A., Melchels, F.P.W., Öner, F.C., Dhert, W.J.A., Vermonden, T., Alblas, J., 2017. 3D bioprinting of methacrylated hyaluronic acid (MeHA) hydrogel with intrinsic osteogenicity. *PloS One* 12, e0177628–e0177628. <https://doi.org/10.1371/journal.pone.0177628>
- PrestoBlue™, 2023. PrestoBlue™ Cell Viability Reagent [WWW Document]. URL <https://www.thermofisher.com/order/catalog/product/A13261> (accessed 11.7.23).
- Rajabi, N., Rezaei, A., Kharaziha, M., Bakhsheshi-Rad, H.R., Luo, H., RamaKrishna, S., Berto, F., 2021. Recent Advances on Bioprinted Gelatin Methacrylate-Based Hydrogels for Tissue Repair. *Tissue Eng. Part A* 27, 679–702. <https://doi.org/10.1089/ten.tea.2020.0350>
- Rajabzadeh, N., Fathi, E., Farahzadi, R., 2019. Stem cell-based regenerative medicine. *Stem Cell Investig.* 6, 19–19. <https://doi.org/10.21037/sci.2019.06.04>
- Rüfer, F., Schröder, A., Erb, C., 2005. White-to-White Corneal Diameter: Normal Values in Healthy Humans Obtained With the Orbscan II Topography System. *Cornea* 24, 259–261. <https://doi.org/10.1097/01.ico.0000148312.01805.53>
- Saghizadeh, M., Kramerov, A.A., Svendsen, C.N., Ljubimov, A.V., 2017. Concise Review: Stem Cells for Corneal Wound Healing. *Stem Cells Dayt. Ohio* 35, 2105–2114. <https://doi.org/10.1002/stem.2667>
- Saini, G., Segaran, N., Mayer, J., Saini, A., Albadawi, H., Oklu, R., 2021. Applications of 3D Bioprinting in Tissue Engineering and Regenerative Medicine. *J. Clin. Med.* 10, 4966-. <https://doi.org/10.3390/jcm10214966>
- Salvador-Culla, B., Kolovou, P.E., 2016. Keratoprosthesis: A Review of Recent Advances in the Field. *J. Funct. Biomater.* 7, 13-. <https://doi.org/10.3390/jfb7020013>
- Schlötzer-Schrehardt, U., Kruse, F.E., 2005. Identification and characterization of limbal stem cells. *Exp. Eye Res.* 81, 247–264. <https://doi.org/10.1016/j.exer.2005.02.016>

- Schwab, A., Levato, R., D'Este, M., Piluso, S., Eglin, D., Malda, J., 2020. Printability and Shape Fidelity of Bioinks in 3D Bioprinting. *Chem. Rev.* 120, 10850–10877. <https://doi.org/10.1021/acs.chemrev.0c00084>
- Sekar, M.P., Suresh, S., Zennifer, A., Sethuraman, S., Sundaramurthi, D., 2023. Hyaluronic Acid as Bioink and Hydrogel Scaffolds for Tissue Engineering Applications. *ACS Biomater. Sci. Eng.* 9, 3134–3159. <https://doi.org/10.1021/acsbiomaterials.3c00299>
- Shirzaei Sani, E., Kheirkhah, A., Rana, D., Sun, Z., Foulsham, W., Sheikhi, A., Khademhosseini, A., Dana, R., Annabi, N., 2019. Sutureless repair of corneal injuries using naturally derived bioadhesive hydrogels. *Sci. Adv.* 5, eaav1281–eaav1281. <https://doi.org/10.1126/sciadv.aav1281>
- Shopperly, L.K., Spinnen, J., Krüger, J.-P., Endres, M., Sittinger, M., Lam, T., Kloke, L., Dehne, T., 2022. Blends of gelatin and hyaluronic acid stratified by stereolithographic bioprinting approximate cartilaginous matrix gradients. *J. Biomed. Mater. Res. B Appl. Biomater.* 110, 2310–2322. <https://doi.org/10.1002/jbm.b.35079>
- Shyam Mohan, T., Datta, P., Nesaei, S., Ozbolat, V., Ozbolat, I.T., 2022. 3D coaxial bioprinting: process mechanisms, bioinks and applications. *Prog. Biomed. Eng. Bristol* 4, 22003-. <https://doi.org/10.1088/2516-1091/ac631c>
- Si, Z., Wang, Xue, Sun, C., Kang, Y., Xu, J., Wang, Xidi, Hui, Y., 2019. Adipose-derived stem cells: Sources, potency, and implications for regenerative therapies. *Biomed. Pharmacother.* 114, 108765–108765. <https://doi.org/10.1016/j.biopha.2019.108765>
- Singh, N., Said, D., Dua, H., 2018. Lamellar keratoplasty techniques. *Indian J. Ophthalmol.* 66, 1239–1250. https://doi.org/10.4103/ijo.IJO_95_18
- Singh, R., Gupta, N., Vanathi, M., Tandon, R., 2019. Corneal transplantation in the modern era. *Indian J. Med. Res. New Delhi India* 1994 150, 7–22. https://doi.org/10.4103/ijmr.IJMR_141_19
- Soltan, N., Ning, L., Mohabatpour, F., Papagerakis, P., Chen, X., 2019. Printability and Cell Viability in Bioprinting Alginate Dialdehyde-Gelatin Scaffolds. *ACS Biomater. Sci. Eng.* 5, 2976–2987. <https://doi.org/10.1021/acsbiomaterials.9b00167>
- Song, Y., Hua, S., Sayyar, S., Chen, Z., Chung, J., Liu, X., Yue, Z., Angus, C., Filippi, B., Beirne, S., Wallace, G., Sutton, G., You, J., 2022. Corneal bioprinting using a high concentration pure collagen I transparent bioink. *Bioprinting* 28, e00235-. <https://doi.org/10.1016/j.bprint.2022.e00235>
- Sorkio, A., Koch, L., Koivusalo, L., Deiwick, A., Miettinen, S., Chichkov, B., Skottman, H., 2018. Human stem cell based corneal tissue mimicking structures using laser-assisted 3D bioprinting and functional bioinks. *Biomaterials* 171, 57–71. <https://doi.org/10.1016/j.biomaterials.2018.04.034>
- Sridhar, M., 2018. Anatomy of cornea and ocular surface. *Indian J. Ophthalmol.* 66, 190–194. https://doi.org/10.4103/ijo.IJO_646_17
- Stepanovska, J., Supova, M., Hanzalek, K., Broz, A., Matejka, R., 2021. Collagen Bioinks for Bioprinting: A Systematic Review of Hydrogel Properties, Bioprinting Parameters, Protocols, and Bioprinted Structure Characteristics. *Biomedicines* 9, 1137-. <https://doi.org/10.3390/biomedicines9091137>
- Syed-Picard, F.N., Du, Y., Hertszenberg, A.J., Palchesko, R., Funderburgh, M.L., Feinberg, A.W., Funderburgh, J.L., 2018. Scaffold-free tissue engineering of functional corneal stromal tissue. *J. Tissue Eng. Regen. Med.* 12, 59–69. <https://doi.org/10.1002/term.2363>
- Tafti, M.F., Aghamollaei, H., Moghaddam, M.M., Jadidi, K., Alio, J.L., Faghihi, S., 2022. Emerging tissue engineering strategies for the corneal regeneration. *J. Tissue Eng. Regen. Med.* 16, 683–706. <https://doi.org/10.1002/term.3309>
- Takahashi, K., Tanabe, K., Ohnuki, M., Narita, M., Ichisaka, T., Tomoda, K., Yamanaka, S., 2007. Induction of Pluripotent Stem Cells from Adult Human Fibroblasts by Defined Factors. *Cell* 131, 861–872. <https://doi.org/10.1016/j.cell.2007.11.019>
- Tan, D.T., Dart, J.K., Holland, E.J., Kinoshita, S., 2012. Corneal transplantation. *Lancet Br. Ed.* 379, 1749–1761. [https://doi.org/10.1016/S0140-6736\(12\)60437-1](https://doi.org/10.1016/S0140-6736(12)60437-1)
- Taylor, A.W., 2009. Ocular immune privilege. *Eye Lond.* 23, 1885–1889. <https://doi.org/10.1038/eye.2008.382>
- Thoft, R.A., Friend, J., 1983. The X, Y, Z hypothesis of corneal epithelial maintenance. *Invest. Ophthalmol. Vis. Sci.* 24, 1442–1443.
- Thomson, J.A., Itskovitz-Eldor, J., Shapiro, S.S., Waknitz, M.A., Swiergiel, J.J., Marshall, V.S., Jones, J.M., 1998. Embryonic Stem Cell Lines Derived from Human Blastocysts. *Sci. Am. Assoc. Adv. Sci.* 282, 1145–1147. <https://doi.org/10.1126/science.282.5391.1145>

- Ullah, I., Subbarao, R.B., Rho, G.J., 2015. Human mesenchymal stem cells - current trends and future prospective. *Biosci. Rep.* 35, e00191-. <https://doi.org/10.1042/BSR20150025>
- van der Sanden, B., Dhobb, M., Berger, F., Wion, D., 2010. Optimizing stem cell culture. *J. Cell. Biochem.* 111, 801–807. <https://doi.org/10.1002/jcb.22847>
- Vattulainen, M., Ilmarinen, T., Koivusalo, L., Viiri, K., Hongisto, H., Skottman, H., 2019. Modulation of Wnt/BMP pathways during corneal differentiation of hPSC maintains ABCG2-positive LSC population that demonstrates increased regenerative potential. *Stem Cell Res. Ther.* 10, 236–236. <https://doi.org/10.1186/s13287-019-1354-2>
- Vattulainen, M., Ilmarinen, T., Viheriälä, T., Jokinen, V., Skottman, H., 2021. Corneal epithelial differentiation of human pluripotent stem cells generates ABCB5 + and Δ Np63 α + cells with limbal cell characteristics and high wound healing capacity. *Stem Cell Res. Ther.* 12, 609–609. <https://doi.org/10.1186/s13287-021-02673-3>
- Ventura, L., Jesus, G.T. de, Oliveira, G.C.D. de, Sousa, S.J.F., 2005. Portable light transmission measuring system for preserved corneas. *Biomed. Eng. Online* 4, 70–70. <https://doi.org/10.1186/1475-925X-4-70>
- Vijayavenkataraman, S., Yan, W.-C., Lu, W.F., Wang, C.-H., Fuh, J.Y.H., 2018. 3D bioprinting of tissues and organs for regenerative medicine. *Adv. Drug Deliv. Rev.* 132, 296–332. <https://doi.org/10.1016/j.addr.2018.07.004>
- Wan, L.Q., Jiang, J., Arnold, D.E., Guo, X.E., Lu, H.H., Mow, V.C., 2008. Calcium Concentration Effects on the Mechanical and Biochemical Properties of Chondrocyte-Alginate Constructs. *Cell. Mol. Bioeng.* 1, 93–102. <https://doi.org/10.1007/s12195-008-0014-x>
- Wang, L.L., Highley, C.B., Yeh, Y.-C., Galarraga, J.H., Uman, S., Burdick, J.A., 2018. 3D extrusion bioprinting of single- and double-network hydrogels containing dynamic covalent crosslinks. *J. Biomed. Mater. Res. A* 106, 865–875. <https://doi.org/10.1002/jbm.a.36323>
- Wang, M., Li, Y., Wang, H., Li, M., Wang, X., Liu, R., Zhang, D., Xu, W., 2023. Corneal regeneration strategies: From stem cell therapy to tissue engineered stem cell scaffolds. *Biomed. Pharmacother.* 165, 115206–115206. <https://doi.org/10.1016/j.biopha.2023.115206>
- Wang, S., Ghezzi, C.E., Gomes, R., Pollard, R.E., Funderburgh, J.L., Kaplan, D.L., 2017. In vitro 3D corneal tissue model with epithelium, stroma, and innervation. *Biomaterials* 112, 1–9. <https://doi.org/10.1016/j.biomaterials.2016.09.030>
- Wang, S., Oommen, O.P., Yan, H., Varghese, O.P., 2013. Mild and Efficient Strategy for Site-Selective Aldehyde Modification of Glycosaminoglycans: Tailoring Hydrogels with Tunable Release of Growth Factor. *Biomacromolecules* 14, 2427–2432. <https://doi.org/10.1021/bm400612h>
- WHO, 2023. ICTRP Search Portal [WWW Document]. URL <https://trialsearch.who.int/?TrialID=JPRN-UMIN000036539> (accessed 12.6.23).
- Wilson, S.E., 2020. Corneal wound healing. *Exp. Eye Res.* 197, 108089–108089. <https://doi.org/10.1016/j.exer.2020.108089>
- Wilson, S.L., Wimpenny, I., Ahearne, M., Rauz, S., El Haj, A.J., Yang, Y., 2012. Chemical and Topographical Effects on Cell Differentiation and Matrix Elasticity in a Corneal Stromal Layer Model. *Adv. Funct. Mater.* 22, 3641–3649. <https://doi.org/10.1002/adfm.201200655>
- Wu, Y., Qin, M., Yang, X., 2023. Organ bioprinting: progress, challenges and outlook. *J. Mater. Chem. B Mater. Biol. Med.* <https://doi.org/10.1039/D3TB01630G>
- Wu, Z., Su, X., Xu, Y., Kong, B., Sun, W., Mi, S., 2016. Bioprinting three-dimensional cell-laden tissue constructs with controllable degradation. *Sci. Rep.* 6, 24474–24474. <https://doi.org/10.1038/srep24474>
- Yam, G.H.F., Riau, A.K., Funderburgh, M.L., Mehta, J.S., Jhanji, V., 2020. Keratocyte biology. *Exp. Eye Res.* 196, 108062–108062. <https://doi.org/10.1016/j.exer.2020.108062>
- Yazdanpanah, G., Haq, Z., Kang, K., Jabbehdari, S., Rosenblatt, M. I., Djallilian, A.R., 2019. Strategies for reconstructing the limbal stem cell niche. *Ocul. Surf.* 17, 230–240. <https://doi.org/10.1016/j.jtos.2019.01.002>
- Zakrzewski, W., Dobrzyński, M., Szymonowicz, M., Rybak, Z., 2019. Stem cells: past, present, and future. *Stem Cell Res. Ther.* 10, 68–68. <https://doi.org/10.1186/s13287-019-1165-5>
- Zennifer, A., Manivannan, S., Sethuraman, S., Kumbar, S.G., Sundaramurthi, D., 2022. 3D bioprinting and photocrosslinking: emerging strategies & future perspectives. *Biomater. Adv.* 134, 112576–112576. <https://doi.org/10.1016/j.msec.2021.112576>
- Zhang, B., Xue, Q., Hu, H., Yu, M., Gao, L., Luo, Y., Li, Y., Li, J., Ma, L., Yao, Y., Yang, H., 2019a. Integrated 3D bioprinting-based geometry-control strategy for fabricating corneal substitutes. *J. Zhejiang Univ. B Sci.* 20, 945–959. <https://doi.org/10.1631/jzus.B1900190>

- Zhang, B., Xue, Q., Li, J., Ma, L., Yao, Y., Ye, H., Cui, Z., Yang, H., 2019b. 3D bioprinting for artificial cornea: Challenges and perspectives. *Med. Eng. Phys.* 71, 68–78. <https://doi.org/10.1016/j.medengphy.2019.05.002>
- Zhang, M., Yang, F., Han, D., Zhang, S.-Y., Dong, Y., Li, X., Ling, L., Deng, Z., Cao, X., Tian, J., Ye, Q., Wang, Y., 2023. 3D bioprinting of corneal decellularized extracellular matrix: GelMA composite hydrogel for corneal stroma engineering. *Int. J. Bioprinting* 9, 774–774. <https://doi.org/10.18063/ijb.774>
- Zhong, Z., Balayan, A., Tian, J., Xiang, Y., Hwang, H.H., Wu, X., Deng, X., Schimelman, J., Sun, Y., Ma, C., Dos Santos, A., You, S., Tang, M., Yao, E., Shi, X., Steinmetz, N.F., Deng, S.X., Chen, S., 2021. Bioprinting of dual ECM scaffolds encapsulating limbal stem/progenitor cells in active and quiescent statuses. *Biofabrication* 13, 44101-. <https://doi.org/10.1088/1758-5090/ac1992>
- Zhou, L., Chen, E., Jin, W., Wang, Y., Zhou, J., Wei, S., 2016. Monomer zinc phthalocyanine/up-conversion nanoparticle coated with hyaluronic acid crosslinked gel as NIR light-activated drug for in vitro photodynamic therapy. *Dalton Trans. Int. J. Inorg. Chem.* 45, 15170–15179. <https://doi.org/10.1039/c6dt01929c>